Laser Heating, Refrigeration, and Thermometry of Semiconductor Nanomaterials

Anupum Pant

A dissertation
submitted in partial fulfillment of the
requirements for the degree of

Doctor of Philosophy

University of Washington

2020

Reading Committee:

Peter J. Pauzauskie, Chair

Fumio Ohuchi

Jihui Yang

Program Authorized to Offer Degree:
Materials Science and Engineering

University of Washington

Abstract

Laser Heating, Refrigeration, and Thermometry of Semiconductor Nanomaterials

Anupum Pant

Chair of the Supervisory Committee:
Dr. Peter J. Pauzauskie
Materials Science and Engineering

Photothermal heating is a major constraint that limits the performance of many nanoscale optoelectronic and optomechanical semiconductor devices including nanolasers, optomechanical resonators, and integrated photonic circuits. Laser refrigeration of semiconductor devices to counteract photothermal heating has been a long-standing challenge. This work highlights the errors in previous experimental efforts and shows that the existing semiconductor laser refrigeration claims are controversial. It also presents an alternative route to experimentally achieve the laser refrigeration of a CdS nanoribbon (CdSNR) by >20 K, using Yb^{3+} doped $LiYF_4$ microcrystal attached to it. Further, it explores the other promising avenues for achieving intrinsic laser refrigeration in wide band gap semiconductor materials, such as diamond, using color centers.

This work aims to develop a deep understanding of the physics of photothermal effect in nanostructures such as CdSNRs by considering the morphology, wavelength, refractive index and other physical parameters that affect its magnitude. A novel non-contact optomechanical thermometry method for measuring temperatures within nanostructures was developed by including the effects of laser trapping forces and temperature gradient. Thermometry experiments were conducted on CdSNRs of various geometries - cantilever, wedge and bridge using complementary techniques such as eigenfrequency and anti-Stokes Stokes Raman thermometry. The experimental techniques were also validated by developing exact

analytical heat transfer theory for each type of geometry. The time scales to reach steady state were found to be smaller than 30 ms for the CdSNRs despite including the lowest thermal conductance at the interface of the device and the substrate. These time scales were four orders of magnitude faster than the those reported by Zhang *et al.*[1] The acceptance of this result into major publications suggests that there is a gap in the deep understanding with regards to the physics of heat transfer in nanoscale materials.

Consequently, to counteract the photothermal effect that caused the heating of CdSNR cantilever sensors, the refrigeration of this sensor was accomplished by the use of anti-Stokes photoluminescence of trivalent ytterbium ions doped within a yttrium-lithium-fluoride ($LiYF_4$) host crystal. A >20 K drop in temperature was measured using optomechanical thermometry. Optically-refrigerating the lattice of a dielectric resonator has the potential to impact several fields including scanning probe microscopy, the sensing of weak forces, the measurement of atomic masses, and the development of radiation-balanced solid-state lasers. In addition, optically refrigerated resonators may be used in the future as a promising starting point to perform motional cooling for exploration of quantum effects at mesoscopic length scales, temperature control within integrated photonic devices, and solid-state laser refrigeration of quantum materials. In the following work, cooling NV^-:NDs by 27 K at $\sim 10^{-3}$ Torr was achieved by attaching them to a 10% Yb:$LiYF_4$ microcrystal. The temperature of the NV^-:NDs and the cooling crystal was measured using Debye-Waller factor (DWF) thermometry and ratiometric Yb ion thermometry, respectively. Stabilization of thermal spectral wandering of the NV^- zero-phonon-line (ZPL) was achieved by modulating the 1020 nm laser irradiance. The demonstrated cooling of NV^-:NDs using an optically cooled microcrystal opens up new possibilities for rapid feedback-controlled cooling of a wide range of nanoscale quantum materials.

Finally, to explore the intrinsic cooling of wide band gap semiconductors, the photothermal effects due to NV doping in nanodiamonds (NDs) was evaluated by attaching them to

silica microsphere resonators. Analytical heat transfer theory was developed for both spherical and cylindrical bodies with localized sources. The H3 defects are recommended for future exploration for laser refrigeration of wide band gap semiconductors using color centers. This recommendation is based on the 10-fold reduction of heating measured in a diamond sample containing predominantly H3 defects, compared to an NV doped diamond. The observation of anti Stokes emission from the H3 is also encouraging for the endeavor of achieving intrinsic semiconductor cooling.

TABLE OF CONTENTS

LIST OF FIGURES

GLOSSARY

DWFT: Debye-Waller factor thermometry

CDSNRS: cadmium sulfide nanoribbons

RE: Rare earth

TIR: Total internal reflections

EQE: External quantum efficiency

MAT: Minimum achievable temperature

DLT: Differential luminescence thermometry

TBDLT: Two-band Differential luminescence thermometry

IR: Infrared

PPLT: Pump-probe luminescence thermometry

SP / LP: Short pass / Long pass

ICF: Intensity correction factor

DWF: Debye-Waller factor

ND: Nanodiamond

ZPL: Zero phonon line

MW: Microwave

ODMR: Optically detected magnetic resonance

FTIR: Fourier-transform infrared spectroscopy

AFM: Atomic force microscopy

PL: photoluminescence

LOP: Longitudnal optical phonon

CVT: Chemical vapor transport

AUNC: Gold nanocrystals

SCCM: Standard cubic centimeters per minute

APD: Avalanche photodiode

FL: Focusing lens

HLB: Holographic beam splitter cube

NF: Notch filter

TEM: Transmission electron microscopy

SAED: Select area electron diffraction

NR: Nanoribbon

VND: Variable neutral density filter

DL: Diode laser

BS: Beam splitter

LITMOS: Laser Induced Modulation Spectroscopy

Some passages have been quoted verbatim from the following sources:

- **A. Pant**, B. E. Smith, M. J. Crane, X. Zhou, M. B. Lim, S. A. Frazier, E. J. Davis, and P. J. Pauzauskie. "Optomechanical thermometry of nanoribbon cantilevers." *The Journal of Physical Chemistry C* **122.13** (2018): 7525-7532.

- **A. Pant**[*], Y. V. Morozov[*], S. Zhang[*], Boldizsár Jankó, S. D. Melgaard, D. A. Bender, P. J. Pauzauskie, and M. Kuno. *et al.* "Can lasers really refrigerate CdS nanobelts?." *Nature* **570.7762** (2019): E60-E61.

- **A. Pant**, E. J. Davis, and P. J. Pauzauskie."Photothermal heating of semiconductor nanoribbons." *The Journal of Physical Chemistry C* **123.47** (2019): 28941-28947.

- **A. Pant**, X. Xia, E. J. Davis, and P. J. Pauzauskie. "Solid-state laser refrigeration of a composite semiconductor Yb:$YLiF_4$ optomechanical resonator." *Nature Communications* **11.1** (2020): 1-7.

- **A. Pant**, R. G. Felsted, A. B. Bard, X. Xia, S. Dadras, K. Shayan, D. R. Luntz-Martin, D. Mannikko, I. M. Pavlovetc, S. Stoll, M Kuno, A. N. Vamivakas, and P. J. Pauzauskie. "Solid-state laser refrigeration of nanodiamond quantum sensors." (*in preparation* 2020).

- X. Xia, **A. Pant**, A. S. Ganas, F. Jelezko, and P. J. Pauzauskie. "Quantum point defects for solid state laser refrigeration." *Advanced Materials* (*in press* 2020).

---

[*] *Indicates equal contribution*

ACKNOWLEDGMENTS

I would like to thank my advisor, Professor Peter J. Pauzauskie. His enthusiasm for learning and experimentation was an inspiration to me for the past 4 years and, I am certain, will continue to inspire future students for years to come. Likewise, I am appreciative to Professor Emeritus E. James Davis for all of his guidance and feedback and honored to have been able to collaborate on so many fruitful projects. I thank Prof. Fedor Jelezko for valuable conversations and the idea to attempt laser cooling of H3-doped diamond materials.

I want to thank Dr. Bennett E. Smith for the conception and initial development related to the optomechanical thermometry method which gave me a boost in my first year of PhD. I also thank him and Dr. Paden Roder for inspiring the coder in me which increased my productivity one hundred folds. Thanks to Dr. Matt Crane, Dr. Xuezhe Zhou, Stuart Frazier, Dr. Matt Lim, Xiaojing Xia, Abbie Ganas, Alex Bard, Greg Felsted, Dr. Elena Dobretsova and Rachel Gariepy for all the things they taught me and for supporting me during hard times. I want to thank Yueyang Chen for helping with the silicon nitride nanobeam optical cavity experiments.

I want to thank my parents and brother for being unconditionally supportive of my education in every way. At every point I knew they were the safety net that would catch me if I fell. It allowed me to focus on the task ahead and take risks. Finally, I cannot thank my wife enough for choosing to leave a world behind and being with me during the Covid-19 pandemic. I would have had a hard time functioning alone and finishing my PhD without all of the support she gave me as social distancing measures were put in for several months at the end of my degree.

DEDICATION

to my dear family

Chapter 1

INTRODUCTION

It is well known that a certain fraction of electromagnetic radiation (photons) incident on a material may get absorbed and generate thermal energy within the material. This is known as photothermal heating. In some ways photothermal heating helps to make our lives easier, such as when we use electromagnetic radiation in a microwave oven ($\lambda_0 \sim 5$ cm) to heat our foods. It has also been used in groundbreaking techniques such as photodynamic therapy, where cancerous and precancerous cells can be destroyed by selectively attaching photosensitizers and heating them with a specific wavelength of light.[3] Other areas where photothermal heating has led to fascinating observations includes catalysis[4], sea water desalination[5], and superheating of solvents, among many other applications. Unless certain rare conditions are met, light heats materials irrespective of whether it is desired or not. When it is undesirable, photothermal heating may cause loss of accuracy in scientific measurements using sensors or may even irreversibly damage materials by melting or burning them.

1.1 The bane of photothermal heating

The loss of accuracy in sensors due to photothermal heating has traditionally been counteracted by attaching an external heat sink to the system. The heat sink is used to actively draw heat from the sensor which can help maintain a constant temperature within the sensor, which in turn would help in reducing measurement noise due to thermal fluctuations. For example, microscopic sensors can be cooled by attaching a large cryostat. But because of the large size of such heat sinks, the control loop cannot physically be made fast enough to counteract temperature fluctuations in millisecond or microsecond timescales. In addition,

when the sensor is free of contact to any conductive or convective surface, as in the case of levitated sensors in optical trapping,[6, 7] heat management through such methods is non trivial. Thus the traditional cooling methods that cool through conduction or convection are inadequate in helping maintain desirable temperature within sensors levitated in air or vacuum. Vibrations and finite lifetimes of coolers due to the presence of various moving parts such as pumps has also been a major hindrance in conducting precision science.

Photothermal heating of solid-state gain media also impedes the development of very high powered lasers. This is because the rate of heat generation due to photothermal heating, or the temperature gradients can be so large in the solid-state gain media that they cannot be counteracted with traditional cooling techniques. This may cause damage to the gain media when attempting to generate very high laser powers. Or this may result in a poor beam quality due to the large gradient of refractive index induced by irregular heating of the gain medium. In such cases an internal cooling mechanism is desirable that can help maintain temperature gradients across the solid-state gain media for the realization of very high powered lasers without loss of beam quality. This may be achieved with the use of radiation balanced or athermal lasing scheme which will be discussed in the following sections.

Due to the tremendous progress in the area of solid-state laser refrigeration, this non traditional method of cooling has generated great interest within the scientific community for the last few decades as it has proven to be useful in the areas where traditional cooling methods have not been adequate. Under the right circumstances, this method of cooling can be used to cool the right materials simply by directing a laser beam into it. Laser refrigeration can induce intrinsic cooling in solid materials. In addition, this cooling happens radiatively, which makes it possible to cool these materials in vacuum without any attached contacts. It also may be built without any moving parts, enabling high precision science and can be used to cool using microscopic or nanoscale crystals by focusing the coherent laser radiation to a small spot.

1.2 Laser refrigeration of rare-earth (RE) doped solids

Laser cooling is a term that is widely used in the Doppler cooling community for the cooling of metal atom vapors using laser irradiation. It is physically a different process that requires high vacuum and low starting temperature conditions which prevents it from being adopted as a practical cooling scheme for solids near room temperature and atmospheric pressure. In this thesis, "laser refrigeration" is used for referring to solid-state laser refrigeration - a process that is able to cool a solid lattice using laser radiation.

Solid-state laser refrigeration is based on a counter-intuitive process where a solid material absorbs low-entropy photons from a laser, moves to an excited state, decays to the ground state spontaneously, and emits photons. Under the right conditions, the emitted photons may have both a higher average energy and net entropy[8]. This is similar to the reverse of the process on which optically-pumped laser works. In an optically pumped laser the defect adds heat to the gain medium. In the case of solid-state laser refrigeration, the heat is taken away by the defect (or dopant) in the form of up converted photons escaping the system.

1.2.1 Background

The first few reports on laser refrigeration was in 1929 when Pringsheim proposed the use of anti-Stokes fluorescence to refrigerate a vapor of sodium atoms[9]. However, it was only in 1995 that the first experimental demonstration of solid-state laser refrigeration was reported[10]. In the last two decades tremendous progress has been made in demonstrating the solid-state laser refrigeration of both amorphous[10, 11, 12] and crystalline materials[13, 14, 15, 16, 17, 18] under vacuum and atmospheric conditions. Solid-state laser refrigeration has also been demonstrated using microcrystals suspended in aqueous media[19], demonstrating the first instance of cold Brownian motion (CBM) since Einstein's seminal paper on Brownian motion in 1905[20].

In contrast with thermoelectric cooling, solid-state laser refrigeration is capable of cooling materials in the absence of electrical connections. It also does not require moving parts

or cryogenic fluids which eliminates detrimental mechanical vibrations or the risk of mechanical failure. Furthermore, laser refrigeration has been shown to cool materials much below the temperatures that thermoelectric cooling can reach.[13] These unique features have made laser refrigeration useful in a variety of practical applications. This has been adequately demonstrated by the laser refrigeration of a Fourier Transform Infrared Spectroscopy (FTIR) detector for imaging or spectroscopy.[21] Laser refrigeration has been investigated for the precise temperature control of frequency standards based on optical cavities[22], or modulating the temperature of individual molecules at physiological conditions[19, 23]. In addition, its viability was recently evaluated for space-borne laser refrigeration architecture to be used for temperature regulation of instruments in low earth orbit observation satellites.[24] Solid-state laser refrigeration is also inherently useful in the development of radiation-balanced lasers[25], which may be enable continuous wave (CW) lasers that can reach very high powers without overheating.

1.2.2 Radiation balanced lasing

Excessive heating is a limitation inherent to high powered lasers, which can lead to problems ranging from poor beam quality due to thermal lensing to cracking of the crystal. Because of these and other issues, the maximum power that can be generated by a laser is limited. To counteract this effect, traditionally coolers are attached on the outer surface. However, such coolers are unable to reduce the large internal thermal gradient efficiently. In addition, they add vibrations and fragility to the system due to many moving parts. In the concept of radiation balanced lasers first developed by Steven R. Bowman[25], internal cooling of laser refrigeration materials such as Yb doped $LiYF_4$ may be used where the fluorescence cooling will fully compensate the heating associated with laser emission.

1.2.3 The fundamentals of laser refrigeration

Under normal conditions a luminescent material emits photons of energy lower than the energy of photons that used to optically excite it. In other terms, the emission wavelength

is typically longer (red-shifted) compared to the absorbed photon wavelength. This red-shifting of the emitted photon's energy is known as the Stokes shift and the conservation of energy requires that the material gets heated in this process. It therefore follows that, if the emitted photons have a higher average energy relative to what was absorbed (anti-Stokes luminescence) phonon energy must be removed from the crystal lattice. If this process has a near-unit quantum efficiency, i.e. the number of photons being emitted through anti-Stokes luminescence are nearly equal to the number of photons being used to excite the material, the rate of radiative cooling via this process will exceed the rate of nonradiative heating, resulting in laser refrigeration.[26].

Initially there were concerns about the violation of the second law of the thermodynamics. These were resolved by Landau by quantifying the optical entropy of the system[27]. Landau reasoned that lasers have a low entropy due to their small divergence, narrow photon energy range, phase coherence, and well-defined polarization. Following optical excitation of the solid, the emission of spontaneous (anti-Stokes) luminescence has a higher net entropy when considering the wide divergence, broad photon energies, low phase coherence, and multiple polarization states of the emitted light. The need for optical radiation with low entropy is therefore crucial for achieving solid-state laser refrigeration. The increased optical entropy of the blue-shifted photons makes this cooling cycle consistent with the second law of thermodynamics[27].

The progress in the field of solid-state laser refrigeration has since taken off, and tremendous progress has been made in cooling heavy metal glasses using Yb^{3+} ions, since the first experimental demonstration[11, 12]. Research in the area of solid-state laser refrigeration using Yb in crystalline materials has culminated in the development of a solid-state optical cryo-cooler with bulk Yb:$LiYF_4$ single crystals grown using the Czochralski method[13], which has cooled crystals to 91 K from room temperature. The primary advantage of using crystalline materials for solid-state laser refrigeration is the existence of well-defined crystal field levels in them. These minimizes inhomogenous broadening of the rare-earth absorption spectra.

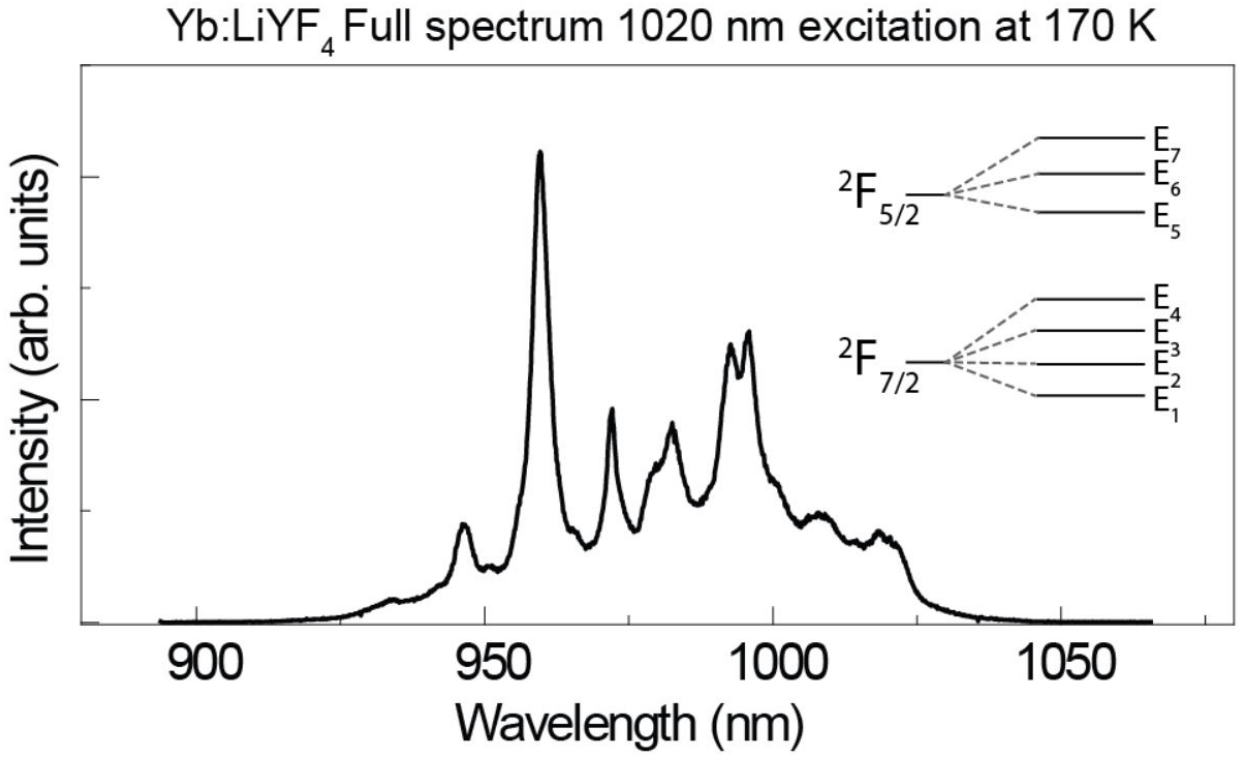

Figure 1.1: The full emission spectrum of Yb:$LiYF_4$ collected at 170 K during the decay period of a pulsed 1020 nm excitation. The inset shows a schematic of the Yb^{3+} energy level splitting in $LiYF_4$ host.

1.2.4 Yb^{3+} energy levels and the cooling process

The Yb^{3+} ions doped in an $LiYF_4$ crystal exist in a point group symmetry of S_4. Due to the low site symmetry of the crystal field, the (2J+1)-fold degeneracy of the Yb^{3+} multiplets ($^2F_{7/2}$ and $^2F_{5/2}$) is lifted. Therefore the $^2F_{7/2}$ and $^2F_{5/2}$ multiplets split into four and three Stark levels ($E_1, E_2, E_3, ...$) respectively, as illustrated in Figure 1.1. The amount of splitting in the ground-state multiplet ($^2F_{7/2}$) depends on the specific host crystal into which the Yb ion is doped. The ground-state splitting in $LiYF_4$ is 477± 10 cm^{-1}[28].

The excitation photon energy used for laser refrigeration ($h\nu$) is resonant with a differ-

ence in energy from the bottom of the excited-state manifold to the top of the ground-state manifold ($E_4 \rightarrow E_5$). The resonant excitation breaks the thermal equilibrium of the relative populations between the two manifolds. The ground and excited atoms must reach quasi-equilibrium by absorbing phonons from the lattice with the rates much faster than the spontaneous emission rate. It is known that the interactions between electrons and phonons within each manifold is known as "thermalization." This process is far faster ($\sim$ps) than the spontaneous emission rate ($\sim$ms) for a broad range of materials and temperatures. The electron-phonon interaction helps maintain the quasi-equilibrium of the Boltzmann distribution between each manifold. Consequently, the spontaneous emission of a mean photon energy ($h\nu_f$) which is greater than that of the absorbed photon exits the material and releases the energy into free space. Hence, the anti Stokes fluorescence process removes thermal energy from the material due to annihilation of phonons during each cycle as long as the quantum efficiency of the process is high.

The thermodynamic cooling efficiency η_c of the cooling cycle is expressed as

$$\eta_c = \frac{h\nu_f - h\nu}{h\nu} = \frac{\lambda}{\lambda_f} - 1, \tag{1.1}$$

where $h\nu$ is the pump photon energy, $h\nu_f$ is the mean fluorescence energy, $\lambda = c/\nu$ is the pump wavelength, and $\lambda_f = c/\nu_f$ is the mean fluorescence wavelength.

Additional considerations must be made to calculate the thermodynamic efficiency for non-ideal systems, such as the probability that a pump photon can be absorbed, the probability that an absorbed photon is converted to a fluorescence photon, and the probability a spontaneously emitted photon escapes the system. Non-ideal systems require the introduction of the other two parameters, absorption efficiency and external quantum efficiency.[29, 30] Following these considerations, the overall cooling efficiency can be rewritten as

$$\eta_c(\nu, T) = \eta_{ext}\eta_{abs}\frac{\lambda}{\lambda_f} - 1. \tag{1.2}$$

This describes the cooling efficiency by which an excited ion decays to its ground state with the fluorescence photon escaping to free space. The cooling efficiency must be positive

to realize net cooling, which means high external quantum efficiency (η_{ext}), high absorption efficiency (η_{abs}), and a large anti-Stokes shift ($h\nu_f - h\nu$) are required.

The absorption efficiency η_{abs} describes the probability of a pump photon being absorbed by the cooling ions rather than an impurity, which is a function of temperature and wavelength defined by

$$\eta_{abs} = \frac{\alpha_r(\lambda, T)}{\alpha_r(\lambda, T) + \alpha_b}, \tag{1.3}$$

where $\alpha_r(\lambda, T)$ is the temperature and wavelength-dependent resonant absorption coefficient of the cooling ion. The term α_b represents background absorption, which is assumed to be independent of temperature and wavelength,[31] though recent research calls into question the validity of that assumption[32, 33].

It is clear from the Eq. 1.3 that a high value of resonant absorption (α_r) and low detrimental background absorption (α_b) would maximize the absorption efficiency (η_{abs}), which would enhance the cooling efficiency. The detrimental absorption could be minimized by improving the material's purity. The optimization of a material's resonant absorption is a much more complicated process. Considering the saturation of absorption, the resonant absorption coefficient is reduced if one tries to increase thermodynamic cooling efficiency by increasing the Stokes shift[34]. The choice of the optimum pump wavelength should have a moderate resonant absorption and Stokes shift to maximize the cooling efficiency. The pump wavelength with the highest cooling efficiency can be predicted with temperature-dependent absorption and emission data.

The external quantum efficiency (η_{ext}) is a measure of the fraction of excited ions that transfer heat out of the material through anti-Stokes luminescence, and is given by

$$\eta_{ext} = \frac{\eta_e W_r}{\eta_e W_r + W_{nr}}, \tag{1.4}$$

where η_e is the luminescence extraction efficiency which denotes the fraction of the emitted photons that are able to escape from the material. W_r and W_{nr} are radiative and nonradiative decay rates, respectively. The ratio $W_r/(W_r+W_{nr})$ quantifies the probability of an excitation

producing fluorescence and the η_e quantifies the probability that a spontaneously emitted photon exits the system.

The cooling requirement ($\eta_c > 0$) necessitates that the $\eta_{ext}\eta_{abs}$ product in Eq.(1.2) is as close as possible to unity, which means the vast majority of optical excitations should decay radiatively, and a minimum amount of parasitic heating due to unwanted background absorption from impurities should occur.

It is known that rare-earth ions doped into low-phonon energy glasses and fluoride crystal hosts are typically associated with high external quantum efficiency ($\eta_{ext} > 99\%$) for their electronic excited states[35, 36]. As such, the corresponding RE ions are excellent candidates for solid-state laser refrigeration within these host materials.

1.3 Laser refrigeration of semiconductors

Photothermal heating is a perennial challenge in the development of advanced optical devices at nanometer length scales given that a material's optical index of refraction, bandgap, and Young's modulus all vary with temperature. For instance, reducing the mechanical motion of an optomechanical resonator to its quantum ground state requires that the temperature (T) must be much less than $h\nu/k_{\mathrm{B}}$, where ν is the mode frequency, h and k_{B} are Planck and Boltzmann constants, respectively[37]. Critically, incident laser irradiances must be kept low enough to avoid photothermal heating of the resonator above cryogenic temperatures[38, 39, 40, 37, 41]. In vacuum, it is a consistent problem that affects the accuracy of sensors or causes permanent damage[7]. The absence of conductive and convective pathways for removing excess heat from the optically-trapped particle *in vacuo* magnifies the effect of photothermal heating.

A number of stringent material properties are required for solid-state laser refrigeration of semiconductors to occur, including high optical absorption, low non-radiative relaxation rates, significant Huang-Rhys factors, and near-unity external radiative quantum efficiency[29, 42]. Zhang *et al.* reported that nanoribbons of CdS could be laser cooled by as much as 40 K below room temperature using continuous-wave optical pumping at wave-

lengths λ = 514.5 nm and 532 nm.[1] They further claimed that the thickness of the CdS material must be between 60 and 120 nm.[43] If the thickness was too small, non-radiative recombination at surfaces was hypothesized to reduce the external radiative quantum efficiency below the fundamental thermodynamic constraint for laser refrigeration to occur (∼98%). If the thickness was greater than 120 nm, the high index of refraction of CdS nanoribbons was predicted to produce a significant amount of total internal reflection and subsequent reabsorption within the cantilever, resulting in heating.

Cadmium sulfide nanostructures have been investigated for a number of applications including optically pumped nanolasers[44, 45], photocatalysis[46, 47], and, more recently, solid-state laser refrigeration[1] due to the material's direct optical bandgap[48], large electron/phonon (Frölich) interaction[49], and high external radiative quantum efficiency[1].

In 2013 Zhang *et al.* reported that nanoribbons of CdS could be laser cooled by as much as 40 K below room temperature using continuous-wave optical pumping at wavelengths λ = 514.5 nm and 532 nm.[1] This emerged as a radical way to manage the thermal energy within semiconductor nanomaterials for precision science. However, these claims have been contested[50] and remain to be reproduced by an independent study. Nevertheless, for the reasons described above, the optical refrigeration of semiconductor materials remains to be an attractive endeavour.

1.3.1 External quantum efficiency in semiconductors

The η_{ext} when written for semiconductors[51, 52] can be expressed can be modified to include the known recombination pathways as

$$\eta_{ext} = \frac{\eta_e B N^2}{AN + \eta_e B N^2 + C N^3}, \tag{1.5}$$

where the nonradiative recombination coefficient, radiative recombination coefficient, and the Auger recombination coefficient are denoted using A, B and C, respectively. The carrier population density is denoted using N.

Owing to their near-unity external quantum efficiencies[53], very recently colloidal cadmium selenide (CdSe) quantum dots have emerged as attractive candidates to induce laser refrigeration of the solution [54, 55]. In addition, the theoretical feasibility of laser refrigeration of $CsPbBr_3$ nanocrystals embedded in an aerogel matrix has also been demonstrated [56].

1.3.2 The complex refractive index

In contrast to RE-doped fluoride host crystals with $n \sim 1.4$, semiconductors frequently have real indices of refraction $n > 2$, which leads to challenges in the extracting anti-Stokes photons from the solid material. A higher index of refraction can be beneficial from the standpoint of enhancing the optical absorption of pump photons due to TIR or Mie resonances. An alternative strategy for increasing the absorption of excitation photons is to design photonic crystal cavities that could efficiently trap excitation photons, while emitting anti-Stokes photons out of the material.

Furthermore, semiconductors have significantly larger optical absorption coefficients ($\alpha_{semicon.} > 10$ cm^{-1}) in comparison with RE-doped fluorides ($\alpha_{fluoride} \approx 0.1$ cm^{-1}), implying that semiconducting materials also have significantly higher imaginary refractive indices ($k = \alpha\lambda/4\pi$). Equation 1.2 shows that the cooling efficiency (η_c) is directly proportional to the efficiency of optical absorption. However, from Equation 1.5 it is also clear that the EQE depends on how efficiently the emitted photons can be extracted out of the sample. For semiconductors with a high value of α, the extraction efficiency decreases exponentially ($\eta_e \propto \exp[-\alpha x]$) when the distance, x, that photons must travel to escape through the material increases. Li *et al.*[43] have discussed this effect in the context of CdS nanoribbons where an analysis of the EQE was done by including the thickness-dependence of η_e. It was suggested that CdS nanoribbons within the thickness range of 65 to 120 nm would have the highest EQE. Samples below this thickness range would have insufficient optical absorption while samples thicker than 120 nm would not cool due to detrimental reabsorption of anti-Stokes PL.

Given the stringent requirements for high external quantum efficiency, high optical absorption of the pump laser, and low background absorption, it is challenging to find other material systems beyond laser gain media that are capable of solid-state laser refrigeration. Given the success of laser-cooling lanthanide point defects within fluoride ceramic host crystals, it is worth considering cooling point defects in semiconductors. Recently interest in solid-state laser refrigeration of point defects in diamond [57] has motivated experiments which will be discussed later.

Chapter 2

THERMOMETRY: SIMULATION AND MEASUREMENT

2.1 General overview of heat transfer theory

Heat transfer theory is a great tool for modeling the effects of electromagnetic radiation on different materials. Based on the geometry, material properties, boundary conditions and the source, the steady state temperature gradients across an object, or the dynamic change of the gradient with time may be predicted using heat transfer theory. Primarily, the analytical method or the finite element method are used to solve the heat energy equation. The analytical method solves the energy equation by writing it in a dimensionless form for the particular geometry in question. While the finite element method does this by dividing any arbitrary geometry into discrete volumes and then writing a system of equations based on the Cartesian heat energy equation. This can be done using a variety of commercial (COMSOL) or open source software (FEniCS package for Python). However, performing calculations on Python to obtain the final temperatures by evaluating traditional functions is far easier if careful assumptions can be made to simplify the physical conditions and the energy equation is solved analytically. A general method used for obtaining the analytical solution is discussed in the following sections.

2.1.1 Geometry

In the analytical heat transfer theory, the problem becomes manageable once the geometry of the object is simplified to the closest primitive such as a cuboid, cylinder or sphere. The corresponding energy equation is then written in the Cartesian, cylindrical or spherical form. In certain cases it is beneficial to reduce the dimensionality of the problem if a very high proportion of heat transfer occurs only in certain coordinate directions. After writing

the energy equation in a general form, the equation is converted to dimensionless form by normalising the dimensions and the heat source. In the dimensionless form the equation becomes separable when it is considered as a homogeneous equation without the source and solved. The source is added later in the process to obtain the final solution.

2.1.2 Boundary conditions

While separating variables and solving the homogeneous dimensionless energy equation, eigenfunctions are obtained in each coordinate direction. The eigenfunctions have arbitrary coefficients which can be evaluated by considering the boundary conditions. Boundary conditions are written by considering the physical conditions at which the sample was mounted. Two such conditions are required in each coordinate direction to obtain the two coefficients. In the cases when a surface of the sample is attached to a large substrate, a constant temperature boundary condition may be used at that surface. When a sample's surface is in contact with a stagnant fluid, Biot numbers and flux conditions are used. Symmetry conditions such as zero steady-state flux may also be useful to set a boundary condition. When multiple coefficients satisfy the boundary conditions, an eigenvalue function is written in order to obtain a series of eigenvalues.

2.1.3 Source

The source function defines the rate of generation of heat across the geometry. To obtain the source function for the purposes of this work, the physics of interaction of light with matter was used. For a Gaussian source incident on a simple geometry, this is easily calculated using the analytical focused Gaussian beam equation. The absorption in the direction of propagation can be modeled using Beer-Lambert's law. And the presence of multiple reflections may be included analytically too. This is described in the chapter A.1. In other cases where the geometry is more complicated and morphologically dependent resonances may occur within the geometry, numerical methods such as finite difference time domain (as in chapter C.1) may be used to obtain the source function.

Both the real (n_s) and imaginary components (k) of a material's refractive index ($N = n_s - ik$) play a crucial role in determining whether or not a semiconducting material will be able to demonstrate laser refrigeration. If a solid with real index n_s is placed in a medium with a lower index ($n_m < n_s$), then Fresnel reflection will direct anti-Stokes photons back into the emitting solid based on total internal reflections (TIR) where they may be reabsorbed, leading to a reduction in the cooling efficiency. To overcome the reduced extraction efficiency due to internal reflection, a variety of techniques such as index matching layers, surface roughening, and spherical domes have been considered as strategies for increasing the efficiency of luminescence extraction [58].

2.1.4 Software implementation

Once the eigenfunctions, eigenvalue functions are obtained, the constants were entered into a Jupyter notebook (Python 3.7). The eigenfunctions and eigenvalue functions were defined. Eigenvalue functions were then evaluated using a dense array of numbers and the zero-crossings (eigenvalues) were obtained for those functions.The eigenvalues were used to evaluate the eigenfunctions, multiplied and summed according to the defined solution to obtain the dimensionless temperature change at all points in the geometry for a given time point in a multidimensional array. The temperatures were then plotted against the coordinates or versus time to understand the steady state temperature gradients or the time scales. See chapter A.4 for more details.

2.1.5 Predicting timescales

The time for a geometry to reach steady state temperatures after a source is switched on or off is primarily dependent on the dimensions and the material properties - mass density (ρ), specific heat capacity ($\hat{C}$) and thermal conductivity (κ). Boundary conditions are other parameters that effect the time scales too.

For general purposes, these characteristic timescales (τ) may be estimated using the

parameter called thermal diffusivity ($\alpha = \kappa/\rho\hat{C}$) in the following manner:

$$\tau = \frac{d^2}{\alpha}, \tag{2.1}$$

where d is the characteristic size of the structure.

However, in the case of large temperature changes and when the radiative heat flux can be considered to be significant, the blackbody-limited characteristic timescales (τ_{BB})[50] can be given using the following equation.

$$\tau_{BB} = \frac{\hat{C}}{4(\frac{A}{V})\sigma T_0^3}, \tag{2.2}$$

where A, V are the surface area and volume of the structure; σ is the Stefan-Boltzmann constant and T_0 is the surrounding temperature.

Using these estimations, the timescales for CdS nanostructures used by Zhang *et al.*[1] would show a cooling/heating timescale of $\tau \approx 30$ ms, about four orders of magnitude faster than what has been reported. This motivated further investigation into the claims by particularly measuring the laser refrigeration effect in the nanostructure using independent thermometry methods, and to analyse the heat transfer dynamics more carefully using exact heat transfer through analytical methods.

2.2 Challenges with nano-thermometry

A variety of techniques which may be used to measure the temperature of nanometer scale materials and the challenges associated with them have been discussed in the following sections.

Making direct thermal measurements of nanomaterials is challenging given that direct physical contact with thermocouples can conduct heat, limiting the minimum achievable temperatures (MAT)[59]. Non-contact optical thermometry methods based on fluorescence emission, including ratiometric themometry[19, 60, 61], differential luminescence thermometry[62], and dynamic forward light scattering[19] avoid this pitfall and allow the laser to simultaneously cool and measure the local temperature. However, these methods require irradiance-dependent calibrations. Also, pumping electronic states to induce cooling can modify their

energies and requires careful considerations to decouple the incident irradiance from cooling measurements[60].

Non-contact thermometry techniques based on spectroscopic and spin readout methods offer a great advantage over others because they prevent the possibility of a conductive heat flux being attached to the material physically. Infrared thermography is a robust technique which relies on analyzing the black body radiation emitted by a sample. However, thermography is more challenging when measuring the temperature of micrometer-sized objects. In addition, the thermography of materials which are transparent to the mid-IR wavelengths (such as GaAs) involves overcoming a number of additional experimental challenges[63].

2.3 Differential luminescence thermometry (DLT)

Many challenges with infrared thermography may be overcome using novel optical thermometry techniques such as Differential Luminescence Thermometry (DLT). DLT is a versatile technique for the measurement of temperature, which is widely used within the laser refrigeration community. Recently DLT has proven to be a viable alternative to infrared cameras for conducting fast and accurate non-contact thermometry of small or infrared-transparent materials. It enables the measurement of small temperature changes with high time resolution. DLT can be applied to any material system that exhibits a temperature-dependent change in its luminescence spectrum. The idea was adopted from Zhang and Grattan[64] and developed to measure the temperature of a bulk GaAs solid. A weak cw-probe laser is used to excite the material and the luminescence is collected using an optical fiber. The luminescence is dispersed using a monochromator and a time-gated CCD is used to collect the spectra with real-time resolution. Upon subtracting the normalized spectrum with a reference temperature spectrum, a differential luminescence spectrum is obtained which can be calibrated using a cryostat. A temperature sensitivity of 100 μK was obtained by using a 12 μW, 785 nm probe laser [63]. Further enhancement of the technique using reduced sampling and balanced photodetectors for each wavelength band has resulted in two-pixel DLT which is capable of millikelvin and millisecond temperature and time resolutions, respectively[62]. Two-band

DLT is another variant of essentially the same technique which analyzes the spectral distribution from Yb^{3+} emission by isolating two bands from the spectrum using interference filters. The signal is obtained by dividing the difference of two bands with their sum. More recently, a 7 mK temperature resolution was obtained for RE-doped materials.[65]

2.4 Pump-probe luminescence thermometry (PPLT)

In 2013, Zhang *et al.* reported that nanoribbons of CdS could be laser cooled by as much as 40 K below room temperature using continuous-wave optical pumping at wavelengths $\lambda =$ 514.5 nm and 532 nm.[1]

A pump-probe luminescence thermometry (PPLT) approach was used by Zhang *et al.*[1] to explore CdS laser refrigeration. In this method, a cooling laser at either 514 or 532 nm pumped the sample to generate anti-Stokes photoluminescence, and a subsequent probe laser at 473 nm was used to excite temperature-dependent band-edge PL, which was used to measure the temperature via a Varshni calibration[1]. Time constants on the order of several minutes were observed for the sample to warm back to room temperature after the cooling laser was turned off. This same method was used to claim laser refrigeration of pervoskites[66]. One challenge in interpreting photoluminescence data is that band-edge energies are also dependent on the carrier excitation density[67]. This motivates a need for experimental optical thermometry methods that are non-contact and independent of excited carrier densities.

2.5 Optomechanical thermometry

Optomechanical thermometry is one such method that overcomes the limitations of PPLT. The foundations for optomechanical thermometry were laid by Smith *et al.*[68] During my research I worked to refine the technique, validate it and apply it to a variety of systems to obtain many novel results.

Optomechanical thermometry is akin to observing the fundamental acoustic eigenfrequency of the cantilever using forward-scattered continuous-wave laser interferometry, anal-

ogous to the softening of breathing modes with increasing laser powers[69] measured by ultrafast time-resolved studies[70] in metal nanostructures. A modified Euler-Bernoulli beam model was used to interpret the data by accounting for temperature-dependent changes in the material's Young's modulus and optical dipole-trapping forces[71] that act on the suspended cantilever.

In this technique for thermometry of a nanometer scale cantilever the Young's modulus is the primary temperature-dependent observable. Measurements of the cantilever's fundamental acoustic eigenfrequency at low laser powers showed a red-shift in the eigenfrequency with increasing power, suggesting net heating. At high laser powers, a decrease in the rate of red-shift of the eigenfrequency is explained using Euler-Bernoulli elastic beam theory, considering Hookean optical-trapping force.

For a beam that has been freely suspended from the edge of a substrate, the resonant acoustic frequency can be measured by collecting the forward scattered light transmitted through the material using an avalanche photodiode and Fourier transforming the voltage signal. The displacement z of a cantilever of uniform cross sectional area A at a position x along the length and time t can be described by the Euler-Bernoulli equation

$$\rho A \frac{\partial^2 z}{\partial t^2} + \frac{\partial^2}{\partial x^2}\left[EI\frac{\partial^2 z}{\partial x^2}\right] - F(x,t) = 0, \tag{2.3}$$

where E is the Young's modulus, I is the second moment of inertia, ρ is the density, and A is the cross-sectional area. It can be shown that the radiation pressure acting on the cantilever is minimal at the low laser irradiances used, the force acting on the cantilever ($F(x,t) = 0$). The resulting equation can be solved to give the frequency f_i of the i^{th} mode of the cantilever of length L and thickness h as[68]

$$f_i = \frac{\beta_n^2}{4\sqrt{3}\pi}\frac{h}{L^2}\sqrt{\frac{E}{\rho}}, \tag{2.4}$$

for which the solutions β_n are given using

$$1 + \cos\beta_n \cosh\beta_n = 0. \tag{2.5}$$

Although several parameters will have a temperature dependence, it has been shown[72] for cantilevers comprised of a single material that the dominating factor is the temperature dependence of the Young's modulus.

2.5.1 Effect of Optical Trapping Stiffness

It is important to note that although the radiation pressure force would cause a minimal deflection, it would not affect the eigenfrequency as no real mass is added to the system (see appendix). Deconvolution of heating and trapping effects in the high laser irradiance range can be accomplished analytically by using a modified Euler-Bernoulli elastic beam model[73] for a uniform cross section cantilever is modified with a spring attached at the tip of the cantilever. The eigenfrequency (f_i) of the i^{th} mode can be modeled according to the following equation [74]:

$$f_i = \frac{1}{2\pi}\frac{\Omega_i^2}{L^2}\sqrt{\left(\frac{EI}{\rho}\right)}, \tag{2.6}$$

For a beam of length L and linear density ρ, E and I are the Young's modulus and area moment inertia of the crossection of the beam, respectively. The i^{th} eigenvalue of non-dimensional frequency coefficient Ω_i, can be obtained by solving the eigenfunction for a given value of spring stiffness (K)[74].

$$-\left(\frac{K}{\Omega_i^3}\right)\left[\cos\Omega_i \sinh\Omega_i - \sin\Omega_i \cosh\Omega_i\right] + \cos\Omega_i \cosh\Omega_i + 1 = 0. \tag{2.7}$$

2.5.2 Effect Due to Mass and Optical Trapping Stiffness

To obtain the absolute change in temperature for a beam with mass ($Yb:LiYF_4$) being probed using a focused Gaussian spot, it is important to view the system through a modified Euler-Bernoulli beam theory and include the effects of the laser trapping forces[6] on the $Yb:LiYF_4$ crystal, which acts as a spring at the end of the cantilever. With increased irradiances, due to the increased force constant of the spring, the eigenfrequency of the cantilever increases.

Analytically the eigenfrequency (f_i) in hertz, of a uniform rectangular beam is given by[74]:

$$f_i = \frac{1}{2\pi}\frac{\Omega_i^2}{L^2}\sqrt{\frac{EI}{\rho}}. \tag{2.8}$$

Here L is the length, ρ is the linear density, E is the Young's modulus, and I is the area moment inertia of the cross section of the beam. The i^{th} eigenvalue of the non-dimensional frequency coefficient Ω_i satisfies the following equation for a uniform rectangular cantilever with a mass M_0 and spring of spring constant K attached at the free-end of the cantilever of mass m_0.

$$-\left(\frac{K}{\Omega_i^3}-\frac{\Omega_i M_0}{m_0}\right)[\cos(\Omega_i)\sinh(\Omega_i)-\sin(\Omega_i)\cosh(\Omega_i)]+\cos(\Omega_i)\cosh(\Omega_i)+1=0. \tag{2.9}$$

2.5.3 Temperature dependent Young's modulus

When a cantilever nanoribbon is heated (or cooled) photothermally, the laser spot heats a certain region of the nanoribbon by a greater extent than the regions further away from the spot. This temperature gradient will be evaluated more closely in the heat transfer analysis section. During steady state there is a significant temperature gradient across the ribbon attached to a conductive boundary (silicon substrate) at room temperature. Due to the temperature gradient, the Young's modulus across the Nanoribbon varies greatly. However, when the temperature calibration is done using the cryostat, the frequency of an isothermal beam is measured. Therefore, since the Young's modulus is the primary observable in the eigenfrequency method, the method does not report the maximum temperatures reached within the cantilever irradiated with a focused Gaussian spot.

The temperature profile within the cantilever during the calibration can be assumed to be isothermal. At high laser irradiances a temperature gradient is established in the cantilever, and numerical calculations must be made to correlate how measured eigenfrequency values at isothermal conditions correlate to eigenfrequencies that exist in the context of a temperature gradient. Using finite element simulations of a non-isothermal cantilever with a spatially varying Young's modulus, the measured temperatures are a close representation of a laser

heated CdSNR cantilever. For a rectangular cantilever with a uniform cross section along the length, the measured temperatures (ΔT_{ms}) are a close representation of a laser heated cantilever with a $\Delta T_{max} \approx 4 \cdot \Delta T_{ms}$ at the center of the laser spot.

2.6 Yb^{3+} emission analysis

In addition to optomechanical thermometry, Yb^{3+} emission analysis can be used to measure the internal temperature of the Yb doped crystal. This becomes a reliable complementary thermometry technique to verify the results from other methods.

2.6.1 Yb^{3+} Ratiometric Emission Analysis

The emission spectrum from Yb^{3+} ions excited using a 1020 nm laser consist of a bright anti-Stokes emission in the NIR region of 900 to 1000 nm. When the ion is in a $LiYF_4$ host lattice, the emission spectrum has distinct peaks representing the $E_6 \rightarrow E_1$ (960 nm) and $E_5 \rightarrow E_3$ (993 nm). The area under the peaks are represented as I_1 and I_2, respectively. The temperature of the Yb:$LiYF_4$ crystal can be determined using a ratiometric analysis of the fluorescence spectra. This is based on Boltzmann thermal population analysis of the truncated spectrum, by evaluating the ratio of areas under the peaks I_1 and I_2 corresponding to the dominant E_6 and E_5 transitions, and using the equation[13, 75]:

$$\frac{I_1}{I_2} \propto \exp\left(\frac{-(E_6 - E_5)}{k_{\mathrm{B}}T}\right). \tag{2.10}$$

The decrease in the natural log of the ratio (I_1/I_2) as a function of laser irradiance indicates cooling of the Yb:$LiYF_4$ crystal. This method is more reliable for small sized microcrystals (<100 μm) as larger crystals are more susceptible to reabsorption effects. Due to reabsorption, the emitted light is absorbed better near the 960 nm wavelength which may also contribute to the decrease in the ratio of I_1/I_2 and appear like cooling.

2.6.2 Full width half maximum analysis

Ytterbium ion emission consists of peaks corresponding to the transitions from each of the excited state manifolds to the ground state manifolds. When Yb^{3+} is present in an amorphous medium such as glass, the emission lines are primarily inhomogeneously broadened, meaning the peaks are broadened due to site-to-site variations of the local crystal fields. However, in the case of Yb^{3+} ions in a crystalline host since the site-to-site variation in local crystal field is minimal, the dominant form of line broadening is homogeneous. For an emission spectrum, when plotted with energy, the homogeneous Lorentzian line shapes and the inhomogeneous Gaussian shapes are convoluted. These may be resolved using Voigt line shapes[76]. In crystalline hosts, due to minimal inhomogeneous broadening, a Lorrentz line shape may suffice.

The inhomogeneous line widths (Δl) are nearly independent of temperature while the homogeneous line widths follow power law with temperature (T)[76]. In the case of Yb^{3+} in $LiYF_4$, fitting of the emission spectra with 12 different transitions with a composite 12 Lorentz function is required for a rigorous fit. This would require the fine tuning and constraining 36 different parameters. It is a highly complicated procedure, and without proper constraints 36 parameters may easily lead to an erroneous fit. For truncated spectra such as one obtained with a 1000 nm SP filter in the emission collection train, the dominant peak corresponding to the $E_6 \rightarrow E_1$ at 960 nm can be fit using a function that is the combination of a quadratic background and a Lorentzian. The T dependence can be obtained by fitting the peak in the representative peak from the spectra collected at various temperatures using a low laser irradiance. This dependence can then be used as a calibration to obtain the temperature of the crystal during operation.

The advantage of this technique is that due to the intrinsic nature of the inhomogeneous broadening, the calibration obtained would be more consistent from one crystal to another obtained from a single batch of processing, as long as all the other measurement parameters are maintained to be constant.

2.6.3 Mean Wavelength Analysis

As the temperature of the Yb:$LiYF_4$ crystal decreases, the overall mean wavelength (λ_f) of the emission red-shifts due to the Boltzmann distribution of populations in both ground and excited states. The mean wavelength of the spectrum can be obtained by calculating the "spectral centroid" representing the "center of gravity" (or the mean wavelength or the first moment).

$$\lambda_f = \frac{\sum \lambda_i I(\lambda_i)}{\sum I(\lambda_i)} \tag{2.11}$$

where the summation represents the sum over all the pixels, $I(\lambda_i)$ is the intensity and λ_i is the wavelength at the i^{th} pixel.

2.6.4 Intensity Correction

This dependence of the mean wavelength on temperature can be used as a calibration to measure the temperature of the Yb:$LiYF_4$ crystal. Since it uses the intensity from each pixel of the spectra, it is less susceptible to errors in other techniques such as ratiometric analysis or two-band differential luminescence thermometry[65] which involve using only specific parts of the spectra by manually selecting wavelength bands.

To obtain the absolute mean wavelength, it is essential that the raw spectrum ($I_{raw}(\lambda)$) is intensity-corrected ($I_{corr}(\lambda)$) using a calibrated light source to remove any instrumentation related changes in intensity over the wavelength range of the spectrometer. Performing the intensity correction on the intensity data obtained using a silicon detector being used for measurement in the near-infrared range is crucial because the detector efficiency drops precipitously in this range. The difference between the corrected and raw spectrum for a Yb:$LiYF_4$ crystal using a pulsed 1020 nm excitation, obtained using a silicon detector can be seen in Figure 2.1.

Intensity correction can be done by multiplying an intensity corrected function (ICF(λ)), which is obtained from the measured lamp spectrum ($I_{lamp}(\lambda)$) and the interpolated calibrated spectrum ($I_{calib}(\lambda)$) which should be provided with a calibrated lamp. The ICF is

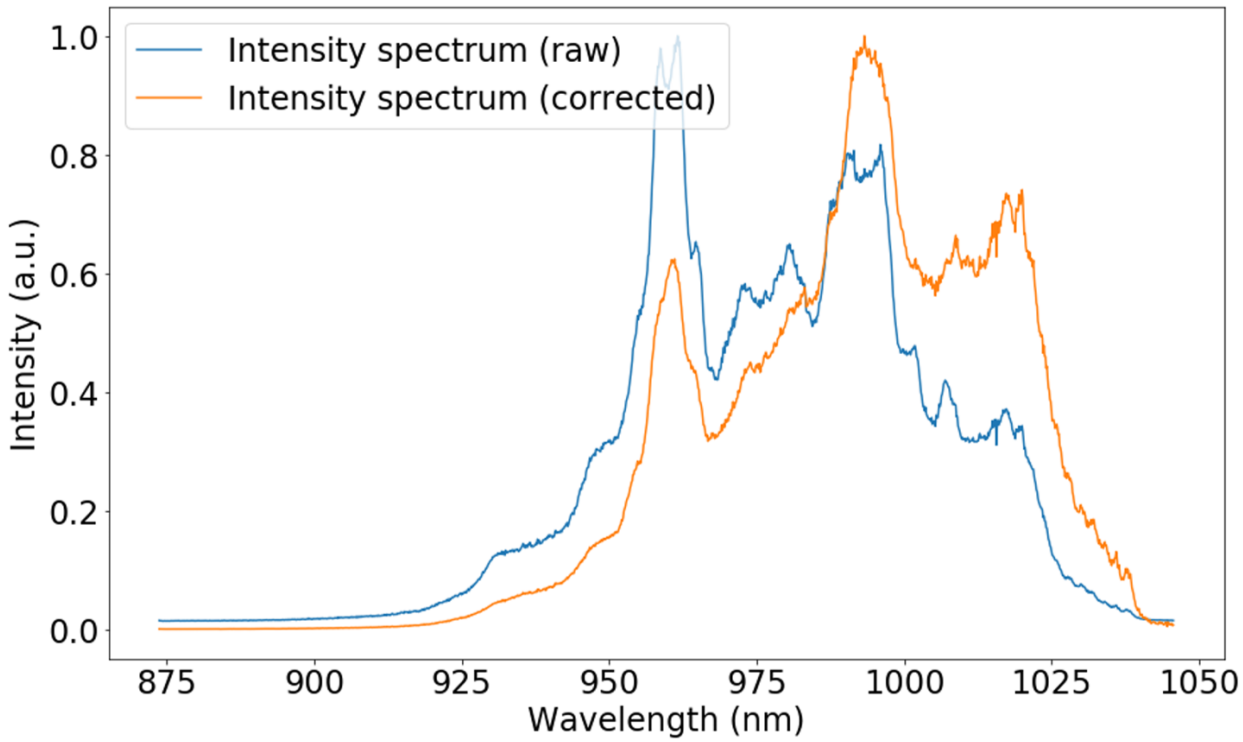

Figure 2.1: The raw (blue) and intensity corrected (orange) emission spectrum of Yb:$LiYF_4$ collected at room temperature during the decay period of a pulsed 1020 nm excitation.

given as.

$$ICF(\lambda) = \frac{I_{calib}(\lambda)}{I_{lamp}(\lambda)}. \tag{2.12}$$

The corrected intensity then is simply given as $I_{corr}(\lambda) = I_{raw}(\lambda) \times ICF(\lambda)$.

2.7 Raman anti-Stokes to Stokes ratio thermometry

In the Raman effect, inelastic scattering of light can occur when a photon excites the sample. This means that the energy of the emitted photon is either lower or higher than the excitation photon. The inelastic scattering due to a sample gives information about the molecular structure of the sample as the shift in photon energy corresponds to the vibronic signature of the molecule. When the shift of excitation photon energy is to a lower frequency, this is called a Stokes shift, or anti-Stokes when the frequency shift is to a higher frequency. The distribution of photons emitted through anti-Stokes or Stokes process maintains a Boltzmann distribution distribution law. Hence allowing a pathway to measure the temperature by non-contact method through the measurement of integrated emission intensities of the anti-Stokes and Stokes Raman line[77].

Although the center position of the Raman peaks may contain information about the temperature, it is highly sensitive to strain in the material. Another advantage of the anti-Stokes to Stokes intensity ratio is that it insensitive to strain.

This method of temperature measurement requires highly sensitive detector as the probability of inelastic Raman scattering is nearly five orders of magnitude smaller than the elastic Raleigh scattering. In addition, gratings used to disperse the photon energies need to be dense to resolve the narrow Raman lines corresponding to crystalline samples. Lastly, high density notch filters are required to eliminate the scattered excitation light from entering the spectrometer. At lower temperatures the anti-Stokes intensity may be weak or hard to detect due to florescence background. However, this thermometry method may be a great method of non-contact thermometry for nanoscale materials, near room temperatures or higher temperatures because the intensity ratio of anti-Stokes to Stokes photons approaches 1 as the temperature increases.

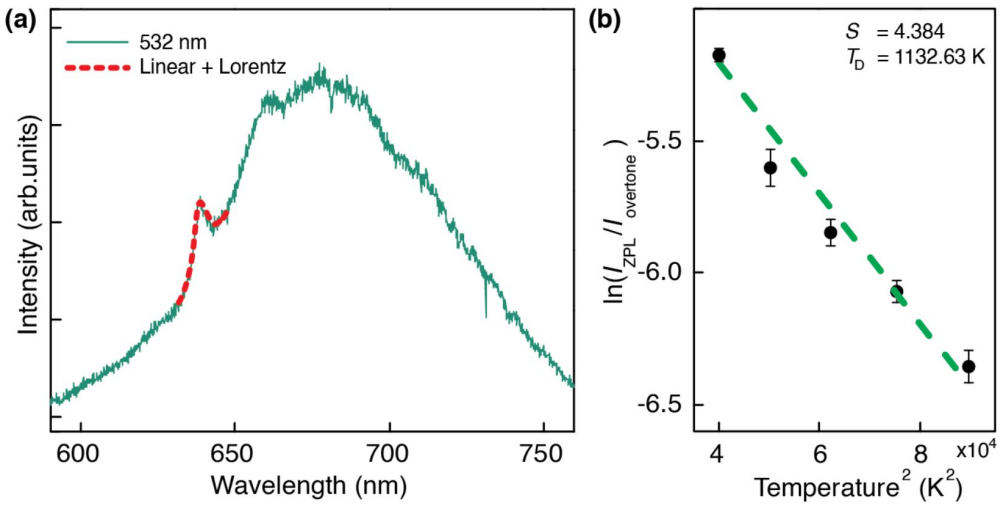

Figure 2.2: a) The room temperature emission spectrum from a nanodiamond ensemble doped with NV^- centers excited using a 532 nm laser. The red dashed line shows the composite function used to fit the ZPL. b) The natural log of I_{ZPL} to $I_{overtones}$ ratio plotted against the sample temperature at which the spectra were measured using a 532 nm laser. A dashed green line shows the fit to the equation 2.13.[79]

2.8 Debye-Waller factor (DWF) thermometry

Debye-Waller factor (DWF) is a term from condensed matter physics which measures the attenuation of x-ray and neutron scattering sciences due to thermal motion. Other names used for DWF are B-factor or temperature factor. The DWF in the case of diamonds can be evaluated by analysing the emission spectra from NV^- centers doped in it[78]. This is obtained by finding the ratio of integrated intensity from the emission of zero-phonon line (ZPL) to that from its adjacent phonon side bands (PSB). This can be done by finding the corresponding areas under the emission spectra in the respective wavelength bands.

The emission spectrum from an NV^- center doped within the diamond, as shown in Figure 2.2a consists of a narrow ZPL line around 638 nm which has a stoke shifted wide

emission from the phonon overtones. The area under the ZPL (I_{ZPL}) can be obtained by fitting the spectrum in a narrow wavelength range around the 638 nm using a composite function consisting of a linear background and a Lorentzian. The amplitude of the Lorentzian is I_{ZPL}. A representative fit for the ZPL using the composite function is shown using a red dashed line in Figure 2.2a. Area under the phonon side bands ($I_{overtones}$) can be obtained by integrating over the spectrum and subtracting the ZPL area from it. The DWF is calculated by taking the ratio I_{ZPL} to $I_{overtones}$. The change in DWF with temperature is given as[78]

$$\ln\left(\frac{I_{ZPL}}{I_{overtone}}\right) = -S\left(1 + \frac{2}{3}\pi^2\frac{T^2}{T_D^2}\right) \tag{2.13}$$

where T_D is the Debye temperatyre and S is a electron phonon coupling parameter which is closely related to the Huang-Rhys parameter[80]. The spectra of NV^-:NDs measured using a constant 532 nm laser irradiance of 0.073 MW/cm^2 and the natural log of DWF is plotted against the temperature in Figure 2.2b. The data points can be be fit to the equation 2.13 to obtain the Debye temperature (T_{D}=1132.6 K) and electron-phonon coupling parameter (S=4.38) for the particular sample. Such a calibration may be used to measure the temperature of the samples in the following measurements by simply recording the emission spectra.

This method of thermometry can be a reliable method of obtaining temperatures using the emission spectra. NV doped nanodiamonds can be very bright. The small size and the large emission rate allows for smaller collection times with high spatial resolution. In the cases where the temperature of other micrometer sized objects is to be measured by attaching the nanodiamond probes to the surface, the small size and the high thermal conductivity of nanodiamonds ensures the sample temperaure is not changed by the contact probe and steady states are reached at very high speeds (within nano to microseconds).

The downsides of this method are in the cases when overlapping emission or enhanced emission at particular wavelengths due to Fabry-Perot interference of whispering gallery modes contaminates the NV^-:ND spectral features. This may prevent proper fitting of the ZPL or the phonon overtones and give erroneous temperatures unless the background

emission is accounted for or other special fitting techniques are required. One of these techniques is described in the following section.

2.8.1 Fitting the NV⁻ spectrum

In the cases when the NV^- emission spectrum is convoluted with features that prevents the proper fitting of ZPL individually, a composite function consisting of two Lorentzian and nine Gaussian functions may be constrained heavily to fit the amplitudes of ZPL and overtones. The amplitudes can be summed and divided appropriately to give DWF. The Gaussian (G_i) and Lorentz (L_i) function used for the following fits are given as

$$G_i(\lambda; A, \mu, \sigma) = \frac{A}{\sigma\sqrt{2\pi}} e^{-(\lambda-\mu)^2/2\sigma^2} \text{ and } L_i(\lambda; A, \mu, \sigma) = \frac{A}{\pi} \frac{\sigma}{(\lambda-\mu)^2 + \sigma^2} \tag{2.14}$$

To validate this method of fitting a clean NV^- spectrum from a heavily doped macroscopic red-diamond sample was used. One Lorentzian (L_1) centered at 1.95 eV and five Gaussians (G_1-G_5) with fixed centers (μ) were used to fit the emission from the NV^- centers. The center of G1 was fixed at an energy 67.9 meV smaller than the L_1 center. To fit the NV^0 part of the spectrum, one Lorentzian (L_2) center fixed at 2.15 eV and four Gaussians (G_6-G_9) with fixed centers were used. The FWHMs (L: 2σ; G: $2\sigma\sqrt{2\ln 2}$) of all the functions were fixed as well. To obtain a fit, the amplitudes were let to vary and the Levenberg-Marquardt least squares algorithm was used. The fits are shown using red lines in Figure 2.3, the fit parameters are given in the Table 2.1. Given the areas of the individual components, they can be used to calculate the DWF by obtaining the ZPL area from ($L_1 : A$) and the overtones are obtained by summing the amplitudes obtained from the fits of all the other components. The natural log of DWF values calculated using the method discussed in the previous section are shown in the parenthesis. The magnitude of values is different, possibly due to the significant mathematical difference between the methods. However the change in their values which is the significant parameter required for measuring the change in temperature agrees well with the other method.

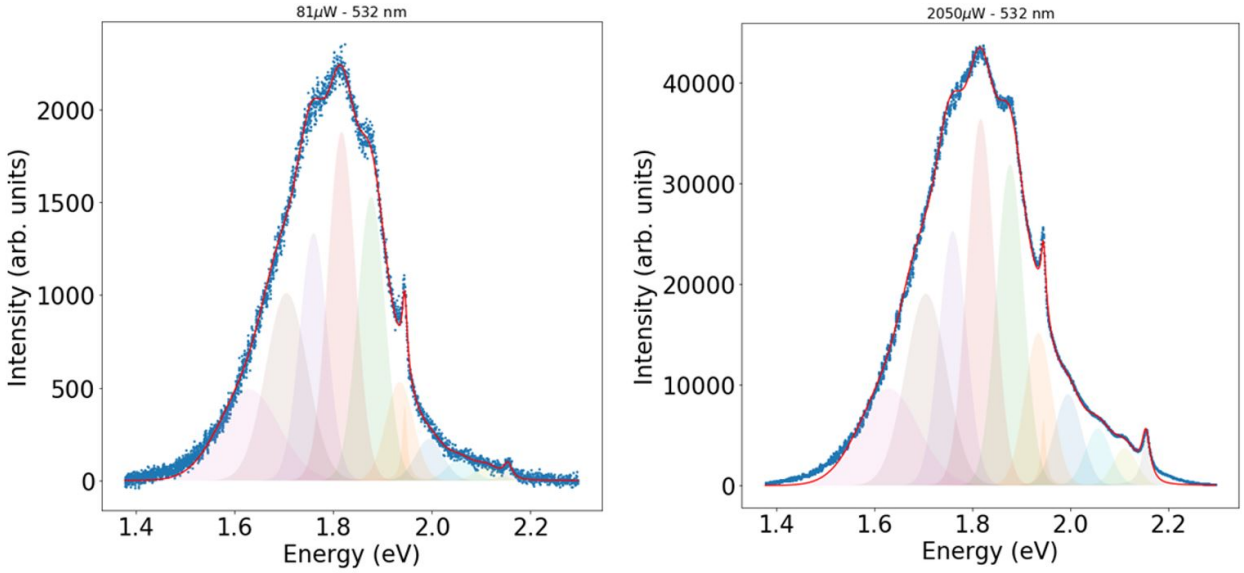

Figure 2.3: a) The NV-center spectra of the red-macro diamond is measured using 81 μW and b) 2050 μW of of 532 nm laser power focused down to a diffraction limited spot. The individual Lorentz and Gaussian components are shown using translucent filled area plots and their sum is shown using a red line.

Table 2.1: Summary of fitting results from the composite fitting function used to fit the NV^- and NV^0 emission. The natural log of DWF calculated using the method discussed in the previous section is given in the parenthesis.

Parameter	**532 nm (81 μW)**	**532 nm (2050 μW)**
L_1: A, σ **(eV)**, μ **(eV)**	7.532, 1.945, 0.006	123.88, 1.945, 0.006
G_1: A, σ **(eV)**, μ **(eV)**	107.4, 1.877, 0.028	2239.3, 1.877, 0.028
G_2: A, σ **(eV)**, μ **(eV)**	131.7, 1.817, 0.028	2555.5, 1.817, 0.028
G_3: A, σ **(eV)**, μ **(eV)**	93.59, 1.760, 0.028	1774.2, 1.760, 0.028
G_4: A, σ **(eV)**, μ **(eV)**	106.3, 1.706, 0.042	2004.6, 1.706, 0.042
G_5: A, σ **(eV)**, μ **(eV)**	75.27, 1.629, 0.061	1470.8, 1.629, 0.061
L_2: A, σ **(eV)**, μ **(eV)**	2.829, 2.154, 0.011	160.8, 2.154, 0.011
G_6: A, σ **(eV)**, μ **(eV)**	7.615, 2.111, 0.024	224.1, 2.111, 0.024
G_7: A, σ **(eV)**, μ **(eV)**	15.75, 2.056, 0.026	369.5, 2.056, 0.026
G_8: A, σ **(eV)**, μ **(eV)**	15.75, 1.995, 0.028	634.3, 1.995, 0.028
G_9: A, σ **(eV)**, μ **(eV)**	37.28, 1.935, 0.028	1062.9, 1.935, 0.028
ln(**DWF**)	**-4.348 (-5.109)**	**-4.613 (-5.489)**

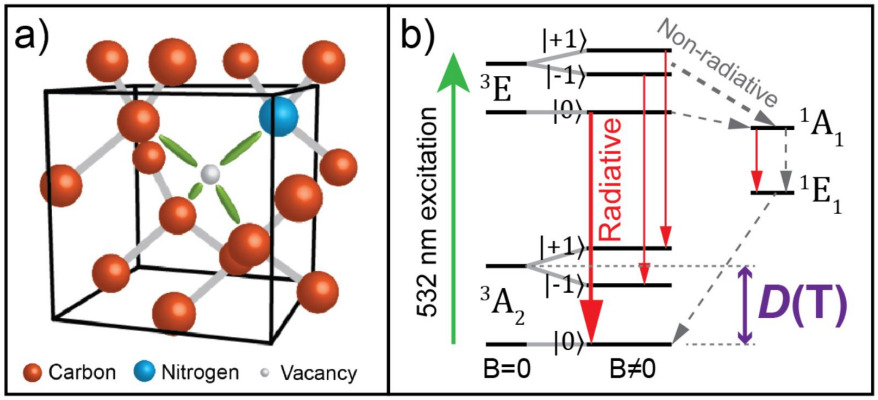

Figure 2.4: a) Physical structure of the NV^- center in diamond. b) Energy level diagram of the NV^- centers. Red arrows represent radiative transitions. The temperature dependent D-splitting parameter in the context of NV^- centre's energy level system is shown. The red arrows represent emission resulting from radiative decay. Heavier lines (as compared to a lighter lines) from the excited state to the ground state represents the stronger emission associated with m_s=0 transitions (versus the weaker emission with m_s=$\pm$1). The weaker emission at m_s=$\pm$1 results from a stronger non-radiative coupling (heavier dashed grey line) to the singlet energy system through intersystem crossing.[79]

2.9 Optically detected magnetic resonance (ODMR)

The NV^- centre is formed when a lattice vacancy coalesces with an adjacent nitrogen impurity atom within the diamond lattice, creating a spin-1 system with a trigonal C_{3V} symmetry. The emission spectrum from the centre ranges from the ZPL at 638 nm, out to 800 nm through phonon broadened transitions between the ground state ($^3A_2$) and excited state (^3E) triplets. Readout of the spin state within the ground state triplet can be performed optically using the spin-selective intersystem crossing between the NV^- excited state triplet and a pair of singlet states ($^1A_1$ and ^1E). Decay through the intersystem crossing is non-radiative, and preferentially repopulates the $m_s = 0$ ground state spin sublevel. Since the non-radiative

decay is stronger from $m_s = \pm 1$ than $m_s = 0$, a reduction in the emitted PL results if the NV^- spin has been prepared in $m_s = \pm 1$ using MW radiation prior to excitation above the ZPL (here at 532 nm). Figure 2.4a, b show the physical structure and energy level diagram of NV^- centres with the spin-selective intersystem crossing to the singlet states.[79]

In nanodiamonds, the crystal lattice is typically strained which gives rise to a splitting between the ground state spin sublevels. Thus the ground state Hamiltonian for a strained defect centre can be expressed as [81]

$$\hat{H} = D\hat{S}_z^2 + E(\hat{S}_x^2 - \hat{S}_y^2), \tag{2.15}$$

where D is the zero-field splitting parameter of 2.87 GHz, E is the splitting parameter due to non-axial strain, and $\hat{S}_x$, $\hat{S}_y$ and $\hat{S}_z$ are the respective components of the NV centre spin operator. In this picture, the separation between the $m_s = -1$ and $m_s = +1$ states is then $2E$. Since the radiative decay to these sublevels is weaker than that of $m_s = 0$, a pair of dips appear in the collected PL when the MW resonates with the $m_s = 0 \leftrightarrow m_s = \pm 1$ transitions. The ODMR measurements were conducted by scanning the MW frequency across the resonances at $D \pm E$ while optically exciting the NV^- centres at 532 nm. The centre frequency D in the ODMR scan is related to temperature by the power series expansion[82]

$$D(T) = a_0 + a_1 T + a_2 T^2 + a_3 T^3 + \Delta_{\text{pressure}} + \Delta_{\text{strain}}, \tag{2.16}$$

where a_0 = 2.8697 GHz, a_1 = 9.7 x 10^{-5} GHz/K, a_2 = -3.7 x 10^{-7} GHz/K^2, a_3 = 1.7 x 10^{-10} GHz/K^3, Δ_{pressure} = 1.5 kHz/bar is the pressure-dependent shift,[83] and Δ_{strain} is the internal strain effect depending on the diamond crystal. By calibrating the Δ_{strain} at room temperature, the actual temperature of the crystal can be calculated using the zero-field splitting parameter (D) measured from the ODMR scan.

This method may be preferable over DWF thermometry in the cases where there are overlapping emission in the 600-800 nm wavelength range. In addition since D splitting is a intrinsic parameter for the NV^- energy levels, its dependency on temperature is consistent

over different samples. This may remove the need to repeat calibration measurements for individual samples. However, it is a slower technique compared to DWF and requires collection over longer times or expensive avalanche photodiodes to obtain good signal to noise.

Chapter 3

PHOTOTHERMAL HEATING OF CDSNR

Cadmium sulfide nanostructures have been investigated for a number of applications including optically pumped nanolasers[44, 45], photocatalysis[46, 47], and, more recently, solid-state laser refrigeration[1] due to the material's direct optical bandgap[48], large electron/phonon (Frölich) interaction[49], and high external radiative quantum efficiency[1]. A number of stringent material properties are required for solid-state laser refrigeration of semiconductors to occur, including high optical absorption, low non-radiative relaxation rates, significant Huang-Rhys factors, and near-unity external radiative quantum efficiency[29, 42]. Zhang *et al.* reported that nanoribbons of CdS could be laser cooled by as much as 40 K below room temperature using continuous-wave optical pumping at wavelengths $\lambda = 514.5$ nm and 532 nm.[1] It was also claimed that the thickness of the CdS material must be between 60 and 120 nm.[43] If the thickness was too small, non-radiative recombination at surfaces was hypothesized to reduce the external radiative quantum efficiency below the fundamental thermodynamic constraint for laser refrigeration to occur ($\sim$98%). If the thickness was greater than 120 nm, the high index of refraction of CdS nanoribbons was predicted to produce a significant amount of total internal reflection and subsequent reabsorption within the cantilever, resulting in heating.[2]

3.1 Attempts at cooling CdSNR

Making direct thermal measurements of materials during laser refrigeration experiments is challenging given that direct physical contact with thermocouples can conduct heat, limiting the minimum achievable temperatures[59]. Non-contact optical thermometry methods, including ratiometric themometry[19, 60, 61], differential luminescence thermometry[62], and

dynamic forward light scattering[19] avoid this pitfall and allow the laser to simultaneously cool and measure the local temperature. However, these methods require irradiance-dependent calibrations. Also, pumping electronic states to induce cooling can modify their energies and requires careful considerations to decouple the incident irradiance from cooling measurements[60]. A pump-probe luminescence thermometry (PPLT) approach was used by Zhang *et al.*[1] to explore CdS laser refrigeration. In this method, a cooling laser at either 514 or 532 nm pumped the sample to generate anti-Stokes photoluminescence, and a subsequent probe laser at 473 nm was used to excite temperature-dependent band-edge PL, which was used to measure the temperature via a Varshni calibration[1]. Time constants on the order of several minutes were observed for the sample to warm back to room temperature after the cooling laser was turned off. This same method was used to claim laser refrigeration of pervoskites[66]. One challenge in interpreting photoluminescence data is that band-edge energies are also dependent on the carrier excitation density[67]. This motivates a need for experimental optical thermometry methods that are non-contact and independent of excited carrier densities.

The downsides of PPLT method can be minimised by the use of optomechanical method for measuring the temperature of suspended CdS nanoribbon cantilevers by observing the fundamental acoustic eigenfrequency of the cantilever using forward-scattered continuous-wave laser interferometry, analogous to the softening of breathing modes with increasing laser powers[69] measured by ultrafast time-resolved studies[70] in metal nanostructures. A modified Euler-Bernoulli beam model was used to interpret the data by accounting for temperature-dependent changes in the material's Young's modulus and optical dipole-trapping forces[71] that act on the suspended cantilever.

3.1.1 Optomechanical thermometry measurement

The cadmium sulfide nanoribbons (CdSNR) were synthesized using chemical vapor transport (CVT) process conducted in a programmable tube furnace (Lindberg Blue M). Cadmium sulfide powder (650 mg, 99.995% Sigma Aldrich) in an alumina boat was used as the source

and placed at the center of the tube furnace. The growth substrates were prepared by dropping a dilute gold nanocrystal (AuNC, 30 nm) solution in chloroform on a silicon (100) surface. The substrates were left to rest for a few minutes to allow the solvent to evaporate and then transferred onto a quartz tray. The quartz tray was loaded into a tube furnace such that the silicon substrates were downstream 7-10 cm inside the edge of the furnace. Argon + 5% H_2 was used to initially flush the chamber for 30 minutes at 400 SCCM. The flow rate was then reduced to 50 SCCM and the temperature was ramped up to the growth temperature (T_g) in 30 minutes. The growth temperature was maintained for the growth time (t_g), and the furnace was allowed to cool naturally.

Dry transfer of as-grown CdSNRs was conducted by gently inverting a cleaved silicon wafer onto the as-grown substrate. Individual CdSNRs were then removed from the transfer substrate and placed at the edge of another clean silicon substrate to form a cantilever (as shown in Figure 3.1b) using a nano-manipulator (Märzhäuser-Wetzlär) with a tungsten dissecting probe (World Precision Instruments) with a sufficiently small tip radius-of-curvature ($\sim$100 nm).

The silicon substrate loaded with the CdSNR cantilever sample was then attached via a copper tape to the stage of an optical cryostat (Janis ST-500) that was modified by drilling a hole down its center line. Cantilevers were suspended over the stage's axial hole to allow forward-scattered laser radiation to be collected from behind the chamber (Figure 3.1a,b). The chamber was pumped down to a pressure of $4.0\text{x}10^{-4}$ mbar using an oil-free turbo molecular pump. The cryostat stage was then aligned into an optical setup to measure the cantilever's eigenfrequency. A single-longitudinal-mode 532 nm laser beam (Coherent, Compass 532) was first split using a holographic transmission grating and focused on the tip of the cantilever using a 50x long working distance objective lens (Mitutoyo). The transmitted light was focused on a high-speed avalanche photo-diode (APD, Thorlabs APD430A). The voltage vs. time signal obtained from APD over one second was then Fourier transformed using a LabVIEW program to obtain one power spectrum. Thirty power spectra were averaged to obtain one measurement, as shown in the Figure 3.1c. The peak then was fit to

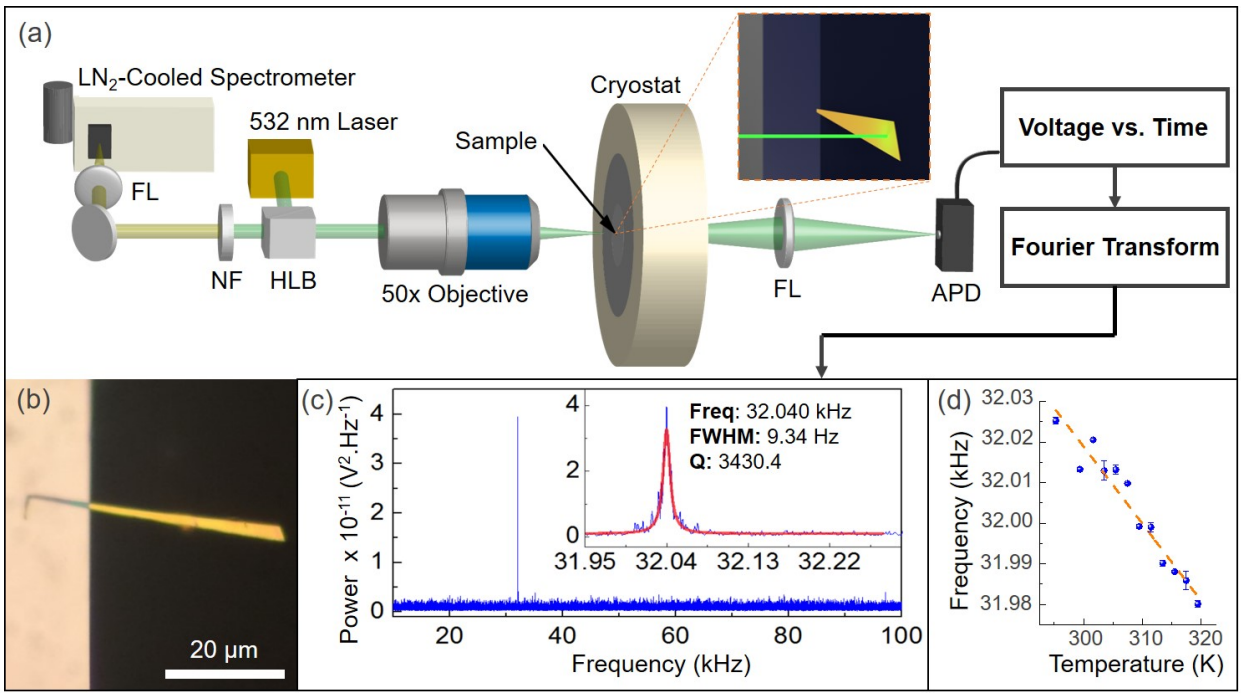

Figure 3.1: a) A schematic of the experimental setup for the eigenfrequency measurement of a CdS cantilever at the edge of a silicon chip, mounted in a cryostat under vacuum. A 532 nm laser was used as the probe, focused on to the tip of the cantilever using a 50x long working distance objective lens to a spot radius of 1.15 μm. The forward scattered light was focused onto the avalanche photodiode (APD) detector and the resultant voltage vs time is Fourier transformed to obtain the cantilever's eigenfrequency. Back-scattered light was focused onto a liquid nitrogen (LN_2) cooled spectrometer to record the PL and Raman spectra. FL, HLB and NF stand for focusing lens, holographic beam splitter cube and notch filter, respectively. b) A bright-field optical image of one cantilever resting on a silicon chip (left side) and suspended over free-space (right side). c) The Fourier-transformed signal shows a lone sharp Lorentzian peak centered at 32.040 kHz. The inset shows a magnified x-axis of the same data and a fitted Lorentzian curve in red. d) A frequency vs temperature calibration of data points is shown in blue circles and a linear least-squares fit of the data is shown with an orange dotted line.[2]

a Lorentzian shape to obtain the cantilever's eigenfrequency. An average frequency data point was obtained by fitting six measurements obtained at the same laser power with a gap of one minute between consecutive measurements. The error bars represent one standard deviation. Temperature calibration was performed by heating the cryostat using a temperature controller (Lake Shore 335, resolution: 10 mK), and measuring the eigenfrequency of the cantilever at different temperatures using a low laser irradiance (5 kW/cm^2) that does not measurably heat the sample. An average frequency data point was obtained by fitting three measurements obtained at the same temperature with a gap of one minute between consecutive measurements. The error bars represent one standard deviation.

The silicon substrate loaded with the CdSNR cantilever sample was then attached via a copper tape to the stage of an optical cryostat (Janis ST-500) that was modified by drilling a hole down its center line. Cantilevers were suspended over the stage's axial hole to allow forward-scattered laser radiation to be collected from behind the chamber (Figure 3.1a,b). The chamber was pumped down to a pressure of 4.0x10^{-4} mbar using an oil-free turbo molecular pump. The cryostat stage was then aligned into an optical setup to measure the cantilever's eigenfrequency. A single-longitudinal-mode 532 nm laser beam (Coherent, Compass 532) was first split using a holographic transmission grating and focused on the tip of the cantilever using a 50x long working distance objective lens (Mitutoyo). The transmitted light was focused on a high-speed avalanche photo-diode (APD, Thorlabs APD430A). The voltage vs. time signal obtained from APD over one second was then Fourier transformed using a LabVIEW program to obtain one power spectrum. Thirty power spectra were averaged to obtain one measurement, as shown in the Figure 3.1c. The peak then was fit to a Lorentzian shape to obtain the cantilever's eigenfrequency. An average frequency data point was obtained by fitting six measurements obtained at the same laser power with a gap of one minute between consecutive measurements. The error bars represent one standard deviation. Temperature calibration was performed by heating the cryostat using a temperature controller (Lake Shore 335, resolution: 10 mK), and measuring the eigenfrequency of the cantilever at different temperatures using a low laser irradiance (5 kW/cm^2) that does

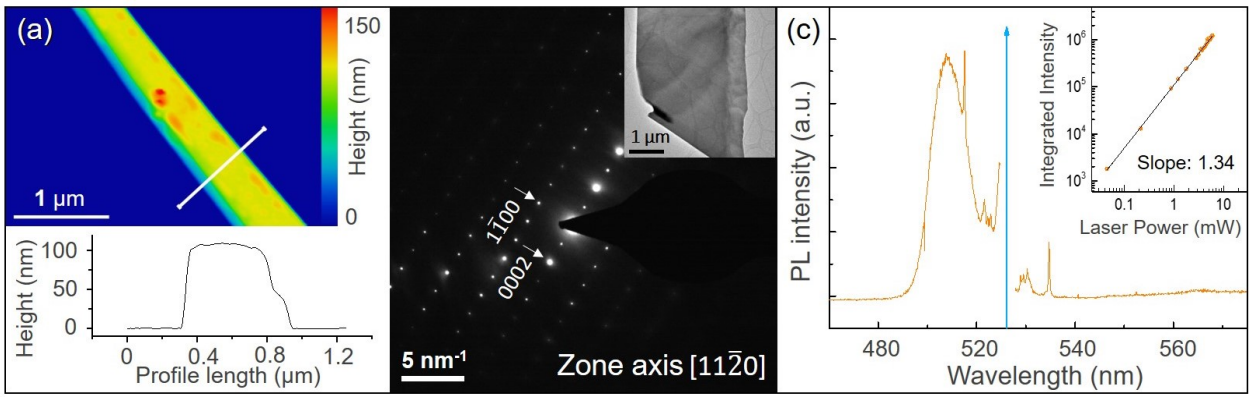

Figure 3.2: a) AFM scan of the NR surface resting on silicon, with a white profile line straddling across the NR width (top). The corresponding line profile is shown below, revealing a 110 nm thickness. b) A select area electron diffraction pattern of the NR shown in the inset. c) A room temperature PL spectrum collected from the suspended part of the cantilever, measured using an incident 532 nm laser with 2 kW/cm^2 irradiance. The inset shows a corresponding log-log plot of the integrated PL intensity as a function of the laser power.[2]

not measurably heat the sample. An average frequency data point was obtained by fitting three measurements obtained at the same temperature with a gap of one minute between consecutive measurements. The error bars represent one standard deviation.

An AFM scan (Figure 3.2a) of the cantilever surface resting on the silicon wafer demonstrates that the surface of the cantilever is flat with a thickness of 110 nm, and a surface RMS roughness <1 nm. Consistent with extensive TEM diffraction studies on isomorphic ZnTe NRs[84], TEM SAED (Figure 3.2b) of the CdSNR shows a single crystal wurtzite diffraction pattern from the [11$\bar{2}$0] zone axis of a representative NR sample, with the planes [1$\bar{1}$00] and [0002] marked. A room temperature photoluminescence spectrum collected from the suspended part of a representative cantilever sample (Figure 3.2c) using a 532 nm excitation source shows a typical band-to-band anti-Stokes PL curve centered around 510 nm, matching the spectra reported by Zhang *et al.*[1] Recently reported time-resolved measurements

indicate that the anti-Stokes luminescence is produced from optical transitions between real states[85]. Peaks in the PL at 299 cm^{-1} and 600 cm^{-1} correspond to the 1LO and 2LO phonon modes, confirming the high crystallinity of CdSNRs. The red-shift in the 1LO mode in these measurements compared to the reported Raman modes for a single crystal of bulk CdS[86] at 305 and 600 cm^{-1} can be attributed to the phonon confinement effect in the nanostructure[87, 88, 89]. The peaks at 204 and 245 cm^{-1} stem from the surface reconstruction of the CdSNR[90]. The inset of Figure 3.2c shows an integrated PL intensity with laser power, depicting no apparent saturation of intensity at laser powers as high as 8 mW or an irradiance of 192.4 kW/cm^2. It is important to note that although some cantilever structures were observed to withstand high power laser irradiation as mentioned above, most cantilevers decomposed at irradiances as low as 72 kW/cm^2. This discrepancy may arise from local variations in the material's absorption coefficient, or morphology dependent resonances (MDRs)[91, 92] which can cause a peak in absorption for certain thicknesses near 102 nm as shown in Figure 3.3. To avoid any permanent damage to the samples during the eigenfrequency experiments, laser irradiances were kept under 43.3 kW/cm^2, corresponding to a total laser power of 1.8 mW in a spot diameter of 2.3 μm.

An interesting blue-shift of eigenfrequency was observed immediately after loading the sample into the cryostat. A representative sample was loaded and the eigenfrequency was continually recorded with a laser beam irradiance of 11.5 kW/cm^2 over a period of 2 hours, during which it shifted from 31900 Hz to a steady state value of 32060 Hz (Figure 3.4a). Upon switching off the laser overnight and repeating the measurement, the eigenfrequency remained stable within standard deviations of a higher steady state value around 32020 Hz over 40 minutes. All of the eigenfrequency measurements discussed below were conducted after irradiation of the cantilever tip for two-hours when the eigenfrequency reached a steady state value. The blue-shift suggests that laser induces an irreversible modification of the the mass distribution of the cantilever around the incident laser spot area and reaches a steady state. Although a blue-shifting frequency trend could be attributed to the cooling of the cantilever structure, the observed irreversible change in the eigenfrequency is inconsistent

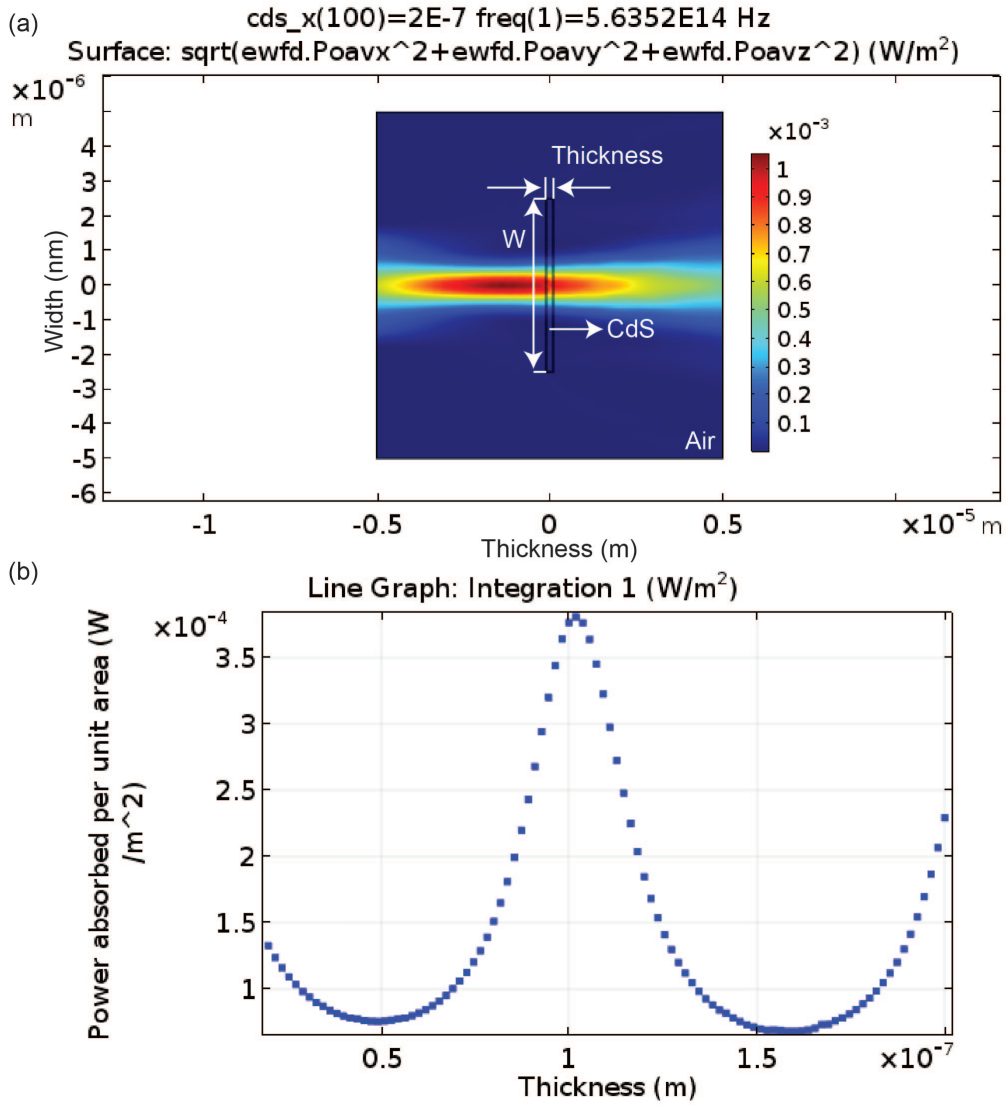

Figure 3.3: a) Using the wave optics package within the finite element program COMSOL a 2D section of the cantilever was modeled. A z-polarized Gaussian electric field of arbitrary magnitude ($w_0 = 1.15$ μm at $x = 0$) was incident on a slab of $W = 5$ μm and refractive index value of $n = 2.5513 - i0.0057657$. b) The thickness (H) was varied from 20 to 200 nm and the integrated power within the slab was calculated. The integrated power at every thickness was normalized using the area (W x H) for each thickness to obtain the average power absorbed per unit area of the section. The variation in average power absorbed per unit area with thickness is shown. A peak in average absorbed power per unit area at thicknesses near 102 nm represents a morphology dependent resonance (MDR).[2]

with this laser-cooling hypothesis. Surface adsorbates may desorb upon irradiation, decreasing the cantilever's local linear mass density, and leading to a blue-shift in the measured eigenfrequency.

The data in Figure 3.4b,c were acquired at random laser irradiances to account for potential hysteresis effects or irreversible desorption of foreign species. Figure 3.4b demonstrates a red-shift in eigenfrequency with an increasing laser irradiance in the low laser irradiance range (<2.5 kW/cm^2). A least-squares linear fit to the data is shown using a red-dotted line. The y-axis intercept of the linear fit was used to obtain the first natural resonant frequency mode ("diving board mode") of the cantilever of 32071 Hz at room temperature in the absence of laser perturbation. The decrease in eigenfrequency in the low irradiance range can be attributed to a decrease in the Young's modulus of the material as the cantilever heats up with increase in laser irradiance. The magnitude of the measured increase at the hottest point within the cantilever (ΔT_{max}) of the cantilever, estimated using the aforementioned temperature calibration is shown using a green line in the right y-axis. Using this, a ΔT_{ms} (ΔT_{max}) of 20.6 K (82.4 K) above room temperature at a laser irradiance of 2.5 kW/cm^2 was determined. Temperature measurements made on CdSNRs from Zhang *et al.*[1], using the same method also suggested heating.

Using COMSOL[93] finite element analysis, the geometry of the cantilever was modeled and the first eigenfrequency mode was probed by varying the Young's modulus from 44 to 46 GPa. A linear increase of eigenfrequency from 32831 Hz to 33569 Hz with increasing Young's modulus (slope: 368.9 Hz/GPa) was observed. Based on the unperturbed natural resonant mode of 32071 Hz, a Young's modulus of 41.9 GPa was extracted from a linear fit to the data obtained from the simulation. This is in agreement with the reported averaged tensor value of 45 GPa [94].

Measurements made over the full laser irradiance range (0.8-43 kW/cm^2, Figure 3.4c), show the eigenfrequency change as a function of laser irradiance. Eigenfrequencies appear to fall on an exponential decay curve (solid green line) which can be interpreted in the context of laser induced heating (heating component) and optical trapping stiffness (trapping

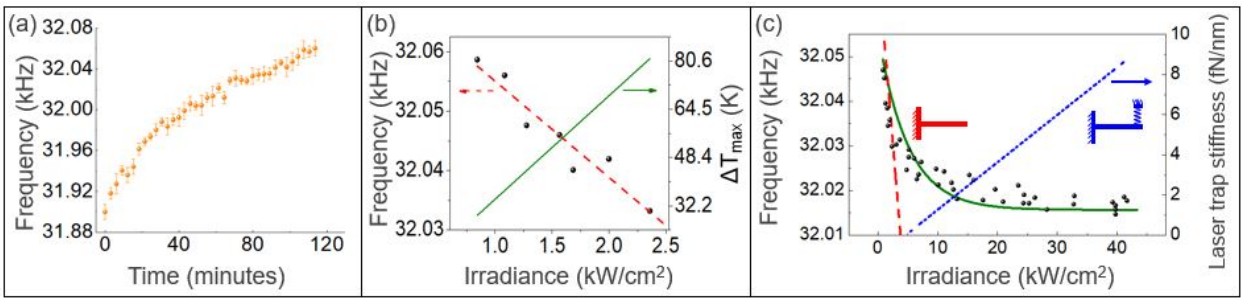

Figure 3.4: a) A blue-shift and eventual saturation of the eigenfrequency observed when measurements were done immediately after loading the cantilever sample into the cryostat, with a 11.5 kW/cm^2 laser irradiance for a span of 2 hours. b) Eigenfrequency measurement at low laser irradiances (below 2.5 kW/cm^2) shows a linear red-shift of eigenfrequency with increasing laser irradiance. A least-squares linear fit is shown using a red dotted line. Based on the temperature calibration, a green line shows the variation of the ΔT_{max} on the right vertical axis. c) Eigenfrequency measurement data points shown as black dots on the cantilever taken at random laser irradiances to account for hysteresis. The data fits to an exponential decay curve shown in solid green line. Young's modulus dependent frequency shift component dominant at low laser irradiances has been shown using a dashed red line, while at higher irradiances the laser trapping stiffness component obtained by subtracting the heating component from the exponential fit has been shown as a dotted blue line. The laser trap stiffness values estimated using theory have been shown in the right vertical axis.[2]

component). The optical trapping stiffness originates from a negative pressure gradient force generated due to a tightly focused single beam of laser, which has been shown to trap particles from 25 nm to 10 μm[71]. At low irradiances, the linear red-shift in the eigenfrequency can be attributed to a decrease in the Young's modulus of the material as the cantilever heats up with increase in laser irradiance (dashed red line). This corresponds to a rise in ΔT_{ms} (ΔT_{max}) of 371 K (1494 K) and a decrease of the Young's modulus to 40.03 GPa for a frequency red-shift of 701.2 Hz at a laser irradiance of 43 kW/cm^2. At high laser irradiances, the optical-trapping stiffness becomes significant and causes a decrease in the rate of the eigenfrequency's red-shift. The measured frequency at high irradiances is thus the net result of heating and laser-trapping components, shown using dashed red line and a dotted blue line, respectively in Figure 3.4c. The dotted blue line representing the laser trapping stiffness experienced by the cantilever was obtained by subtracting the heating component (dashed red line) from the exponential fit (green line) and was further used to estimate its value at different laser irradiances using static structural simulation in COMSOL. The estimated trapping stiffness is shown in the right vertical axis in Figure 3.4c. It is important to note that although the radiation pressure force would cause a minimal deflection , it would not affect the eigenfrequency as no real mass is added to the system. Deconvolution of heating and trapping effects in the high laser irradiance range can be accomplished analytically by using a modified Euler-Bernoulli elastic beam model[73] for a uniform cross section cantilever is modified with a spring attached at the tip of the cantilever discussed in section 2.5.

For a beam length, width, and height of 20 μm, 5 μm, and 110 nm, E = 45 GPa and a density of 4826 Kg/m^3, the calculated eigenfrequency of the first mode increases (blue-shifts) linearly from 7.0 and 70.3 Hz as the spring constant changes from 1 to 10 fN/nm , showing an increased blue-shift for higher spring constant. As the analytical model is only valid for beams with uniform cross section, a finite element analysis was used to model the effects of a spring with stiffness (K) at the end of a cantilever geometry modeled based on the sample dimensions to quantify the magnitude of optical trapping stiffness observed experimentally.

The component of eigenfrequency that blue-shifts with increasing laser irradiance due

to an increasing trapping force is shown as a dotted blue line in Figure 3.4c, indicating an increase in eigenfrequency with increasing irradiance, in the absence of heating. This was obtained by subtracting the heating component (dashed red line) from the exponential fit (green line). The resultant irradiance-dependent blue-shift was used to quantify the laser trapping stiffness at high laser irradiances and is plotted in the right vertical axis of the plot (Figure 3.4c). Starting from a laser irradiance of 4.6 kW/cm^2, the laser trapping stiffness is significant enough to affect the eigenfrequency and reaches a maximum of 9.1 fN/nm at 43 kW/cm^2.

3.1.2 Cantilever heat transfer theory

Analytical heat transfer analysis predicts the temperature distribution within the nanostructures and allows us to calculate the time required to reach steady state temperatures. This approach is useful for investigating solid-state laser refrigeration or photothermal heating of a wide variety of material systems without using inexact finite element methods. In this section, the heat transfer equations for various geometries, boundary conditions and source types are solved analytically. Note that the radiative heat fluxes are ignored in the models due to due to a small Biot number and extremely small characteristic length scales involved here.

To examine the effects of photothermal heating of a rectangular CdS nanoribbon due to a focused Gaussian laser beam we consider a rectangle length L, width W, and thickness H as shown in Figure 3.5. It is convenient to write the energy equation for the photothermally heated ribbon in dimensionless form given by

$$\frac{\partial U}{\partial \tau} = a^2 \frac{\partial^2 U}{\partial \xi^2} + \frac{\partial^2 U}{\partial \eta^2} + b^2 \frac{\partial^2 U}{\partial \zeta^2} + \sigma, \tag{3.1}$$

where the dimensionless parameters are defined by

$$U = \frac{T - T_0}{T_0},\ \tau = \frac{\alpha t}{L^2},\ a = \frac{L}{W}, b = \frac{L}{H},\ \xi = \frac{x}{W},\ \eta = \frac{y}{L},\ \zeta = \frac{z}{L},\ \sigma = \frac{L^2}{\kappa T_0}\dot{Q}'''. \tag{3.2}$$

Here $\alpha = \kappa/\rho C$ is the thermal diffusivity of the nanoribbon, T_0 is the temperature at its base ($y = 0$), and the approximation for the electromagnetic energy absorbed by the medium

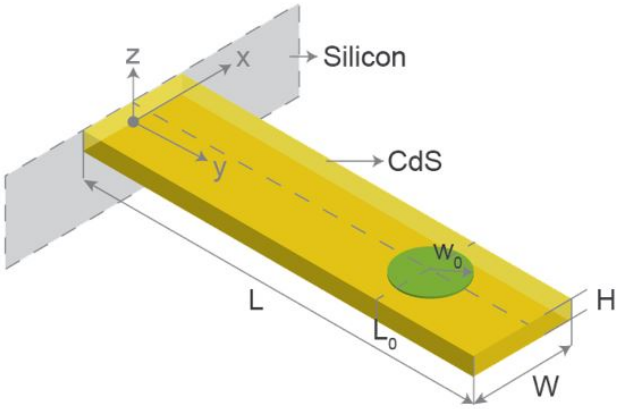

Figure 3.5: The rectangular geometry used for analytical transient heat transfer model.[2]

per unit volume per unit time at a radial distance of r from the center of the beam with a waist radius of w_0 and wavelength λ_0 *in vacuo* is given as

$$\dot{Q}'''(r,z) = \frac{4\pi n''}{\lambda_0} I_0(1-R_\lambda)\exp\left(-\frac{2r^2}{w_0^2}\right)\exp(-2k''z), \tag{3.3}$$

where I_0 is the incident irradiance, R_λ is the wavelength-dependent reflectivity, n'' is the imaginary part of refractive index of the medium, and k'' is the corresponding wavenumber ($k'' = 2\pi n''/\lambda_0$).

The nanoribbon is mounted in a vacuum chamber. Therefore, convective or conductive heat transfer from the suspended surfaces can be neglected. Furthermore, due to a small Biot number the radiant heat fluxes are extremely small for the temperatures and characteristic length scales involved here. Therefore, the boundary conditions are given by:

$$\frac{\partial U}{\partial \xi}(0,\eta,\zeta,\tau) = \frac{\partial U}{\partial \xi}(1,\eta,\zeta,\tau) = \frac{\partial U}{\partial \zeta}(\xi,\eta,0,\tau) = \frac{\partial U}{\partial \zeta}(\xi,\eta,1,\tau) = 0 \tag{3.4}$$

and

$$U(\xi,0,\zeta,\tau) = 0, \ \frac{\partial U}{\partial \eta}(\xi,1,\zeta,\tau) = 0, \tag{3.5}$$

We look for a classical product solution of the form

$$U\big(\xi,\eta,\zeta,\tau\big)=\sum_{l=0}^{\infty}\sum_{m=0}^{\infty}\sum_{n=0}^{\infty}A_{lmn}(\tau)X_l(\xi)Y_m(\eta)Z_n(\zeta), \tag{3.6}$$

in which the orthonormal eigenfunctions $X_m(\xi)$ and $Y_n(\eta)$ satisfy homogeneous boundary conditions and are given by

$$X_l(\xi)=1 \text{ for } l=0 \text{ and } \sqrt{2}\cos(l\xi\pi) \text{ for } l=1,2,3,... \tag{3.7}$$

$$Y_m(\eta)=\sqrt{2}\sin\left(\left(m+\frac{1}{2}\right)\eta\pi\right) \text{ for } m=0,1,2,... \tag{3.8}$$

$$Z_n(\zeta)=1 \text{ for } n=0 \text{ and } \sqrt{2}\cos(n\zeta\pi) \text{ for } n=1,2,3,... \tag{3.9}$$

where prime indicates a dummy variable, and the coefficients of $A_{lmn}(\tau)$ are given by

$$A_{lmn}(\tau)=\frac{[1-\exp(-\gamma_{lmn}^2\tau)]}{\gamma_{lmn}^2}\int_0^1\int_0^1\int_0^1\sigma(\xi'\eta'\zeta')X_l(\xi')Y_m(\eta')Z_n(\zeta')d\xi'd\eta'd\zeta', \tag{3.10}$$

where

$$\gamma_{lmn}^2=(al\pi)^2+\left[\left(m+\frac{1}{2}\right)\pi\right]^2+(bn\pi)^2. \tag{3.11}$$

The steady state solution is obtained by taking the limit as $\tau\to\infty$.

Note that σ vanishes outside of a region surrounding a cylinder with origin $x=W/2$, $y=L_0$ (or $\xi=1/2$, $\eta=\eta^*=L_0/L$). It is assumed that the radius of that region is $W/2$, the half width of the nanoribbon. The double integral over the circular region can be obtained by quadrature using an appropriate numerical integration software (See appendix for details). Calculations were performed using the solution above with a thermal conductivity (κ) of 20 W/(m·K), $n=2.5513$-$i0.0057657$ and 2.6399-$i0.055754$ at 532 nm and 514 nm laser wavelengths respectively, laser spot radius $w_0=1.15$ μm, $L=20$ μm (spot center at 0.75*L), $W=5$ μm, $H=110$ nm, $P_0=1.8$ mW, a ΔT_{ms} (ΔT_{max}) of 9.7 K (38.6 K) and 87.5 K (350 K) is predicted for 532 and 514 nm incident lasers respectively, indicating the importance of the imaginary refractive index (Figure 3.6a,b). In the calculations, a laser power of 1.8 mW was reduced to account for Fresnel reflection at normal incidence using R_λ values of 0.19081 and 0.20317 at 532 and 514 nm, respectively. A calculated steady state

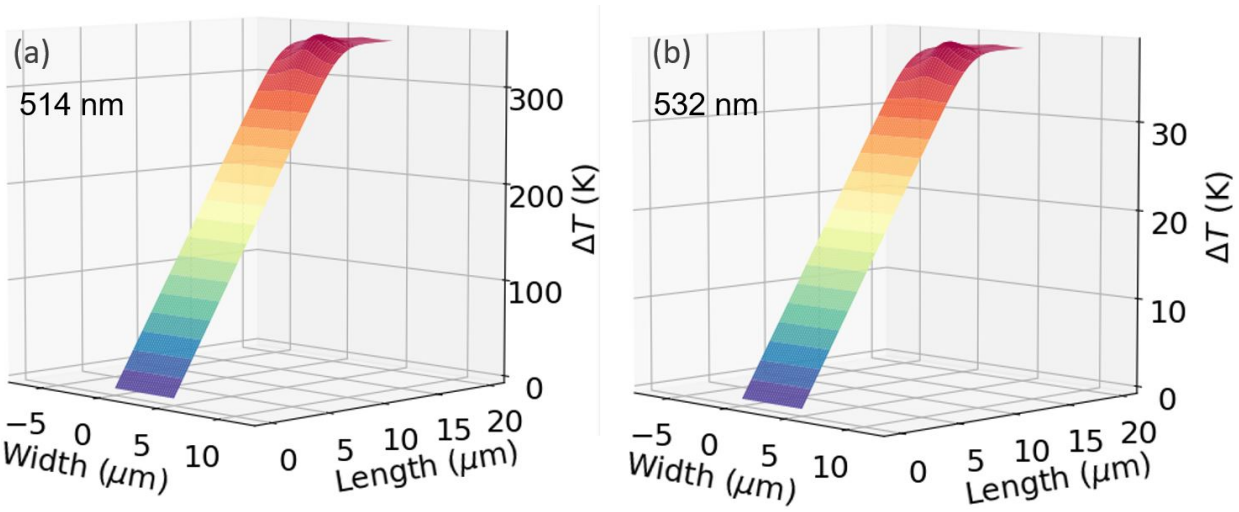

Figure 3.6: a) The steady state surface temperature deviation from the ambient temperature (ΔT) of a CdS cantilever calculated for a thermal conductivity (κ) of 20 W/(m·K), n = 2.5513-i0.0057657, R_λ = 0.19081 (at 532 nm), laser spot radius w_0 = 1.15 μm, L = 20 μm, W = 5 μm, H = 110 nm, P_0 = 1.8 mW. b) The ΔT profile of a CdS cantilever calculated for the same parameters as b, P_0 = 1.8 mW and optical constants for 514 nm - n = 2.6399-i0.055754 and R_λ 0.20317 (at 514 nm).[2]

temperature deviation from the boundary temperature condition (ΔT) profile at the surface during irradiation with the 532 nm and 514 nm laser has been plotted in Figure 3.6a and b, respectively. Although the values on the temperature axis change, the general profile of the plot shown in Figure 3.6a and b remained the same for various laser powers.

Table 3.1: Summary of results from temperature calculations using different parameters in the analytical model. The experimentally measured values of ΔT_{ms} are shown in parentheses.[2]

L, W, H (μm)	λ_0 (nm)	Reflectivity (R_λ)	Refractive Index (n)	P_0 (mW)	ΔT_{max} (K)	ΔT_{ms} (K)
20, 5, 0.11	532	0.19031	2.5513-i0.0057657	1.8	38.6	9.57
20, 5, 0.11	514	0.20317	2.6399-i0.055754	1.8	350	86.8
35, 2.3, 0.11	532	0.19031	2.5513-i0.0057657	0.1	6.69	1.66
35, 2.3, 0.11	532	0.19031	2.5513-i0.0057657	1.8	120	29.8
35, 2.3, 0.11	532	0.19031	2.5513-i0.082112	0.1	83	20.6 (20.6)
35, 2.3, 0.11	532	0.19031	2.5513-i0.082112	1.8	1494	371 (371)

For a rectangular geometry with $L = 35$ μm, $W = 2.3$ μm, $H = 110$ nm (similar to the NR used for eigenfrequency measurements) using the same optical constants mentioned above, and input 532 nm laser powers of 100 μW and 1800 μW, the ΔT_{ms} (ΔT_{max}) were 6.69 K (1.66 K) and 120 K (29.8 K), respectively. Compared to the experimentally measured ΔT_{ms} (ΔT_{max}) of 20.6 K (82.7 K) at 100 μW, the analytical calculation underestimates the magnitude of temperature rise. This deviation can be attributed to a variation in the value of the imaginary part of the refractive index probably due to impurities or non-stoichiometry of the CdSNR. A comparison between the experimentally observed and theoretically predicted temperature allows an estimation of the imaginary refractive index of the CdSNR. A ΔT_{ms} (ΔT_{max}) of 20.6 K (83 K) at 100 μW of laser power was obtained using an imaginary refractive

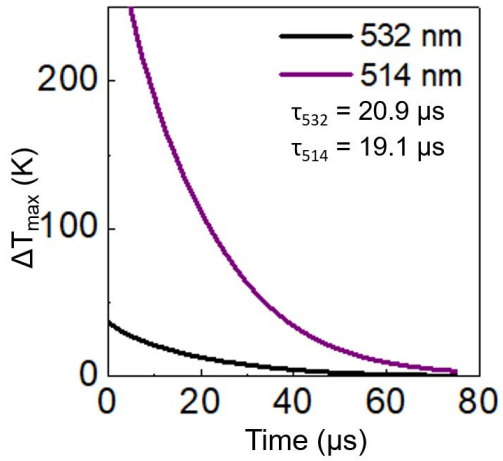

Figure 3.7: The calculated cooling curve depicting the decay in the maximum steady state temperature (ΔT_{max}) with respect to time after the cantilever reached steady state temperatures and then the source was switched off. For comparison, the cooling curves calculated for the same geometry and respective optical constants for 532 nm and 514 nm are shown.[50, 2]

index of 0.082112 rather than that reported by Treharne *et al.*[95] ($n'' = 0.0057657$). This estimated imaginary refractive index predicts a ΔT_{ms} (ΔT_{max}) of 371 K (1494 K) at 1800 μW, which is in agreement with the experimentally measured ΔT_{ms} (ΔT_{max}) of 371 K (1494 K) for the same laser power. Similar values of the steady state temperature obtained using the analytical model have been confirmed using finite element software (COMSOL). The results of calculations using various parameters discussed have been summarized in Table 3.1. Values of $w_0 = 1.15$ μm and $\kappa = 20$ W/(m·K) were used for all the tabulated calculations.

The transient heat transfer model from a finite element model for a cantilever beam irradiated by a 532 nm laser, suggests time scales of 80 μs to reach within 0.1% of T_0 after the laser beam heat source is turned off. The ΔT_{max} vs. time profiles have been plotted in Figure 3.7. Similar time scales of 80 μs, independent of the laser power, were calculated for the time take to reach steady state after the laser source is turned on. These time scales (<100 μs) are significantly shorter than the minute-level time constants that have been

reported in prior claims of CdSNR cooling [1].

In summary, a novel optomechanical eigenfrequency measurement technique was developed for evaluating the temperature of the CdSNRs that have been reported to undergo laser refrigeration. Although the synthesized NRs were highly crystalline and exhibited a high yield of anti-Stokes PL, the eigenfrequencies were observed to decrease with increasing laser power due to heating at low laser powers and a possible laser trapping force at higher laser powers. No evidence of laser refrigeration was observed. A rigorous discussion of a modified Euler-Bernoulli theory of a uniform cantilever with a spring attached to the free end in context of high laser powers has been included to interpret the eigenfrequency data obtained. Theoretical simulations of photothermal heating using transient heat transfer analysis yield a maximum temperature rise and the time to attain steady state for various NR dimensions, laser powers and optical constants. Combined with experimentally measured temperatures, the analytical model also allows the determination of the imaginary refractive index of the CdSNR. This approach is general and may be useful for measuring laser refrigeration in a range of different material systems.

3.2 Thermometry of CdSNR in other geometries

The laser-refrigeration reports by Zhang *et al.*[1] involved experiments with rectangular nanoribbons supported at two ends in a bridge configuration suspended over a SiO_2/Si wafer. To date, analytical models have not been reported for either wedge-shaped cantilevers, or rectangular cantilevers in a bridged configuration. In addition, only heat transfer within a rectangular cantilever was discussed in the previous section. However, since cadmium sulfide nanoribbons (CdSNRs) can be grown to produce either rectangular or wedge shaped nanoribbons. To interpret optomechanical measurements for wedge-shaped samples an analysis of the temperature distribution is also required.[96]

In this section, novel experimental measurements of suspended semiconductor cantilever devices using an approach based on non-contact, continuous-wave Stokes/anti-Stokes Raman spectroscopy are discussed. Furthermore, an exact solution for the time-dependent heat-

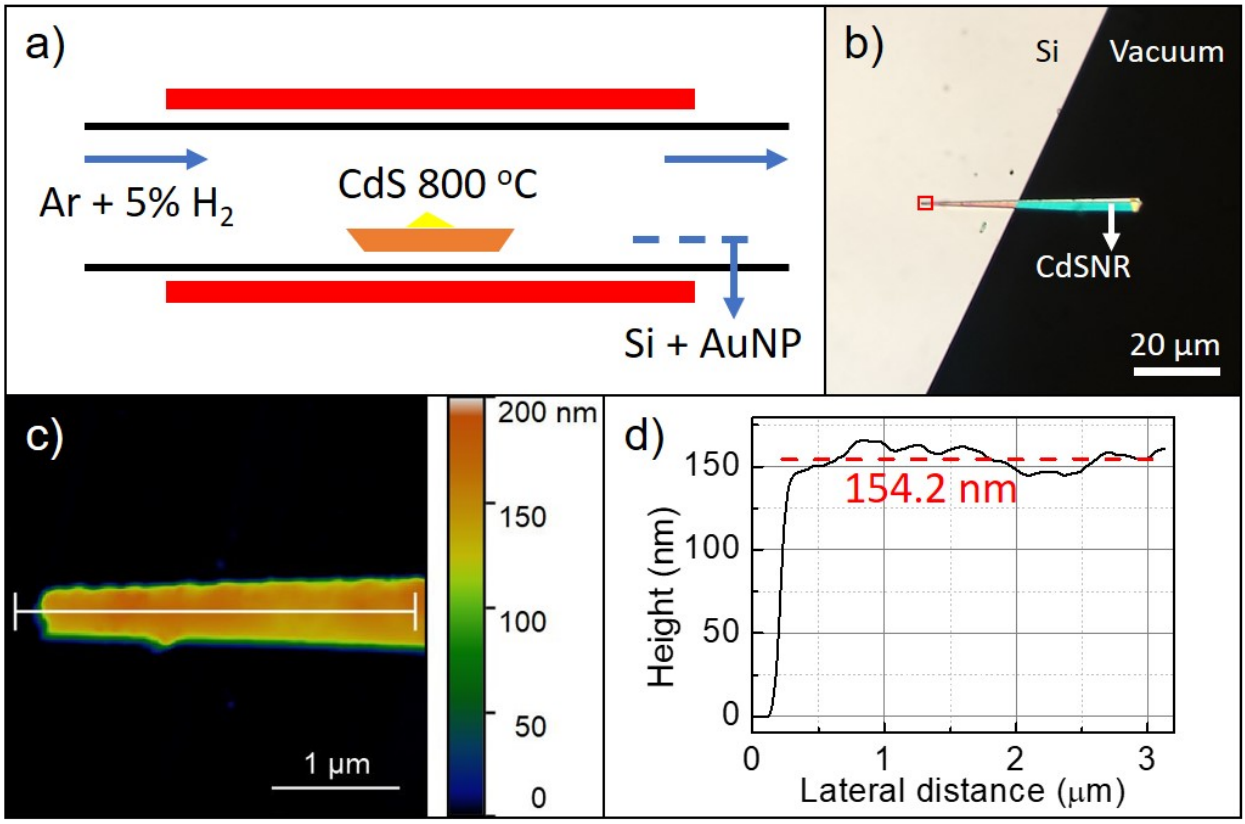

Figure 3.8: a) Schematic of the chemical vapor transport technique to grow CdSNR. The CdS powder (yellow), alumina boat (orange), quartz tube (black), substrate - gold nanocrystals on silicon (blue) and the heating elements (red), are shown. b) A bright field optical image of the CdSNR wedge-type sample with the pointed end supported at the edge of a silicon substrate, and the wider free end is suspended in vacuum. A red square is shown to indicate the area used for AFM measurements c) An AFM height map measured at the sharp end of the supported part of the cantilever on silicon. d) A height plot of the section shown using a white line shown in (c). Average thickness (154.2 nm) is shown using a red dashed line.[96]

transfer equation is derived for both wedged-cantilever and rectangular-bridge geometries for comparison with experimental results. Predicted analytical temperature profiles are observed to agree well with corresponding finite-element calculations, so either methodology can be used for heat transfer analysis. Experimental steady-state temperatures are used to bound the imaginary refractive index of CdSNRs at $\lambda = 532$ nm. These results will improve the interpretation of experimental nanoscale thermometry measurements, including those based on optomechanical laser interferometry or laser spectroscopy. In addition, the results have a direct bearing on the interpretation of the optical refrigeration experiments by Zhang *et al.*[1]

3.2.1 Experimental details for wedge CdSNR measurements

Semicondctor CdSNRs were grown using a previously reported chemical vapor transport (CVT) method [1, 2] shown in Figure 3.8a. The CdS precursor powder (650 mg, 99.995% Sigma Aldrich) was kept in an alumina boat at the center of a quartz tube inside a tube furnace (Lindberg Blue M). A silicon substrate (100) was drop-casted with a dispersion of gold nanocrystals (AuNC, 30 nm) in chloroform and dried in air for 30 min. The prepared substrates were placed in a downstream region, 7-10 cm inside the edge of the tube furnace. Argon + 5% H_2 was used to initially flush the chamber for 30 minutes at 400 SCCM. The flow rate was then reduced to 50 SCCM and the temperature was ramped up to 840 °C and maintained for 2 hours, and the furnace was allowed to cool naturally. Morphological variations based on growth parameters are discussed in further detail in previous literature[2, 87].

Using a nano-manipulator (Märzhäuser-Wetzlär) with a tungsten dissecting probe (World Precision Instruments) having a small tip radius-of-curvature ($\sim$100 nm), a single wedge-shaped CdSNR was removed from the growth substrate and placed at the edge of a clean silicon substrate such that the narrow end was supported by the silicon. The wider, free end was suspended to form a cantilever in vacuum (Figure 3.8b). An atomic force microscope (AFM) was used to obtain a height map of the portion of the CdSNR supported on the

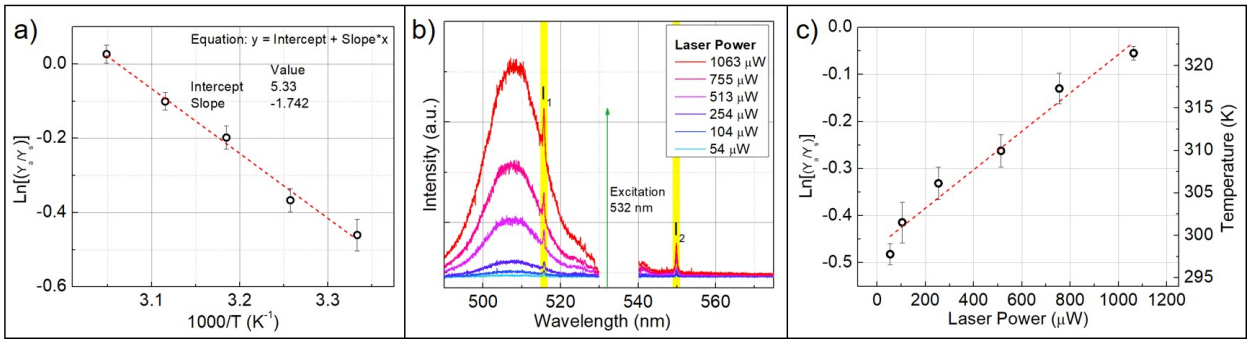

Figure 3.9: a) $\ln(Y_1/Y_2)$ measured for different temperatures using a low 532 nm laser power (54 μW). A least squares linear fit is used as a calibration, shown as a red dashed line. b) Room temperature Raman/PL of the CdSNR wedge obtained at different laser powers of a 532 nm laser. A strong second order LOP anti-Stokes Raman mode with a background of anti-Stokes PL is highlighted and marked with I_1 on the left side of the excitation line. The Stokes second-order LOP is labled I_2. c) Natural log of the ratio Y_1 and Y_2 measured for different 532 nm laser powers at room temperature (298 K). A least squares linear fit is shown using a red dashed line and the calibrated maximum temperature ($1000/T$) is shown in the right y-axis.[96]

silicon wafer (Figure 3.8c). A line scan from the section indicated in Figure 3.8c is shown in Figure 3.8d. The thickness is consistent over the length of the nanoribbon and measures 154 +/− 10 nm.

The Si substrate with the cantilever was placed on a modified cryostat (Janis ST-500) stage using a double sided copper tape, and photoluminescence (PL) spectra were obtained at room temperature by focusing a 532 nm (Coherent Compass 532) single longitudinal mode laser to a diffraction limited spot (radius, $w_0 = 1.25$ μm) with a 50x (Mitutoyo long working distance) objective near the furthest free end of the cantilever. A 532 nm notch filter was used to eliminate the laser line in Raman spectra. A PL peak with center at 509 nm, corresponding to the band gap of CdS was obtained. A weak first order longitudinal optical

phonon (LOP) mode at $I_{1LO} = 304$ cm^{-1} and an enhanced second order LOP mode at $I_{2LO} = 605$ cm^{-1} were observed. The higher ratio (I_{2LO}/I_{1LO}) has previously been attributed to be an indicator of stronger electron-phonon coupling [87, 97]. To isolate the Raman peaks the broad fluorescence background was fit via nonlinear least squares approach using a Gaussian function and subtracted from the Raman spectrum. Due to local heating of the sample using a laser spot, thermal expansion of the hot area is clamped due to the colder region surrounding it. Non-uniform strain due to this will affect the intensity of the Raman peaks, as discussed in previous studies on WS_2.[98] The application of strain on WS_2 showed a 25 % decrease in the intensity of the Stokes A_{1g} peak for a strain of 1 %.[98] Considering the thermal expansion coefficient of $\alpha_{ex} = 6.26\text{X}10^{-6}$ K^{-1} for CdS, the uniaxial strain at 23.4 °C, is given as $\alpha_{ex} * \Delta T = 1.4\text{X}10^{-4}$. At the maximum temperature measured here, using the measured values for intensity counts in WS_2, a relatively minor 0.36 % decrease in the Stokes intensity due to strain was calculated. Assuming the corresponding anti-Stokes intensity increases by 0.36 % at 23.4 °C, the maximum error in the ratio of anti-Stokes to Stokes due to strain effect was estimated as 0.7 %. This additional error based on the measured temperatures at different laser powers was added to the error bars in the power dependent ratio measurements in Figure 3.9c. The anti-Stokes to Stokes intensity ratio was for measuring the temperature. The height of I_{2LO} peaks in the anti-Stokes (I_1) and stokes region (I_2) were obtained through Lorentzian peak fitting, and are labeled Y_1 and Y_2, respectively. The temperature of the cryostat was varied and the spectra were measured using a low laser power (54 μW), and $\ln(Y_1/Y_2)$ was plotted against inverse temperature ($1000/T$). Using a least squares linear fit a slope of -17.4 was obtained (Figure 3.9a). Next, the cryostat temperature was not controlled and spectra were measured using different laser irradiances. The spectra obtained at different laser powers are plotted in Figure 3.9b. The value of $\ln(Y_1/Y_2)$ from the spectra obtained at different laser powers is plotted in Figure 3.9c and the calibration slope was used to obtain the temperature of the sample, shown on the right y-axis. Since the sample was excited and the Raman spectra were measured from the area of the laser spot, the measured temperatures more closely represent the maximum temperature change

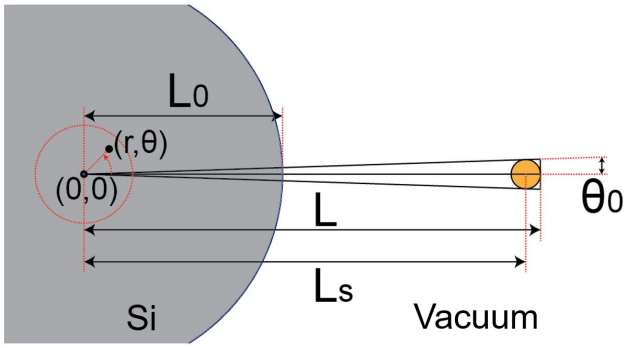

Figure 3.10: Geometry and the cylindrical coordinate system used to obtain the analytical heat transfer solution of the wedge shaped CdSNR. The laser spot (center at L_s, radius w_0) and the silicon boundary ($0<r<L_0$) are shown in orange and grey, respectively.[96]

within the cantilever (ΔT_{max}) relative to optomechanical thermometry[2]. These results indicate the Stokes/anti-Stokes Raman spectroscopy is a sensitive method to investigate the temperature of semiconductor nanoribbons samples during solid-state laser refrigeration experiments.

3.2.2 Heat transfer in wedge CdSNR geometry

Although only heat transfer within a rectangular cantilever was discussed in Pant *et al.*[2], CdSNRs can be grown to produce either rectangular or wedge shaped nanoribbons.[96] To interpret optomechanical measurements for wedge-shaped samples an analysis of the temperature distribution is needed.

For a wedge shaped geometry (Figure 3.10), a solution of the heat-transfer equation is derived below.

The energy equation that applies is expressed in cylindrical coordinates as:

$$\rho\hat{C}\frac{\partial T}{\partial t} = \kappa\left[\frac{1}{r}\frac{\partial}{\partial r}\left(r\frac{\partial T}{\partial r}\right) + \frac{1}{r^2}\frac{\partial^2 T}{\partial \theta^2} + \frac{\partial^2 T}{\partial z^2}\right] + \dot{Q}''', \tag{3.12}$$

for the wedge type geometry, where ρ is the mass density, $\hat{C}$ its heat capacity per unit mass,

κ its thermal conductivity (evaluated at the mean temperature of the nanoribbon), and $\dot{Q}'''$ is the heat generated per unit time per unit volume due to photothermal energy absorption of the pump laser beam. As shown by Pant *et al.*[2], the heat source for a Gaussian beam and a thin nanoribbon is approximated by:

$$\dot{Q}''' = 2k''I_0 \exp\left(-\frac{2r'^2}{w_0^2}\right)\exp(-2k''z), \tag{3.13}$$

in which k'' is related to the complex refractive index $n = n' - in''$ by:

$$k = k' - ik'' = \frac{2\pi}{\lambda}(n' - in''), \tag{3.14}$$

I_0 is the irradiance at the surface (z = 0), r' is the distance from the spot position along the centerline $(0, L_s)$ of the Gaussian beam, and w_0 is the beam waist radius. The maximum value of r' in the case of the wedge and the bridge structures is $L_s \sin(\theta_0)$ and $W/2$, respectively. If the beam waist is greater than either of these values, integration of the source is done in parts, such that the contribution from the beam spot area falling outside the nanoribbon is neglected. The irradiance impinging on the surface is related to the total beam power P_0 by:

$$I_0 = \frac{2P_0(1 - R_\lambda)}{\pi w_0^2}, \tag{3.15}$$

where R_λ is the wavelength dependent reflectance of the beam. The nanoribbons were mounted in a vacuum chamber, so conduction and convection heat transfer from the surfaces suspended in vacuum are absent. For the temperatures involved here radiant energy transfer is also negligible. Consequently, at all surfaces except those attached to the substrate the heat flux is zero, that is $\partial T/\partial s = 0$, where $s = r, \theta, z$. For the wedge-type nanoribbon the temperature is T_b at $r = L_0$. For the solution it is convenient to introduce dimensionless variables defined by:

$$\Theta = \frac{T - T_b}{T_b}, \tau = \frac{\kappa}{\rho\hat{C}}\frac{t}{H^2}, \chi = \frac{r}{L}, \zeta = \frac{z}{H}, \sigma = \frac{H^2\dot{Q}'''}{\kappa T_b}, \tag{3.16}$$

The energy equation transforms to:

$$\frac{\partial\Theta}{\partial\tau} = c^2\left[\frac{1}{\chi}\frac{\partial}{\partial\chi}\left(\chi\frac{\partial\Theta}{\partial\chi}\right) + \frac{1}{\chi^2}\frac{\partial^2\Theta}{\partial\theta^2}\right] + \frac{\partial^2\Theta}{\partial\zeta^2} + \sigma, \tag{3.17}$$

where $c = H/L$. The solution may be written in terms of orthonormal eigenfunctions to give

$$\Theta(\chi,\theta,\zeta,\tau) = \sum_{l=0}^{\infty}\sum_{m=0}^{\infty}\sum_{n=0}^{\infty} B_{lmn}(\tau)X_{lm}(\chi)Q_m(\theta)W_n(\zeta), \tag{3.18}$$

where the eigenfunctions $Q_m(\theta)$, $X_{lm}(\chi)$ and $W_n(\zeta)$ are given by

$$Q_m(\theta) = \frac{1}{\sqrt{2\theta_0}} \text{ for } m = 0, \text{ and } \frac{1}{\sqrt{\theta_0}}\cos\left(\frac{m\pi}{\theta_0}\theta\right) \text{ for } m = 1,2,3,... \tag{3.19}$$

$$X_{lm}(\chi) = \frac{1}{||X_{lm}||}\left[J_{\nu_m}(\mu_{lm}\chi) - \frac{J_{\nu_m}(\mu_{lm}\beta)}{J_{-\nu_m}(\mu_{lm}\beta)}J_{-\nu_m}(\mu_{lm}\chi)\right] \text{ for } l,m = 0,1,2,3,... \tag{3.20}$$

in which $||X_{lm}||$ is defined by

$$||X_{lm}||^2 = \int_{\beta}^{1} \chi'[X_{lm}(\chi')]^2 d\chi' \tag{3.21}$$

$$W_n(\zeta) = 1 \text{ for } n = 0, \text{ and } \sqrt{2}\cos(n\pi\zeta) \text{ for } n = 1,2,3,... \tag{3.22}$$

where $\beta = L_0/L$, and eigenvalues μ_{lm} satisfy the transcendental equation

$$-\mu_{lm}J_{\nu_{m+1}}(\mu_{lm}) + \nu_m J_{\nu_m}(\mu_{lm}) + \frac{J_{\nu_m}(\mu_{lm}\beta)}{J_{-\nu_m}(\mu_{lm}\beta)}[\nu_m J_{-\nu_m}(\mu_{lm}) - \mu_{lm}J_{1-\nu_m}(\mu_{lm})] = 0 \tag{3.23}$$

The coefficients $B_{lmn}(\tau)$ are given by

$$B_{lmn}(\tau) = \frac{2[1-\exp(-\lambda_{lmn}^2\tau)]}{\lambda_{lmn}^2}\int_{\beta}^{1}\int_{0}^{\theta_0}\int_{0}^{1}\sigma(r',\zeta')X_{lm}(\chi')Q_m(\theta')W_n(\zeta')d\chi' d\theta' d\zeta', \tag{3.24}$$

where the primes indicate dummy variables of integration, $\lambda_{lmn}^2 = c^2\mu_{lm}^2 + (n\pi)^2$.

Based on the image of the sample shown in Figure 3.8b and c, the dimensions of the wedge are $L = 49.1$ μm, $\theta_0 = 1.88$ ° and $H = 154$ nm. The wedge rests on the substrate such that $L_0 = 21.4$ μm and is irradiated at $L_s = 47.5$ μm.

The optical constants of CdS at 532 nm, are taken to be $n' = 2.5513$, $n'' = 0.00576$ and $R_\lambda = 0.191$, respectively. The values of material constants ρ and $\hat{C}$ used for the calculations are 4826 kg/m^3 and 470 J/(kg K), respectively.

Table 3.2: Summary of results from temperature calculations using different parameters in the analytical model.The experimentally measured values of ΔT_{ms} are shown in parentheses. The values of material constants ρ and $\hat{C}$ used for the calculations were 4826 kg/m^3 and 470 J/(kg K) respectively, and a laser spot radius $w_0 = 1.25$ μm was used. The temperature dependent values of thermal conductivity[99] adjusted for nanoribbon geometry κ were used.

Wedge geometry						
L, L_0, L_s, H (μm)	θ_0	λ_0 (nm)	Reflectivity (R_λ)	Refractive Index (n)	P_0 (μW)	ΔT_{max} (K)
49.1, 21.4, 47.5, 0.154	1.88	532	0.191	2.5513-i0.00576	1064	90.7
				2.5513-i0.00155	1064	23.4 (23.4)
				2.5513-i0.00155	755	16.4 (19.1)

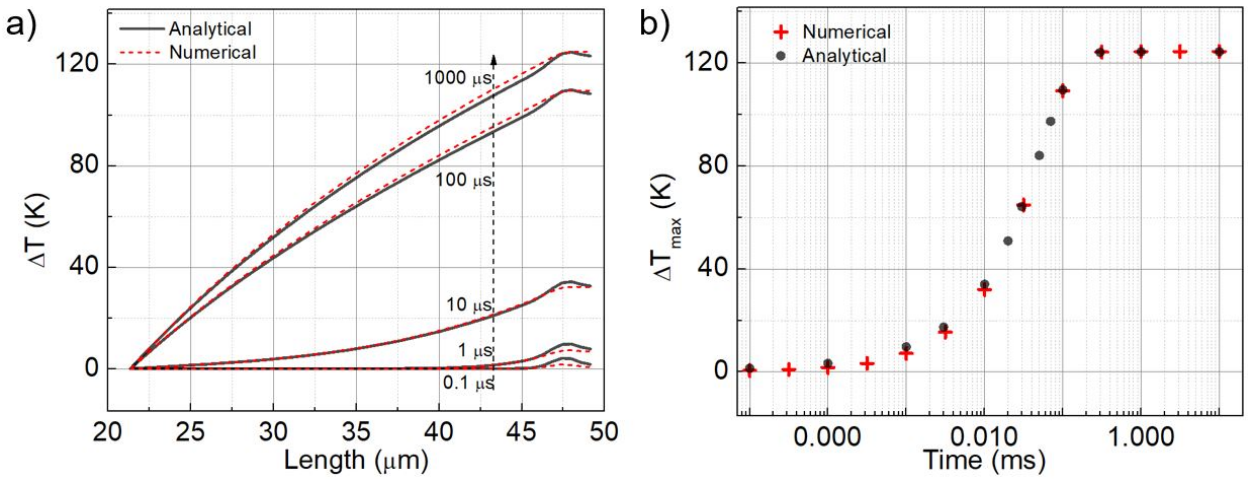

Figure 3.11: a) A temperature distribution along the center line ($\theta = 0$) from L_0 to L of the wedge. b) Temporal evolution of the maximum temperature within the cantilever at a CW laser irradiance of 1450 μW/spot area.[96]

Although the effects of defects within the material or the dimensions of micro/nanoscale devices on the thermal conductivity have been evaluated for certain materials using equilibrium molecular dynamics simulations[100, 101], these are not immediately available in the literature for CdS. It is known that the thermal conductivity within nanostructures depends highly on the dimensionality and can be significantly smaller as compared to the bulk[102]. Thermal conductivity measurements on individual CdS nanowires were measured to be in the range of 4.9-6.2 W/m K[103], however the nanoribbon geometry has only a single constrained dimension and is significantly different compared to a nanowire. Therefore, the temperature dependent values of experimentally measured thermal conductivity (κ) of bulk undoped CdS were used from data extracted and extrapolated from Moore *et al.*[99]. At temperature T (K), $\kappa(T)$ is given as $C_{nano}\exp(C_1 * \log(T) + C_2)$, where C_1 and C_2 fitting parameters were -0.9129 and 8.605, respectively. To account for the size-dependent thermal conductivity within nanoscale semiconductor materials, a C_{nano} multiplier of 0.6 was determined by fitting the model described by Liang *et al.*[104] using parameters for CdS. Considering the relatively smooth surface morphology of the wedge determined by AFM (Figure 3.8c), an arbitrary value of roughness parameter ($p = 0.8$)[104] is assumed. Various factors such as the surface roughness, local crystallinity, doping and phonon mean free path can cause deviations from the value of C_{nano} used here. Accounting for the deviations in C_{nano} caused by all the factors is non-trivial. However, since it has a direct bearing on the imaginary index obtained through the model, an estimated range of values based on the surface roughness of the nanoribbon is projected. For a nanoribbon of the same thickness but a much rougher surface (p = 0.5) a value of $C_{nano} = 0.37$ is obtained, which resulted in a lower bound value of the imaginary index n"=0.00096. Correspondingly, for a nanoribbon with an ideally flat surface ($C_{nano} = 0.75$) the upper bound of the imaginary index was calculated to be n" = 0.00194.

The temperature distribution was derived for room temperature value of κ, in the following iterations κ at average wedge temperature was used until the maximum temperature did not change more than 0.01 K compared to the previous iteration. For calculations of

temperatures with different optical constants or material constants, the values used are reported below. For a wedge with the coordinate system shown in Figure 3.10, the temperature profiles for $P_0 = 1450$ μW along the length from L-L_0 to L at $\theta_0 = 0°$, calculated for different times are shown in Figure 3.11a. Numerical calculations for the same parameters using finite element software (COMSOL) are shown for comparison using a red dotted line. The temporal evolution of the maximum temperature within the cantilever at a CW laser power of 1450 μW are shown in Figure 3.11c, where finite element results are shown in red for comparison. Steady state is reached within 300 μs.

The experimentally measured ΔT_{max} temperatures are compared to those calculated using the wedge heat transfer model in Figure 3.12. A summary of the parameters used for calculations is listed in Table 1. The temperatures calculated agree with the experimentally measured temperatures if a imaginary refractive index $n'' = 0.00155$ is used, instead of the correlated value of 0.00576[95] at 532 nm. There is a considerable uncertainty in the value of n'' in the wavelength range of 500 to 560 nm. Reported values range from 0.1 to 1x10^{-7} [95]. The estimated value of 0.00155 is lower than the value of 0.00576 based on a correlation by Treharne *et al.*[95]. The difference in the estimated n'' at 532 nm in these measurements compared to that in literature could arise from local variations in the material's imaginary refractive index, or morphology dependent resonances (MDRs)[91] which could contribute up to 1-3.7 times higher absorption per unit area within CdSNRs with thickness varying by tens of nanometers above or below ∼100 nm[2].

3.2.3 Heat transfer in bridge CdSNR geometry

For the bridge-type geometry (Figure 3.13a), with conduction boundaries on the both ends of the rectangular geometry, the energy equation is given by:

$$\rho\hat{C}\frac{\partial T}{\partial t} = \kappa\left[\frac{\partial^2 T}{\partial x^2} + \frac{\partial^2 T}{\partial y^2} + \frac{\partial^2 T}{\partial z^2}\right] + \dot{Q}'''. \tag{3.25}$$

The temperature at $y = 0$ and L is the base temperature T_b and at all the surfaces except those attached to the substrate the heat flux is zero. It is convenient to introduce

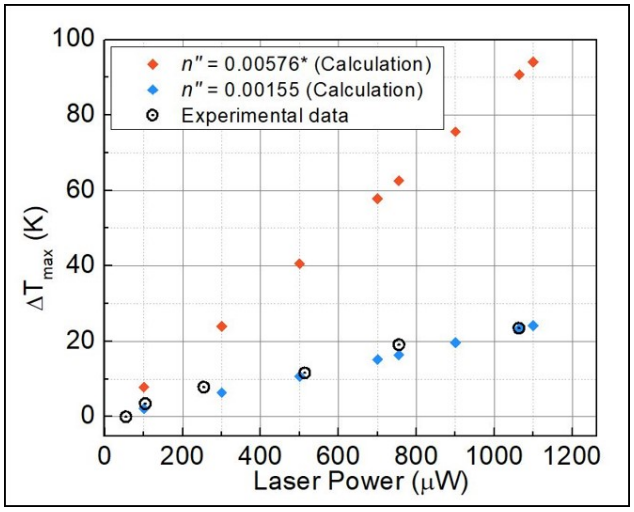

Figure 3.12: Experimentally measured temperatures of CdSNR wedge compared with the heat transfer analysis of the maximum temperature change when a imaginary index of $n'' = 0.00155$ (blue) is used in comparison with a correlated value of 0.00576 (red).[96]

dimensionless variables defined by:

$$\Theta = \frac{T - T_b}{T_b}, \tau = \frac{\kappa}{\rho \hat{C}} \frac{t}{H^2}, \xi = \frac{x}{W/2}, \tag{3.26}$$
$$\eta = \frac{y}{L/2}, \zeta = \frac{z}{H}, \sigma = \frac{H^2 \dot{Q}'''}{\kappa T_b}.$$

In this case, the energy equation becomes

$$\frac{\partial \Theta}{\partial \tau} = a^2 \frac{\partial^2 \Theta}{\partial \xi^2} + b^2 \frac{\partial^2 \Theta}{\partial \eta^2} + \frac{\partial^2 \Theta}{\partial \zeta^2} + \sigma, \tag{3.27}$$

where $a = 2H/W$ and $b = 2H/L$.

The solution becomes

$$\Theta(\xi, \eta, \zeta, \tau) = \sum_{l=0}^{\infty} \sum_{m=0}^{\infty} \sum_{n=0}^{\infty} A_{lmn}(\tau) U_l(\xi) V_m(\eta) W_n(\zeta), \tag{3.28}$$

where the eigenfunctions are given by

$$U_l(\xi) = \cos(l\pi\xi) \qquad \text{for } l = 0, 1, 2, 3, ... \tag{3.29}$$

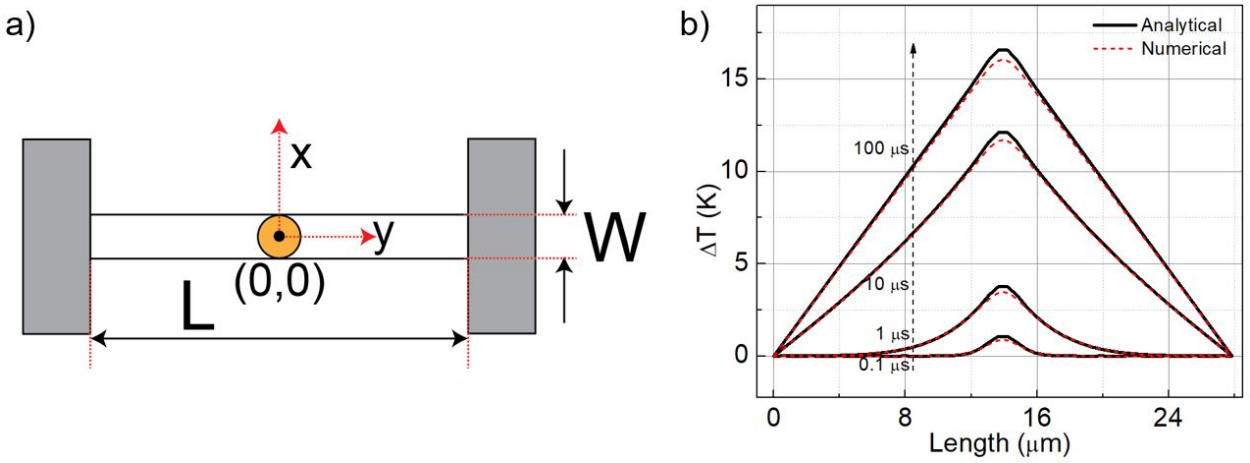

Figure 3.13: a) Geometry and the Cartesian coordinate system used to obtain the analytical heat transfer solution of the rectangular shaped CdSNR bridge supported at two ends. The laser spot (center at origin, radius w_0) and the silicon boundary are shown in orange and grey, respectively. (b) A temperature distribution along the center line (x = 0) from -L/2 to L/2 of the bridge.[96]

$$V_m(\eta) = \cos(\beta_m \eta) \qquad \text{for } m = 0, 1, 2, 3, ... \tag{3.30}$$

$$W_n(\zeta) = 1 \text{ for } n = 0, \text{ and } \sqrt{2}\cos(n\pi\zeta) \text{ for } n = 1, 2, 3, ... \tag{3.31}$$

where eigenvalues β_m satisfy Biot number (Bi) dependent equation

$$\beta_m \sin(\beta_m) = Bi \cos(\beta_m) \tag{3.32}$$

The coefficients $A_{lmn}(\tau)$ are given by

$$\begin{aligned} A_{lmn}(\tau) = \quad & \frac{[1 - \exp(-\gamma_{lmn}^2 \tau)]}{\gamma_{lmn}^2} \int_0^1 \int_0^1 \int_0^1 \\ & \sigma(\xi', \eta', \zeta') \frac{U_l(\xi')}{||U_l||^2} \frac{V_m(\eta')}{||V_m||^2} \frac{W_n(\zeta')}{||W_n||^2} d\xi' d\eta' d\zeta', \end{aligned} \tag{3.33}$$

where the prime indicates dummy variables of integration, $\gamma_{lmn}^2 = a^2\beta_l^2 + b^2(m\pi)^2 + (n\pi)^2$ and the norms are given by

$$||U_l||^2 = \frac{1}{2}\left(1 + \frac{\sin^2(\beta_m)}{Bi}\right) \tag{3.34}$$

$$||V_m||^2 = \begin{cases} 1 & \text{for } m = 0 \\ \frac{1}{2} & \text{for } m = 1, 2, 3, ... \end{cases} \tag{3.35}$$

The steady state solution is obtained by taking the limit $\tau \to \infty$ in Eq. (3.33).

For the bridge geometry (Figure 3.13a), with a rectangular NR clamped at both ends, the same optical and material constants were used for the temperature calculations shown in Figure 3.13b. Dimensions similar to that of the wedge shape with suspended length of L=27.7 μm, W=3.2 μm and H=154 nm were used. The maximum temperature reached at steady state is considerably lower at ΔT_{max}=15 K than that calculated for a wedge (ΔT_{max}=75 K), for the same laser power (1064 μW), primarily due to the availability of two conductive paths for the heat transfer to the sink. A summary of the parameters used for calculations is listed in Table 3.3. For the same reason, time scales (Figure 3.14a) required to reach steady state were also found to be relatively smaller (100 μs).

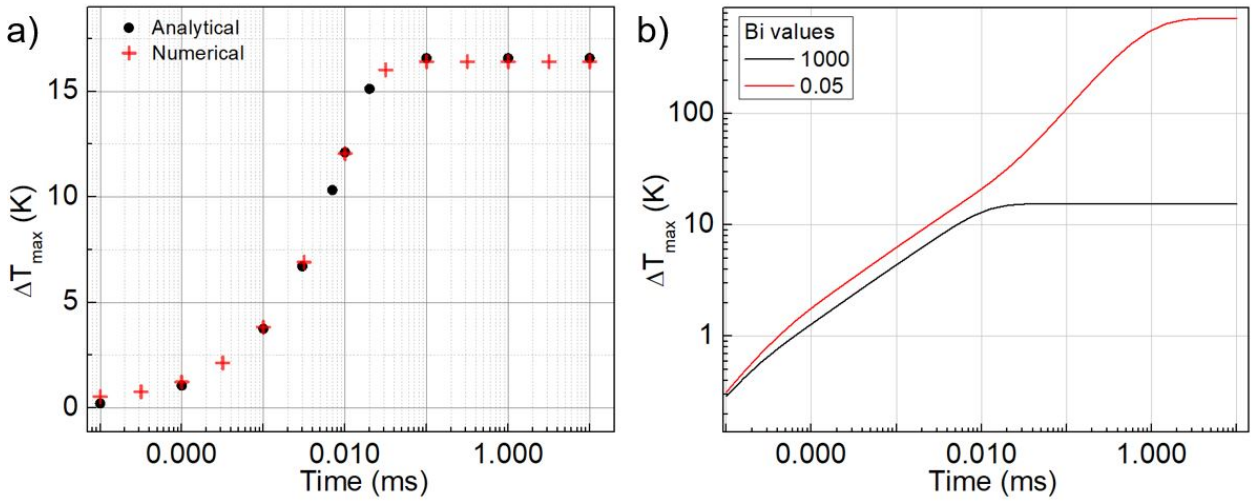

Figure 3.14: a) An analytical and numerical calculation of time-dependent maximum change in temperature within the bridge type geometry and maximum limit case of Biot number is considered. (b) The effect of time scales of maximum change in temperature within the bridge type nanoribbon for various Biot numbers.[96]

Table 3.3: Summary of results from temperature calculations using different parameters in the analytical model. The values of material constants ρ and $\hat{C}$ used for the calculations were 4826 kg/m^3 and 470 J/(kg K) respectively, and a laser spot radius $w_0 = 1.25$ μm was used. The temperature dependent values of thermal conductivity[99] adjusted for nanoribbon geometry κ were used.

Bridge geometry						
L, W, H (μm)	λ_0 (nm)	Reflectivity (R_λ)	Refractive Index (n)	P_0 (μW)	Biot number	ΔT_{max} (K)
27.7, 3.2, 0.154	532	0.191	2.5513-i0.00576 2.5513-i0.00576	1064	1000 0.05	16.6 720

The generality of the model allows for calculation of steady state times in the case of poor thermal contact between the cantilever and the sink. The effects of poor thermal contact in the case of the bridge structure are evaluated, as shown in Figure 3.13b. Using various Biot numbers to mimic poor conductances at the contact, a smaller the Biot number (lower thermal conductance) is shown to increase the time scales (Figure 3.13b). For the lowest thermal conductance measured (8.5 MW/(m^2 K)[105]), an equivalent Biot number of 0.7, the calculated steady state timescale is estimated to be 2 times longer compared to that of the ideal case. A hypothetical case of ultra-low thermal conductance, in the case of physically unlikely Biot number of 0.1 show steady state time scales as long as 2 ms required to reach steady state.

In summary, the temperature change within a suspended nanoribbon irradiated with a focused Gaussian laser spot was experimentally measured using Stokes/anti-Stokes Raman spectroscopy. Measured temperatures were compared with the analysis of heat transfer for a wedge-shaped cantilever. The model enables calculation of the temperature distribution within the nanostructure due to local heating with the laser, which is essential for accurate eigenfrequency thermometry based on the cantilever's temperature-dependent Young's modulus. A timescale of 300 μs is required to reach steady state temperatures in wedge geometry and show much faster times of 33 μs in the case of bridge geometry. The heat transfer model for the bridge geometry allows the inclusion of interfacial resistance at the boundaries. Using the highest value of interfacial resistance measured between solid surfaces, a steady state time scale of 3 ms is calculated. This is four orders of magnitude faster than that reported by Zhang *et al.*[1]

Chapter 4

LASER REFRIGERATION EXPERIMENTS

Photothermal heating represents a major constraint that limits the performance of many nanoscale optoelectronic and optomechanical devices including nanolasers, quantum optomechanical resonators, and integrated photonic circuits. This section demonstrates the direct laser refrigeration of a semiconductor optomechanical resonator >20K below room temperature based on the emission of upconverted, anti-Stokes photoluminescence of trivalent ytterbium ions doped within a yttrium-lithium-fluoride ($LiYF_4$) host crystal. Optically-refrigerating the lattice of a dielectric resonator has the potential to impact several fields including scanning probe microscopy, the sensing of weak forces, the measurement of atomic masses, and the development of radiation-balanced solid-state lasers. In addition, optically refrigerated resonators may be used in the future as a promising starting point to perform motional cooling for exploration of quantum effects at mesoscopic length scales, temperature control within integrated photonic devices, and solid-state laser refrigeration of quantum materials.

4.1 Laser refrigeration of CdSNR using Yb:$LiYF_4$

4.1.1 Introduction

Photothermal heating is a perennial challenge in the development of advanced optical devices at nanometer length scales given that a material's optical index of refraction, bandgap, and Young's modulus all vary with temperature. For instance, reducing the mechanical motion of an optomechanical resonator to its quantum ground state requires that the temperature (T) must be much less than $h\nu/k_B$, where ν is the mode frequency, h and k_B are Planck and Boltzmann constants, respectively[37]. Critically, incident laser irradiances

must be kept low enough to avoid photothermal heating of the resonator above cryogenic temperatures[38, 39, 40, 37, 41]. An approach for the photothermal cooling of nanoscale optoelectronic devices through the emission of anti-Stokes photoluminescence is shown. In particular, a micrometer-scale grain of 10% Yb^{3+}-doped $YLiF_4$ (Yb:$LiYF_4$) located at the end of a semiconductor optomechanical resonator (CdS) was used to cool the resonator >20K below room temperature following excitation with a continuous wave laser source with wavelength $\lambda_0 = 1020$ nm.

Recently, laser refrigeration of a macroscopic Czochralski grown Yb:$LiYF_4$ crystal was used to cool a semiconductor FTIR detector (HgCdTe) to 135 K[21]. In contrast, in this work the temperature of a nanoscale semiconductor optomechanical resonator (CdSNR) is reduced using laser refrigeration of a hydrothermally synthesized Yb:$LiYF_4$ microcrystal attached to it. The cooling of a load using a microscopic cooler enables local cooling. In addition, it also offers a route towards rapidly achieving a thermal steady (μs to ms scale) temperature state within nanoscale devices.

The device is suspended in vacuum from a silicon wafer to reduce the potential for photothermal heating of the adjacent silicon substrate. Van der Waals bonding is used to attach a low-cost, hydrothermal ceramic Yb:$LiYF_4$ microcrystal[19] to the end of the resonator cavity. Rare-earth (Yb^{3+}) point-defects within the $LiYF_4$ emit anti-Stokes photoluminescence which cools both the $LiYF_4$ microcrystal, and also the underlying semiconductor optomechanical resonator. The $LiYF_4$ serves both as a local thermometer (discussed in more detail below) and also as a heat sink which extracts thermal energy from the cantilever, increasing its Young's modulus, and thereby blue-shifting the cantilever's optomechanical eigenfrequency. The transmitted laser causes minimal heating of the cantilever supporting the $LiYF_4$ crystal due to its small thickness (150 nm) and extremely low absorption coefficient of CdS at 1020 nm[95]. The temperature of the source and the cantilever system are measured using two independent non-contact temperature measurement methods - differential luminescence thermometry[59] and optomechanical thermometry[2], respectively, which agree well with each other. The results below suggest several potential applications

for using solid-state laser refrigeration to rapidly cool a wide range of materials used in scanning probe microscopy[106, 107, 108], cavity optomechanics[38, 41, 109, 110], integrated photonics[111, 112, 113], the sensing of small masses and weak forces[114, 115, 116, 117], quantum information science[118], and radiation balanced lasers[119].

4.1.2 Optomechanical thermometry of CdSNR with Yb:$LiYF_4$

A CdSNR was placed at the end of a clean silicon substrate, and a hydrothermally grown 10% Yb:$LiYF_4$ crystal was placed at the free end of the CdSNR cantilever.[79] CdS was chosen because of its wide band gap and low-cost, though in principle any material with low near-infrared (NIR) absorption can be used. A bright-field optical image of a representative sample is shown in Figure 4.1b. The silicon substrate was loaded inside a cryostat chamber such that the free end of the cantilever was suspended over the axial hole in the cryostat, and the system was pumped to $\sim 10^{-4}$ Torr. As shown in Figure 4.1a, a 1020 nm laser was focused onto the Yb:$LiYF_4$ crystal at the end of the cantilever. The time-dependent intensity of the forward-scattered 1020 nm laser was measured by focusing it onto an avalanche photodiode (APD). To measure the cantilever's eigenfrequencies the voltage vs. time signal was Fourier-transformed to obtain its thermomechanical noise spectrum[120, 121]. A representative power spectrum measured on the sample at 300 K using a laser irradiance of 0.04 MW/cm^2 is shown in Figure 4.1c. A sharp peak, fitted using a standard Lorentzian with a peak position at 3648.9 Hz, was attributed to the first natural resonant frequency mode ("diving board mode") of the nanoribbon cantilever with the fluoride crystal. As shown in Figure 4.1a, the backscattered photoluminescence was collected from the rear end of the objective, transmitted through a beamsplitter, was filtered using a 1000 nm short-pass filter and focused into the spectrometer slit. Photoluminescence (PL) spectra were recorded at different grating positions, with appropriate collection times to avoid saturating the detector, and they were stitched together. Ten spectra were collected using 0.04 MW/cm^2 of laser irradiance for 0.1 s and averaged. The intense Yb^{3+} transitions[122, 75] in the range of 800 to 1000 nm, with major peaks at 960 (E_6-E_1), 972 (E_5-E_1) and 993 (E_5-E_3) nm were observed (Figure 4.1d). A longer

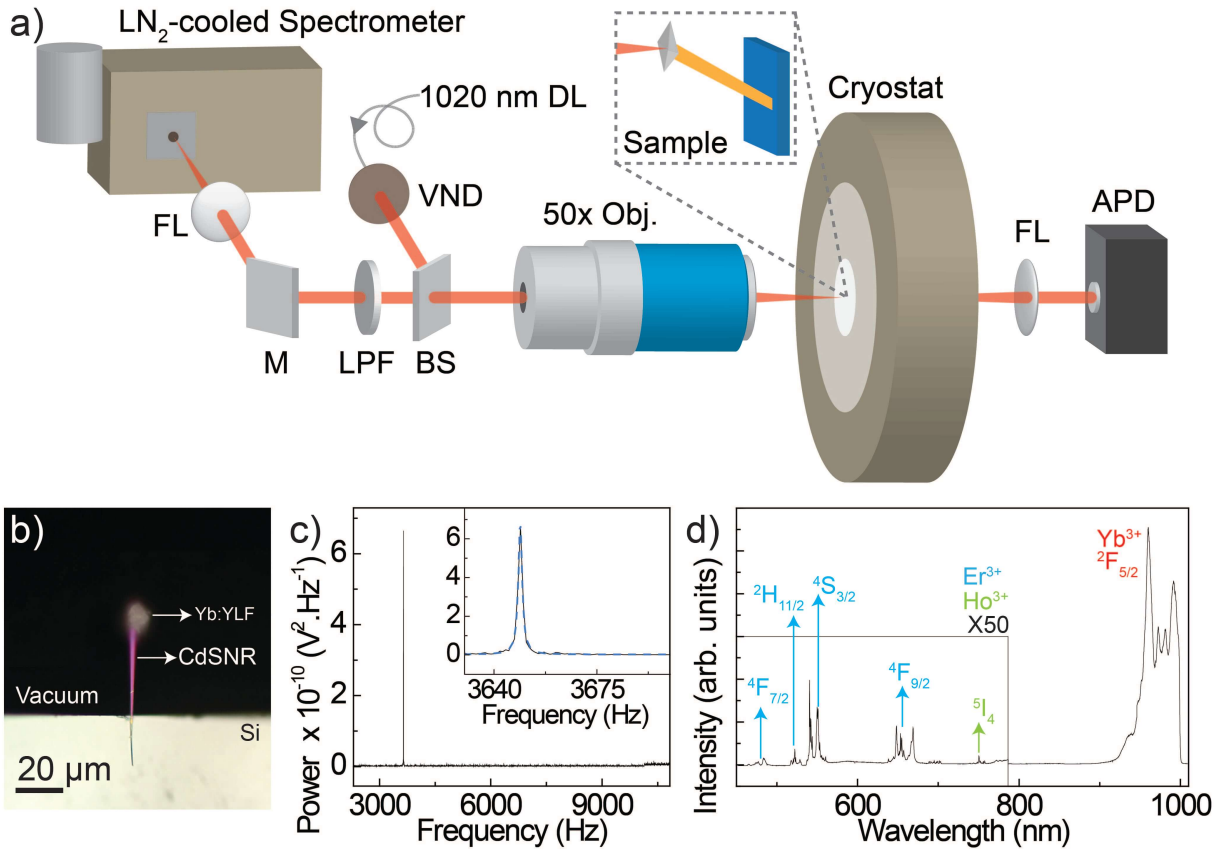

Figure 4.1: a) The schematic of the eigenfrequency and upconverted fluorescence measurement setup. FL, M, SPF, DL, BS, VND and APD stand for focusing lens, mirror, 1000 nm short pass filter, diode laser, beam splitter, variable neutral density filter and avalanche photodiode, respectively. b) A bright field optical image of the CdSNR cantilever supported using a silicon substrate with a Yb^{3+}:$LiYF_4$ crystal placed at the free end. c) A peak in the thermomechanical noise spectrum originating from the fundamental eigenfrequency of the CdSNR with Yb^{3+}:$LiYF_4$ sample obtained at the 0.04 MW/cm^2 at 300 K. d) A stitched, up-converted fluorescence spectrum obtained at room temperature using a 1020 nm excitation source (0.04 MW/cm^2) focused on the suspended Yb^{3+}:$LiYF_4$ crystal. A 1000 nm short pass filter was used to cut off the laser line.[79]

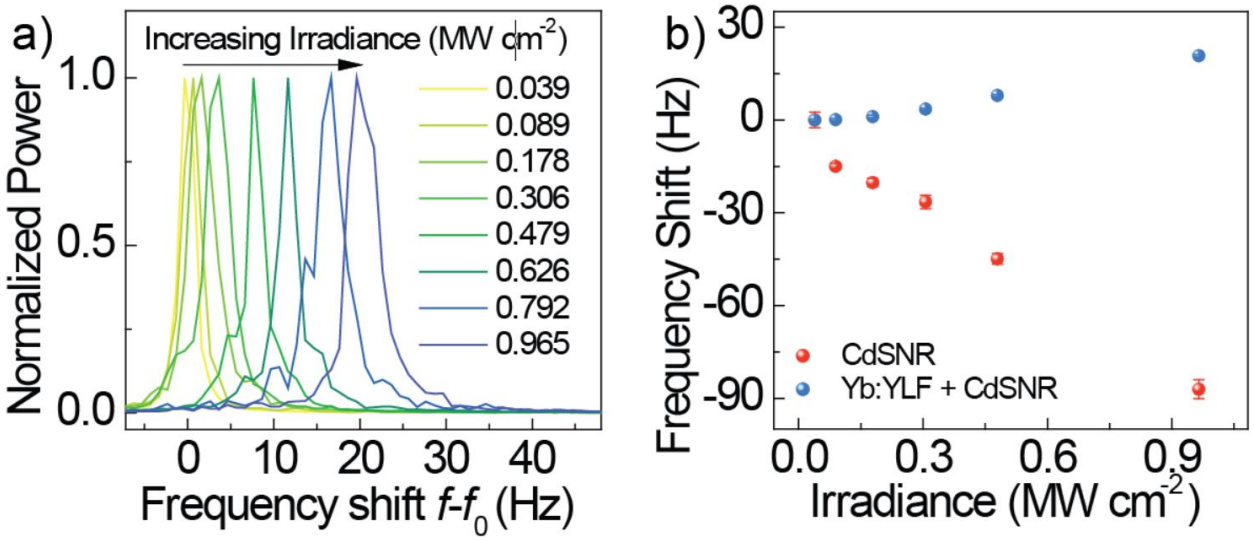

Figure 4.2: a) Normalized power spectra for a representative laser refrigeration measurement at each laser irradiance with an ambient reference temperature of 295 K (f_0 = 3632.2 Hz). b) The frequency shift ($f - f_0$) with laser power at 295 K for both a plain CdSNR (red) and CdSNR with Yb:$LiYF_4$ (blue). Each data point was obtained by taking the mean of peak position obtained from Lorentzian fits of 6 thermomechanical noise spectra and error bars represent one standard deviation. Note that for small standard deviations, the error bars overlap with the data point. f_0 is 3632.2 Hz and 17384.4 Hz, respectively.[79]

acquisition time (50x) was used to collect the weaker luminescence signal from the other rare earth (RE) impurities that were not explicitly added during synthesis. The up-converted green and red emission peaks at 520, 550 and 650 nm are attributed to the transitions from $^2H_{11/2}$, $^4S_{3/2}$ and $^4F_{9/2}$, respectively, of trivalent erbium ions (Er^{3+})[123, 124]. Other minor transitions are labeled.

Power spectra normalized using the maximum value at different laser irradiances obtained from the sample are plotted in Figure 4.2a. When fit to a standard Lorentzian, the peak values show a blue-shift in the eigenfrequency of the FCNR system as the laser power is

increased. The fitted peak values of these power spectra are shown in Figure 4.2b. As the laser irradiance was increased, the Yb:$LiYF_4$ source reached lower temperatures, thereby extracting more heat from the CdSNR cantilever and causing a blue-shift in the frequency due to an increased Young's modulus of the CdS at lower temperatures. Using a 980 nm laser with an irradiance of 0.5 MW/cm^2 resulted in the irreversible photothermal melting of the cantilever device. When the Yb:$LiYF_4$ crystal was removed from the CdSNR cantilever in Figure 4.2b, the fundamental frequency measured at 0.04 MW/cm^2 increased to a higher value of 17384.3 Hz due to the removal of mass from the system ($\sim$1.3x10^{-9}g). As a control experiment, the eigenfrequency of the CdSNR cantilever itself was measured after the removal of the Yb:$LiYF_4$ crystal. The eigenfrequency of the cantilever without the crystal was then measured as a function of the laser power and is shown in Figure 4.2b. The eigenfrequency red-shifted as the laser irradiance was increased, suggesting greater heating of the cantilever at higher irradiances due to the decreasing Young's modulus at higher temperatures[2]. The temperature of the FCNR device was calibrated by increasing the temperature of the cryostat from 160 to 300 K (Figure 4.3a), which showed a linear red-shift in the eigenfrequency of the cantilever. The slope of -0.389 Hz/K obtained using this calibration was used to measure the temperature change of the cantilever system during laser refrigeration experiments. The maximum blue-shift in the eigenfrequency as a function of laser irradiance of the was +20.6 Hz at an irradiance of 0.97 MW/cm^2, compared to the lowest irradiance of 0.04 MW/cm^2. Based on the isothermal temperature calibration, ignoring temperature gradients and other optomechanical effects on the cantilever due to increased irradiance, this blue-shift of +20.6 Hz corresponds to a temperature change of 53 K below room temperature (assuming a negligible change in temperature at a laser irradiance of 0.04 MW/cm^2).

To evaluate the effect on the eigenfrequency at other wavelengths, a 980 nm and a 1020 nm laser spots were co-focused. The thermomechanical noise spectra of a representative device were measured using both wavelengths Figure 4.3b shows that with increasing 1020 nm laser irradiance the eigenfrequency blue-shifts, indicating that the device cools. In contrast, using a 980nm laser leads to a heating-induced red-shift of the cantilever's eigenfrequency with

increasing irradiance. To limit damage to the device the 980 nm irradiance was maintained below 0.2 MW/cm^2.

To obtain the absolute change in temperature it is important to view the system through a modified Euler-Bernoulli beam theory and include the effects of the laser trapping forces[6] on the Yb:$LiYF_4$ crystal, which acts as a spring at the end of the cantilever. With increased irradiances, due to the increased force constant of the spring, the eigenfrequency of the cantilever increases. The analytical model to evaluate this effect was discussed previously (Section 2.5.2).

To experimentally probe the effects of the laser trapping forces, the power-dependent eigenfrequency measurements were performed at a constant cryostat temperature of 77 K. At temperatures as low as 77 K, the cooling efficiency of the Yb:$LiYF_4$ crystal decreases due to diminishing resonant absorption and red-shifting of the mean fluorescence wavelength[59]. Due to negligible cooling with increased irradiance, and with the equilibrium temperature being maintained by the crysostat, it is assumed that any blue-shift in the eigenfrequency of the system was solely due to the greater laser trapping force at higher irradiance. Therefore, the excessive blue-shift at room temperature (6 +/- 2.2 Hz) can be attributed to the change in Young's modulus due to cooling of the CdSNR cantilever. According to this calibration, the cantilever's temperature is reduced 15.4 +/- 5.6 K below room temperature. Since cantilever eigenfrequencies are calibrated at isothermal conditions, the temperatures measured via cantilever eigenfrequencies during laser-refrigeration do not directly measure the coldest point within the cantilever, but rather a lower bound of the absolute minimum achievable temperature decrease[2]. This is a consequence of temperature gradients within the cantilever that lead to gradients of the cantilever's Young's modulus. Based on finite element eigenfrequency modeling of the cantilever with a spatially varying Young's modulus, the coldest point in the cantilever can be calculated. Below a steady-state heat-transfer model of the laser-cooled cantilever system is presented to quantify how thermal gradients within CdSNR cantilevers affect eigenfrequency measurements during laser refrigeration experiments.

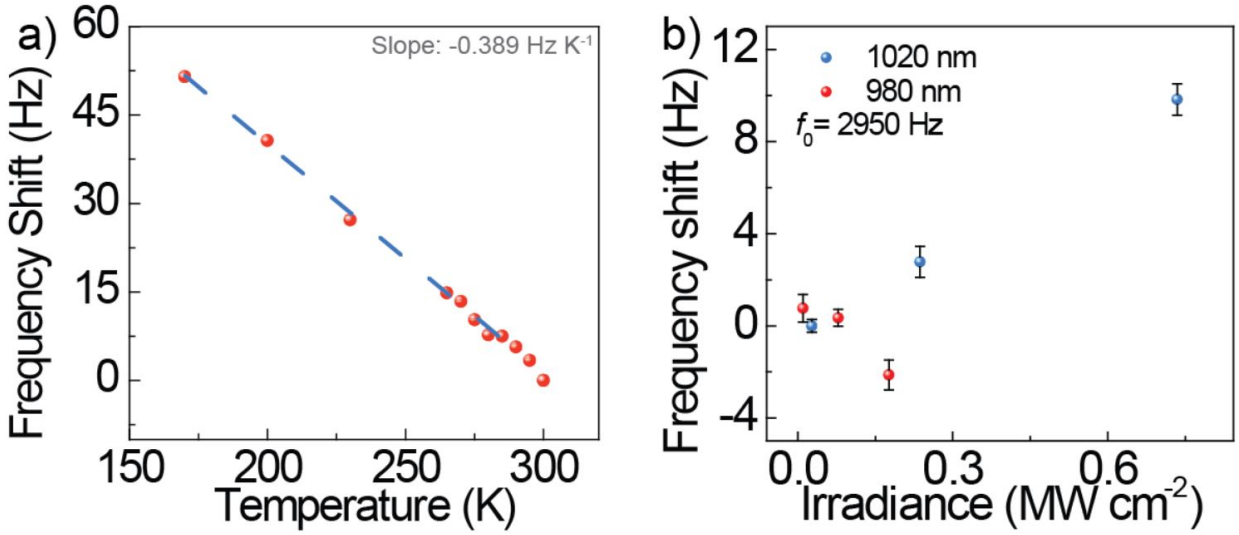

Figure 4.3: a) Temperature calibration of the CdSNR with Yb:$LiYF_4$ obtained by measuring the frequency shift $f - f_0$ ($f_0 = 3653.6$ Hz) as a function of the cryostat temperature. The data points take into account the uncertainties in measurement by averaging the frequency value obtained from six thermomechanical noise spectra recorded at the given temperature. The error bars represent one standard deviation. b) Eigenfrequency measurements using co-focused 980 and 1020 nm lasers. The data points take into account the uncertainties in measurement by averaging the frequency value obtained from six thermomechanical noise spectra recorded at the given laser power. The error bars represent one standard deviation.[79]

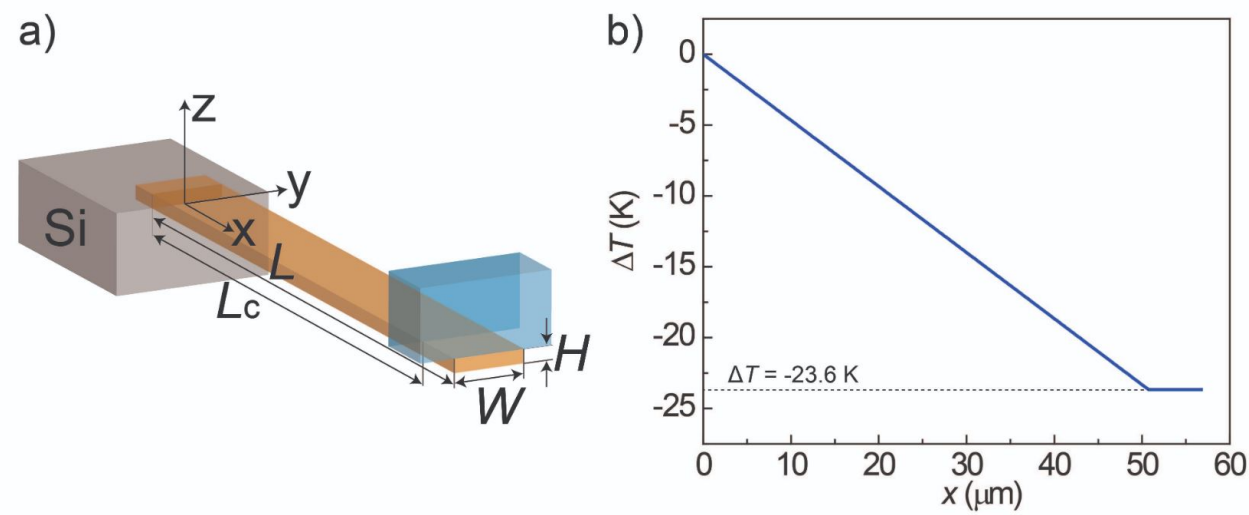

Figure 4.4: a) The geometry of FCNR system used for analytical and finite element heat transfer modeling. b) The steady state temperature along the length of the CdSNR calculated using analytical one dimensional solution obtained assuming all of the cooling power produced by the $LiYF_4$ crystal flows through the CdSNR cross section at L_c.[79]

4.1.3 Heat transfer in laser-cooled cantilever system

A cantilever of length 'L', width 'W', and thickness 'H' is modeled with a $LiYF_4$ crystal placed at the free end (see Figure 4.4a). The $LiYF_4$ crystal is approximated as a cuboid with sides of $H_{YLF} = 6$, $L_{YLF} = 7.5$ and $W_{YLF} = 6$ μm, such that the volume and aspect ratio were similar to the tetragonal bi-pyramidal $LiYF_4$ crystal used experimentally.

At steady state the temperature distribution in the nanoribbon satisfies the energy equation given by:

$$\frac{\partial^2 T}{\partial x^2} + \frac{\partial^2 T}{\partial y^2} + \frac{\partial^2 T}{\partial z^2} = 0. \tag{4.1}$$

Heat transfer to the surroundings by conduction and convection is absent due to the vacuum surrounding the cantilever. Radiant (blackbody) energy transfer to or from the surroundings is negligible due to the relatively low temperatures of the cantilever and its small surface

area. Therefore, the heat flow within the cantilever is one-dimensional and equation (4.1) reduces to:

$$\frac{d^2T}{dx^2} = 0, \tag{4.2}$$

which has the general solution:

$$T(x) = C_1 x + C_2. \tag{4.3}$$

Assuming negligible interfacial resistance between the cantilever and the underlying silicon substrate, the temperature at the silicon/CdS interface (x = 0) is the cryostat temperature T_0. Consequently, the boundary condition at the base of the nanoribbon is $T(0) = T_0$. If all of the heat generated in the $LiYF_4$ crystal is transferred to or from the CdSNR across the interface at $x = L_c$, the heat flux at the interface is given by:

$$\kappa \frac{dT}{dx}(L_c) = \frac{\dot{Q}_c}{HW}, \tag{4.4}$$

in which $\dot{Q}_c$ is the rate of heat removal from the $LiYF_4$ crystal, and κ is the thermal conductivity of CdS.

Applying the boundary conditions, the temperature distribution in the CdSNR becomes:

$$T(x) = \frac{\dot{Q}_c}{\kappa HW} x + T_0. \tag{4.5}$$

It is assumed that the relatively large thermal conductivity of the $LiYF_4$ crystal (∼6 W/(m K)) will lead to a nearly uniform temperature (Figure 4.4b) in the crystal given by:

$$T(L_c) = \frac{\dot{Q}_c}{\kappa HW} L_c + T_0. \tag{4.6}$$

The rate of laser energy absorbed per unit volume $Q''' = Q_{abs}/V$ is given by:

$$Q''' = \frac{4\pi n' n''}{\lambda_0 Z_0} (\mathbf{E} \cdot \mathbf{E}^*). \tag{4.7}$$

Here $n = n' - in''$ is the complex refractive index of the medium, λ_0 is the wavelength in vacuum, Z_0 is the free space impedance ($Z_0 = 376.73\ \Omega$), and $\mathbf{E}^*$ is the complex conjugate of the electric field vector within the $LiYF_4$ crystal. Upconverted, anti-Stokes luminescence

follows laser absorption, cooling the crystal. The absorption of the incident laser by the underlying CdS cantilever is neglected due to its small thickness (154 nm) and low absorption coefficient at 1020 nm (6.7x10^{-13} cm^{-1}) relative to what has been reported[59] for $LiYF_4$ ($\sim$1cm^{-1}).

4.1.4 Discussion for thermometry of CdSNR with Yb:LiYF$_4$

Given that eigenfrequency measurements can only provide a lower bound of the cantilever's temperature, a more direct approach must be used to measure the temperature at the end of the cantilever. Differential luminescence thermometry (DLT)[13, 75] was used to measure the temperature of the $LiYF_4$ at the end of the cantilever based on using a Boltzmann distribution to analyze emission from different crystal-field (Stark) levels. A temperature drop of 23.6 K below room temperature ($\Delta T_{\max}$) was measured at an irradiance (I_0) of 0.97 MW/cm^2 corresponding to an incident power $P_0 = 40.1$ mW and spot radius $w_0 = 1.15$ μm. Using the measured value of $T(L_c) - T_0 = 23.6$ K, $H = 150$ nm, $W = 2.5$ μm, $L_c = 53$ μm, and $\kappa = 20$ W/(m K)[99], A cooling power of $\dot{Q}_c = 3.34$ x 10^{-6} W was calculated. The resultant temperature gradient along the length of the device is shown in Figure 4.4b. Based on the temperature gradient, by modeling a spatially varying Young's modulus, the coldest point in the cantilever from eigenfrequency measurements was calculated to be between 26 and 58 K below room temperature. This agrees well with the coldest temperature measured using DLT.

An absorption coefficient and cooling efficiency of 0.61 cm^{-1} and 1.5%, respectively, have been reported previously for a bulk $LiYF_4$ crystal doped with 10% Yb-ions.[59] Based on this absorption coefficient, considering full illumination of the Yb:$LiYF_4$ crystal, a maximum cooling power of 2.2 μW would be generated when irradiated by a 40.1 mW pump laser. This cooling power is smaller than the experimental cooling power reported above. The discrepancy can be explained by two factors related to the symmetric morphology of the $LiYF_4$ microcrystals. First, the size of the $LiYF_4$ microcrystals is within the Mie-regime for light scattering and internal optical fields may be enhanced considerably due to morphology

dependent cavity resonances. Two-dimensional finite-difference time-domain calculations show that the internal optical power within a $LiYF_4$ microcrystal can be twice as large as the incident power due to internal cavity resonances. Consequently, first-order linear absorption calculations may underestimate the cooling power due to an underestimation of the internal optical power of the pumping laser. Second, a combination of light-scattering and multiple internal reflections of the pump beam within the microcrystal can excite a larger volume of the crystal compared to the incident spot size. In addition the fluorescence is emitted throughout $LiYF_4$ microcrystal, including far from where the excitation laser is focused.

This experiment demonstrate an approach to decrease the temperature of a nanoscale semiconductor optomechanical resonator by >20K below room temperature using solid-state laser refrigeration of a Yb:$LiYF_4$ crystal. Thermometry and calibration of the fabricated device are performed using two independent methods - optomechanical eigenfrequencies and differential luminescence thermometry, respectively - which compare well with each other. A modified Euler-Bernoulli model is used to account for the laser trapping forces, and the measured temperatures are validated using heat transfer theory. A maximum drop in temperature of 23.6 K below room temperature was measured near the tip of the cantilever. Among other applications in scanning probe microscopy and exploration of quantum effects at mesoscopic length scales[117], optical refrigeration of a mechanical resonator could have significant implications for weak force and precision mass sensing applications[115, 116], in the development of composite materials for radiation balanced lasers[119], and local temperature control in integrated photonic devices[112, 113]. In the future, solid-state laser refrigeration may also assist in the cooling of optomechanical devices by enabling the use of higher laser irradiances in the absence of detrimental laser heating.

4.2 Laser Refrigeration of NV^- Quantum Sensors

The negatively-charged nitrogen vacancy (NV^-) centre in diamond is a remarkable optical quantum sensor for a range of applications including, nanoscale thermometry[125],

magnetometry[126, 127, 128], single photon generation[129, 130], quantum computing[131], and communication[132]. However, to date the performance of these techniques using NV^- centres has been limited by the thermally-induced spectral wandering of NV^- centre photoluminescence due to detrimental photothermal heating[7]. This section demonstrates that solid-state laser refrigeration can be used to enable rapid (ms) optical temperature control of nitrogen vacancy doped nanodiamond (NV^-:ND) quantum sensors in both atmospheric and *in vacuo* conditions. Nanodiamonds are attached to a 10% Yb:$LiYF_4$ ceramic microcrystal by van der Waals bonding. The fluoride crystal was cooled through the efficient emission of upconverted infrared photons[133] excited by a focused 1020 nm laser beam. Heat transfer to the ceramic microcrystal cooled the adjacent NV^-:NDs by 27 K at $\sim 10^{-3}$ Torr.

The temperature of the NV^-:NDs was measured using DWF thermometry[78]. Stabilization of thermally-induced spectral wandering of the NV^- ZPL is achieved by modulating the 1020 nm laser irradiance. The demonstrated cooling of NV^-:NDs using an optically cooled microcrystal opens up new possibilities for rapid feedback-controlled cooling of a wide range of nanoscale quantum materials.

4.2.1 Background: NV^- center doped nanodiamond quantum sensors

Nanodiamonds with negatively charged nitrogen vacancy centres (NV^-:NDs) are widely known for their remarkable optical properties and have generated interest as key materials for quantum information science,[131] nanoscale thermometry,[125] magnetometry,[126] and many other applications.[134] NV^- spin systems have long (ms) coherence times at room temperature and their spin-readouts are readily accessible by visible lasers and microwave (MW) radiation. Optical levitation of nanodiamonds offers the additional advantage of extreme isolation, which is conducive to achieving ultra-high quality factor mechanical oscillation and longer spin coherence times for potential applications such as detectors in advanced cosmological observatories that study areas such as dark matter,[135] quantum gravity,[136] and gravitational waves.[137]

Diamonds doped with nitrogen are prone to photothermal heating due to the background

absorption of point defects including substitutional nitrogen (P_1) centres and both neutral (NV^0) and negatively charged (NV^-) nitrogen vacancy centres. This photothermal heating can lead to unintended particle ejection from an optical trap, or cause the graphitization and even burning of the trapped particle.[7] The absence of conductive and convective pathways for removing excess heat from the optically-trapped particle *in vacuo* magnifies the effect of photothermal heating. Recent theoretical models[57] suggest that the direct radiative cooling of microdiamonds trapped in vacuum may be possible, but direct laser refrigeration of diamond remains to be demonstrated experimentally.

The recent cooling of fluoride-based ceramics to sub-cryogenic temperatures suggests that the indirect laser refrigeration of diamonds may be possible.[13] Both microcrystals and nanocrystals of Yb:$LiYF_4$ and Yb:$NaYF_4$ have previously been shown to cool in vacuum[75] and also in physiological media.[23, 19] However, to date solid-state laser refrigeration has not been demonstrated to modulate the temperature of nanoscale quantum sensors.

In this section the laser refrigeration of NV^-:NDs is demonstrated. The refrigeration is based on anti-Stokes luminescence from an underlying micrometer-scale Yb:$LiYF_4$ crystal. The use of micrometer-scale ceramics enables steady-state temperatures to be reached rapidly within microseconds to milliseconds[138] which is comparable to the electron spin coherence time of the NV^- centre.[139] The internal temperature of the NV^-:NDs are made using non-contact optical thermometry. First, a Debye-Waller factor (DWF) thermometry approach[78] is used which is based on the the temperature-dependent ratio of the emission from the NV^- centre's zero-phonon to that of phonon overtones. Second, the internal temperature of the Yb:$LiYF_4$ microcrystal lattice was measured using two-band differential luminescence thermometry (TB-DLT) based on emission from Yb ions.[65].

4.2.2 NV^-:ND DWF thermometry setup

Thermal isolation of the laser cooled crystal was crucial for more efficient cooling for a given laser irradiance. Therefore, the cooling microcrystals with NV^-:NDs were placed at the end of a single-crystalline CdS nanoribbon cantilever[79] that was suspended off of the edge of

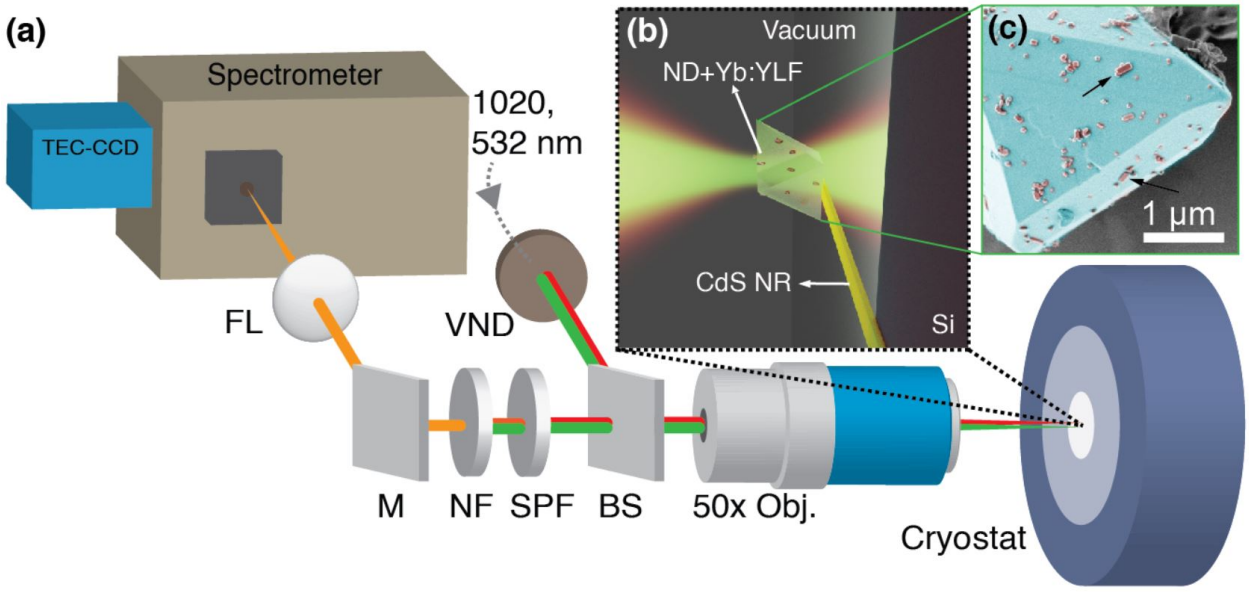

Figure 4.5: a) A schematic of the photoluminescence measurement setup. TEC-CCD, FL, VND, M, NF, SPF, and BS refer to thermoelectrically-cooled charge coupled device, focusing lens, variable neutral density filter, silver mirror, 532 nm notch filter, 1000 nm short pass filter, and beam splitter, respectively. b) An illustration of the cadmium sulfide nanoribbon (CdS NR) cantilever device suspended in vacuum using a silicon substrate. A 10% ytterbium doped lithium yttrium fluoride (Yb:$LiYF_4$) crystal with nanodiamonds (NV^-:NDs) dropcast on it is attached to the free end of the cantilever device. Subsequent inset on the right shows the c) SEM of a representative Yb:$LiYF_4$ crystal with NV^-:NDs dropcast on it (colored for illustrative purposes). Representative NV^-:NDs on different facets of the the Yb:$LiYF_4$ crystal are indicated using black arrows. [79]

a silicon substrate. The small contact and cross-sectional area of the cantilever minimizes the heat conduction losses from the microcrystal. The CdS nanoribbon is ∼110 nm thick in the direction of light propagation, and is optically transparent at 1020 nm (and relatively transparent at 532 nm) which minimizes any additional heating due to its low absorption coefficient ($\alpha_{1020\ \mathrm{nm}} = 6.7 \times 10^{-13}$ cm^{-1}, $\alpha_{532\ \mathrm{nm}}$=1362 cm^{-1}). An illustration of the device used for quantum temperature sensing is shown in Figure 4.5b. A representative scanning electron micrograph of the Yb:$LiYF_4$ crystal coated with NV^-:NDs is shown in Figure 4.5c. Nanodiamonds were coated onto the Yb:$LiYF_4$ crystal with a number density of ∼3.7±1 μm^{-2}.

In the NV^- generation process, nitrogen initially enters the diamond lattice as a substitutional impurity during ion implantation (usually ≤200 ppm). Subsequent radiation damage induced by a variety of sources such as a beam of high-energy neutrons, electrons, or ions is used to create vacancies.[140] Annealing of the irradiated diamond at T≥850 °C causes thermal diffusion of the vacancies. This results in the appearance of the desirable NV^- complexes.[140] However, not all the nitrogen atoms are converted to the NV^- centres, inducing a variety of undesirable defects.

In addition to the photothermal heat generated from the broad phonon overtones of NV^- centres, other surface or lattice defects within NV^-:NDs may contribute to photothermal heating. Both electron paramagnetic resonance (EPR) and a superresolution infrared absorption spectroscopy technique called infrared photothermal heterodyne imaging (IR-PHI)[141] have confirmed the presence of various defects (P_1, B-centres, A-centres and B2-aggregates) within ensemble and individual NV^-:ND particles, respsectively.

4.2.3 DWF thermometry of NV^-:NDs

Debye-Waller factor thermometry[78] was used to measure the temperature of irradiated NV^-:ND quantum sensors by calibrating the ratio of the ZPL emission relative to the adjacent phonon side bands ($I_{\mathrm{ZPL}}/I_{\mathrm{overtone}}$). In Figure 4.6a, the black line shows the composite spectrum from the sample when both the 532 and 1020 nm beams were incident. Since the

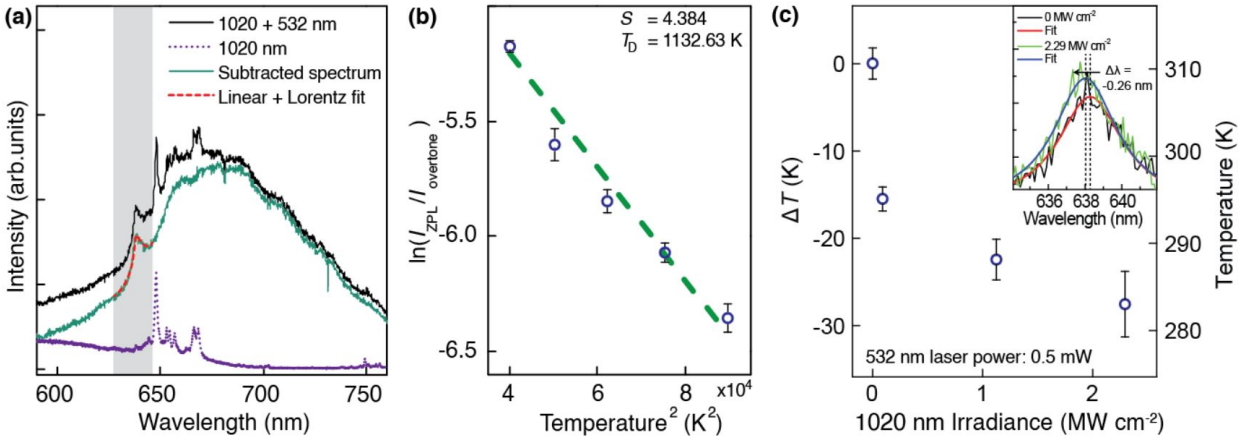

Figure 4.6: a) The composite PL spectrum, when both 1020 and 532 nm lasers are on, is shown in black. The contribution from the upconverted $^4F_{9/2}$ emission from Er^{3+} impurity ions is shown using a dotted purple line. The subtracted spectrum and the fitting function are shown using a green and dashed red line, respectively. b) The natural log of the DWF is plotted versus the temperature squared. A linear fit (dashed green line) to the data is used to extract T_D and S. c) The corresponding calibrated temperatures obtained from the measured value of $\ln(I_{ZPL}/I_{overtone})$ from the processed spectra are plotted for various laser irradiances of 1020 nm while the 532 nm laser is kept consistently at an irradiance of 0.073 MW/cm^2. The inset shows a close up of the background subtracted PL spectra in the ZPL region (∼638 nm), and the Lorentzian component of the ZPL fit as the 1020 nm irradiance is increased from 0 and 2.29 MW/cm^2 are shown in red and blue, respectively. [79]

NV^- emission spectrum was crucial in obtaining the temperature of the NV^-:NDs using the DWF technique, the background $^4F_{9/2}$ emission from the Er^{3+} impurities (dotted purple line) overlapping with the emission of the NV^- centre was subtracted from the composite spectrum (black line) at the respective intensity of 1020 nm laser used to obtain the emission profile from the NV^- centres (green line). The ZPL was fit using a function consisting of a linear background and a Lorentzian around the ZPL (dashed red line) and the integrated intensity of the ZPL peak (I_{ZPL}), centred at 638 nm, was obtained from the amplitude of the Lorentzian component. The emission intensity from the phonon side bands (I_{overtone}) was obtained by subtracting the ZPL area from the integrated area of the spectrum. As the temperature of the cryostat was changed from 200-300 K, the DWF was calculated and plotted against temperature squared (Figure 4.6b). The data points were fit to the calibration function (dashed green line) discussed in Plakhotnik *et al.*[78] to obtain the Debye temperature (T_{D}=1132.6 K) and the electron-phonon coupling parameter (S=4.38). These values were used as a calibration for subsequent measurements. Figure 4.6c shows the calibrated temperature of the NV^-:NDs at various 1020 nm laser irradiances, where a continuous wave (CW) 532 nm laser at an irradiance of 0.073 MW/cm^2 was used as a probe beam to excite the NV^- centres. As the 1020 nm laser irradiance was increased, an immediate drop in temperature and subsequent saturation trend was observed. A maximum temperature change of 27.7($\pm$3.8) K measured at 2.12 MW/cm^2 of 1020 nm laser irradiance using DWF thermometry agrees well with the temperature change of the Yb:$LiYF_4$ microcrystal.

Therefore, the cooling power generated by Yb:$LiYF_4$ microcrystal in vacuum allowed net cooling of the attached NV^-:NDs by 27.7($\pm$3.8) K. The photothermal heating of NV^-:NDs from the 532 nm probe laser was measured to be 25.6 mK/μW at zero 1020 nm irradiance. Heating from the probe laser can be reduced by using low probe laser irradiances on the order of 10 KW/cm^2 along with sensitive detectors. The inset of Figure 4.6c shows a close up of the background-subtracted PL spectra in the ZPL region ($\sim$638 nm). The ZPL fit at two 1020 nm irradiances is shown. As the irradiance is increased, the cooling induced blue-shift of the ZPL peak is observed from the respective fits. Tuning the 1020 nm irradiance

allows for the stabilization of thermally-induced spectral wandering of the NV^- centre's ZPL. A feedback loop can therefore be established so that the red-shifts in ZPL due to heating can be sensed optically and counteracted by increasing (cooling) pump laser intensities. The NV^-:ND temperature may be adjusted 3-6 orders of magnitude faster than a large cryostat's temperature considering the micro-millisecond timescales taken by the microcrystal to reach steady state temperatures.

4.2.4 Two-band differential luminescence thermometry of Yb:$LiYF_4$

The internal temperature of the Yb:$LiYF_4$ microcrystal lattice was measured using two-band differential luminescence thermometry (TB-DLT) based on emission from Yb ions.[65] This approach involves integrating the near-infrared emission of crystal field transitions of Yb^{3+} ions and using a temperature-dependent Boltzmann distribution (see section 2.6). Photoluminesnce spectra were collected and normalized with respect to the 960 nm peak ($E_6 \rightarrow E_1$), obtained from a 10% Yb:$LiYF_4$ microcrystal, excited at 0.09 (black) and 1.05 MW/cm^2 (red) irradiances, are shown in Figure 4.7a. The area under the dominant peaks, representing the transitions $E_6 \rightarrow E_1$ (960 nm) and $E_5 \rightarrow E_3$ (993 nm) from Yb^{3+} ions in the $LiYF_4$ host, have been labeled as I_1 and I_2, respectively. The temperature of the Yb:$LiYF_4$ crystal can be determined using a ratiometric analysis of the fluorescence spectra.

The natural log of the ratio (I_1/I_2) as a function of laser irradiance is plotted in Figure 4.7b. As the laser irradiance increases, the ratio decreases, indicating cooling of the Yb:$LiYF_4$ crystal. The lowest irradiance (0.09 MW/cm^2) was used for calibration. The temperature change of the Yb:$LiYF_4$ crystal was measured to be 15 K below room temperature, at an irradiance of 1.05 MW/cm^2. At the same laser irradiance, the temperature change measured in the NV^-:NDs with DWF was 19K.

In summary, the indirect laser refrigeration of nanodiamond quantum sensors via van der Waals attachment to ceramic laser-cooling microcrystals is demonstrated in vacuum. We use complementary non-contact thermometry methods (DWF and TB-DLT) to demonstrate solid-state laser refrigeration as a rapid (ms) approach for controlling the temperature of

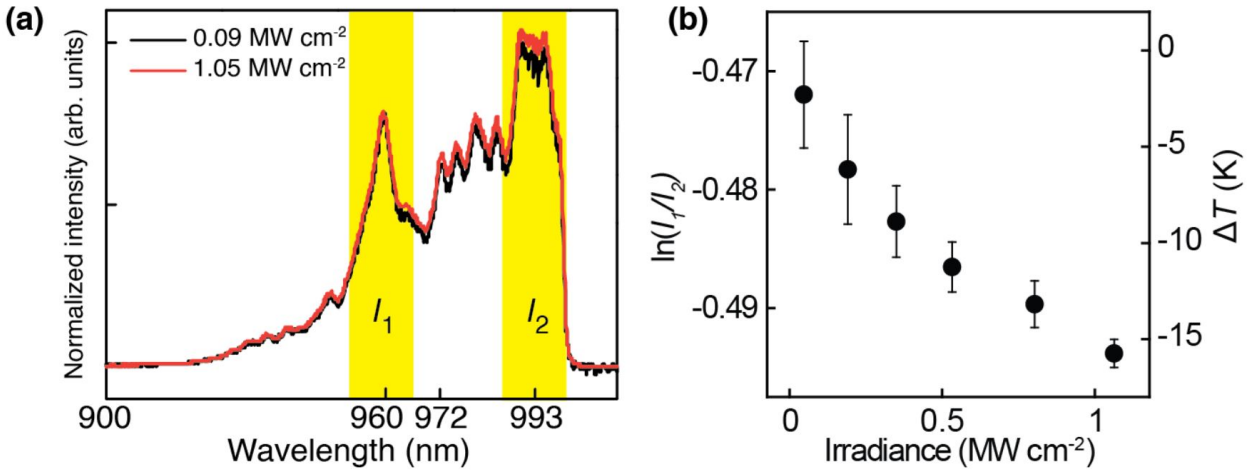

Figure 4.7: a) Intense anti-Stokes emission from the Yb^{3+} ions in the Yb:$LiYF_4$ crystal, using the resonant 1020 nm excitation with irradiances 0.09 (black) and 1.05 MW/cm^2 (red). Major peaks at 960 (E_6-E_1), 972 (E_5-E_1) and 993 (E_5-E_3) nm were observed. The ratio of integrated emission from the $E_6 \rightarrow E_1$ (960 nm) and $E_5 \rightarrow E_3$ (993 nm), represented by I_1 and I_2 respectively, are shown using yellow highlights. The ratio of I_1 and I_2 was used to obtain the temperature within the Yb:$LiYF_4$ crystal. b) The natural log of ratio of I_1 and I_2 is plotted against the 1020 nm laser irradiance. The decrease in the ratio with increasing irradiance indicates lower temperatures at higher irradiances. The right y-axis shows the calibrated temperatures. [79]

nanoscale quantum materials near room temperature. A 27 K drop in the internal temperature of the NV^-:NDs was measured in vacuum. This allows for the stabilization of thermal spectral wandering of the NV^- ZPL by tuning the 1020 nm irradiance. Laser refrigeration of NV^-:NDs will enable rapid feedback temperature control of quantum materials for a wide range of quantum sensing and communication applications. These results may also enable new experimental possibilities in quantum information science including single-beam laser trapping[110, 71, 142], precision sensing of temperature,[125] magnetic fields,[126] dark matter,[135] and quantum gravity.[137]

4.3 $LiYF_4$ on nitride nanobeam optical cavity

A silicon nitride nanobeam cavity device was obtained from Chen *et al.*[143] The nanobeam cavity has the same design parameter as in the original authors' previous work[144]. A Yb:$LiYF_4$ microcrystal was carefully transfered on to the device using a nanomanipulator. The dark field and the bright field image of the device after the Yb:$LiYF_4$ crystal was placed on it is shown in the Figure 4.8a and its inset, respectively.

The device is characterized under a confocal microscopy setup. A dark field optical image of a silicon nitride nanobeam cavity with a Yb:$LiYF_4$ microcrystal placed on it is shown in Figure 4.8. A 1020 nm cooling laser was focused on the Yb:$LiYF_4$ microcrystal and is highlighted using a red circle. The nanobeam cavity is probed through a pair of grating couplers as the input and output ports. The input grating coupler incident with a focused supercontinuum source is highlighted using a green circle. The yellow circle shows the transmitted light from the other end of the nanobeam cavity as the output port. The light from within the yellow circle was isolated using an iris and sent to the spectrometer. A sharp cavity resonance is observed near 747 nm. The spectra measured at 20 and 50 °C are shown in Figure 4.8b. The spectra of the cavity resonance peak measured at various temperatures was fit using a Lorentz function. The fits are shown in Figure 4.8c using a blue and green dashed line for 20 and 50° C spectra, respectively. The inset shows the shift in average fitted peak position of five different spectra at each temperature with respect to the

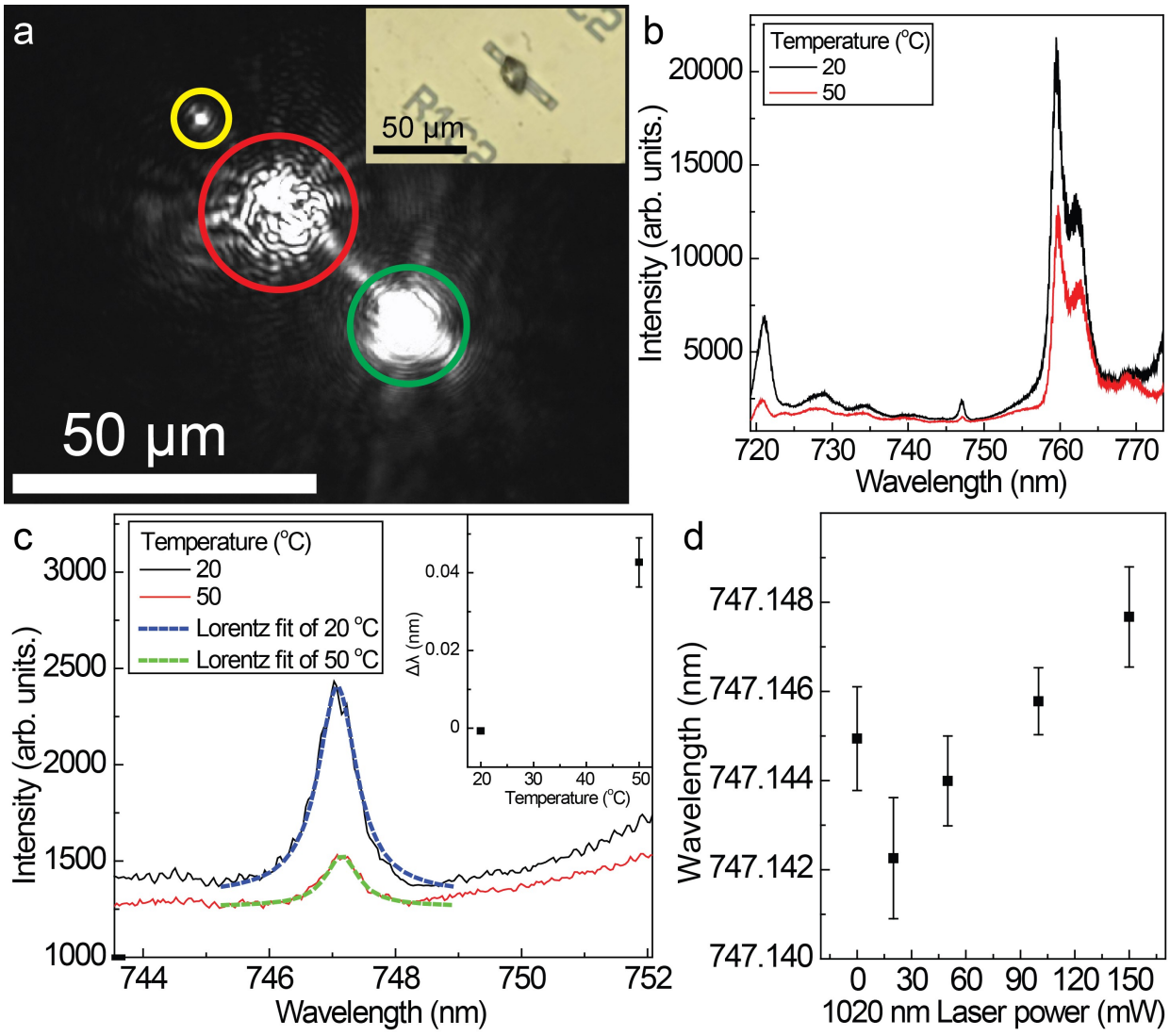

Figure 4.8: a) Dark field optical image of a silicon nitride nanobeam cavity with a Yb:$LiYF_4$ microcrystal placed on it. Red circle: 1020 nm laser spot; Green circle: input port; Yellow circle: output port. Inset is the bright field image of the device b) The spectra at two different device temperatures (20 and 50 °C) are shown. A sharp cavity resonance is observed near 747 nm; c) A closeup of the resonant peak and the Lorentz fits to the spectra. Inset shows the calibration of the peak position at different temperatures. d) Average peak position for five spectra at each laser power. [in preparation]

20 °C measurement. The error bars represent one standard deviation. The cavity resonance red-shifts at higher temperatures, enabling the measurement of the internal temperature of the silicon nitride material. A heating calibration slope of 1.45E-3 nm/K was obtained. The resonance spectra were measured at room temperature using various 1020 nm laser powers and were fit using the Lorentz function. The average peak position for five spectra at each laser power are plotted in Figure 4.8d. The error bars represent one standard deviation. The internal temperature of Si_3N_4 can be measured via its thermooptic coefficient (dn/dt) by observing the transmitted eigenmodes of a waveguide-coupled Si_3N_44 nanobeam cavity to which a Yb:$LiYF_4$ crystal is attached. The internal temperature of the Si_3N_4 cavity is shown to decrease by 1.84 °C with increasing 1020 nm excitation, despite the presence of a thick underlying silicon substrate which is susceptible to heating from the transmitted 1020 nm laser beam. As the laser power is increased, the heating of the underlying substrate due to the transmitted 1020 nm laser power starts dominating.

Chapter 5

EXPLORATION OF COLOR CENTERS

5.1 Intrinsic laser refrigeration of semiconductors

In the past chapter, a significant advancement in the area of laser refrigeration was demonstrated by refrigerating a CdSNR semiconductor load using a Yb:$LiYF_4$ microcrystal. However, intrinsic cooling of the semiconductor itself was not achieved. As stated in the introductory sections, internal cooling of a semiconductor is still an attractive scientific goal to achieve. This is because, when compared to 10%Yb:$LiYF_4$ (MAT ~89 K)[13], semiconductors have theoretically been proposed to have a MAT in the 10 K regime[52]. In semiconductors, the Fermi-Dirac statistics ensure that the carrier population in the valence band is not depleted at low temperatures[145].

5.1.1 Laser refrigeration of semiconductors through color centers

In semiconductors, the requirements for external quantum efficiency are stringent. In addition, semiconductor physical properties remain major obstacles in achieving intrinsic laser refrigeration: high optical fluorescence absorption and a high real part of refractive index, which decreases the photon-escape efficiency. Given the success of laser-cooling lanthanide point defects within fluoride ceramic host crystals, it is worth considering cooling point defects in semiconductors. Recently there has been a theoretical interest in solid-state laser refrigeration of point defects in diamond [57].

Kern *et al.* [57] have shown that diamond microcrystals containing SiV and NV could achieve a maximum temperature drop of 21K and 60K, respectively, below room temperature. Their models suggest that it may be possible to achieve net cooling in diamonds using SiV and NV doping. It is shown that microcrystals of diamonds with a diameter <200 μm

doped with either SiV^- and NV^- may be optically refrigerated by isolating individual crystals through optical traps or electrodynamic traps in vacuum. This may be extended in other media as previously demonstrated cooling in physiological medium using optical RE-doped materials[19, 23, 75].

Kern *et al.* [57] have shown that a maximum temperature drop (ΔT) from room temperature of 21 and 60 K may be possible in microdiamond crystals doped with SiV^- and NV^- centers. For this to be possible, defects will require near-unit quantum efficiencies. In their parametric study with varying quantum efficiency, the cooling of these materials drastically reduced with a relatively small decrease in the EQE (from 1 to 0.97). Therefore identifying and suppressing the sources of nonradiative relaxation will be essential in order to realize net cooling.

Anti-Stokes fluorescence has been observed experimentally in several color centers in diamond including the H3 center[146], the SiV^- center[147], and also NV^- and GeV^- centers[148] using standard optical spectroscopy techniques. These recent results motivate future experimental efforts towards observing solid-state laser refrigeration in diamond through color centers.

When color center such as NV^- fluoresce, a large number of phonons are produced. This causes an undesirable loss in the cooling efficiency and also prevents the use of lower wavelength light sources. As a solution, Kern *et al.* [57] suggest exploration of ZPL emission enhancement with respect to the over all emisison from the phonon side bands. A few methods such as Purcell effect[149] or resonant methods using Mie scattering, Fabry-Perot enhancement and whispering gallery modes (WGM) may help in tuning the emission to preferably occur in the ZPL band.

5.2 Resonant excitation in NV^-:NDs

In this experiment, a solution of NV^- doped NDs (Adamas) in water was drop-casted on a glass coverslip (No. 1) with SiO_2 microsphere particles 9.4 μm in diameter each (Cospheric). The solution was dried in an oven at 80 °C. The glass spheres coalesced and self assembled

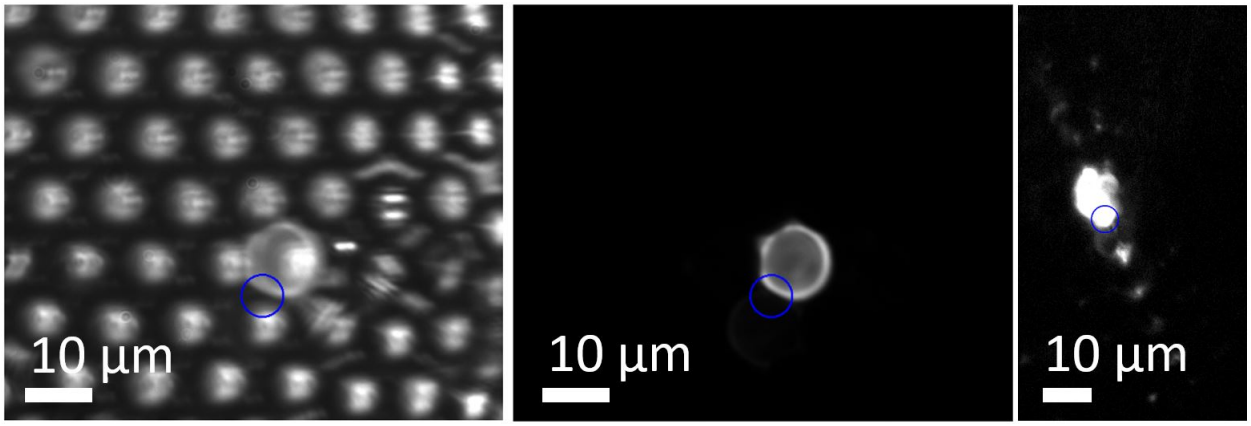

Figure 5.1: a) A dark-field optical image of SiO_2 spheres coated with NV^-:NDs with back light on b) and back light off. The blue circle shows the focal spot location of the incident 532 nm laser. c) A dark-field image of the same sample when the laser spot is carefully adjusted to excite the edge of another sphere. [in preparation]

into a hexagonally packed monolayer as shown in the dark field optical image in Figure 5.1a and b. A 532 nm excitation beam was focused at the blue circle and the sample was imaged after filtering the scattered laser light using a 532 nm notch filter. Figure 5.1b shows the optical image of the sample with the lamp light switched off. An intense glowing ring of NV^-:NDs florescence enhanced due to the whispering gallery modes was observed from around a sphere when the edge of the sphere was excited with a 532 nm laser spot focused at its edge. The emission intensified further when the laser spot location was adjusted such that a coupled resonant mode was excited across a linear chain within multiple spheres as shown in Figure 5.1b.

The spectra from these emission is measured and is shown in Figure 5.2a, b and c. The enhanced spectrum (Figure 5.2 a) corresponding to the excitation scheme shown in Figure 5.1a,b consists of typical NV^- spectral features with emission enhanced in certain wavelength bands at regular intervals. The overall integrated intensity was nearly 4-6 times higher than

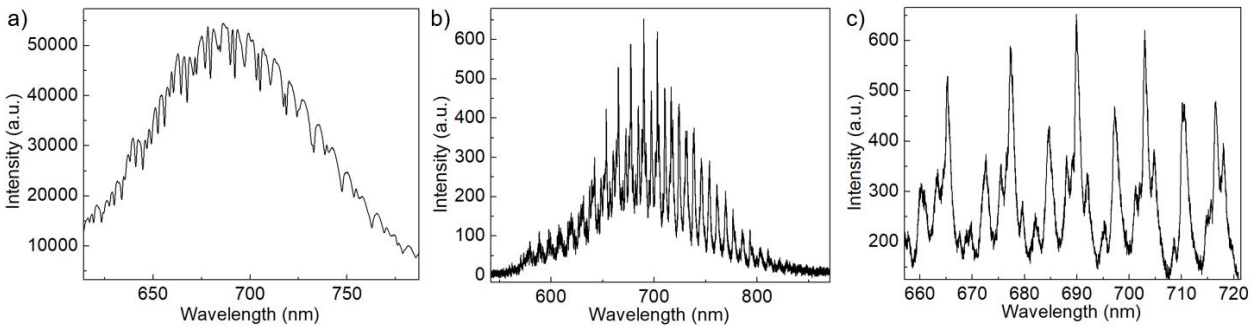

Figure 5.2: a) The room temperature PL spectra from NV^-:NDs using the excitation scheme in Figure 5.1a, b and b) using the excitation scheme shown in Figure 5.1c. c) A 660-720 nm close up of the spectrum shown in b. [in preparation]

the emission observed compared to when the sphere is excited at the center. Figure 5.2b shows the spectrum recorded by using a 1200 lines/mm grating. It shows the sharp resonant modes corresponding to the excitation scheme shown in Figure 5.1c. A close up of the spectrum in the 660-720 nm range is shown in Figure 5.2b. The peak widths range from 0.88 to 1.4 nm.

5.2.1 Photothermal Heating of NV^-:NDs on SiO_2 Microspheres

Due to the limited access to a tunable laser source, only photothermal heating experiments with a CW 532 nm laser were conducted on individual ND coated SiO_2 spheres. The cooling performance was not evaluated. The samples were prepared as discussed in the previous section. A smaller quantity of spheres was used in this case to locate isolated individual spheres. For calibrating the change in DWF with temperature, the coverslip was attached to a cryostat chamber using a double sided copper tape. A single isolated sphere coated with NDs (Figure 5.3a) was located and a 532 nm beam was focused to a diffraction limited laser spot at the area shown using the yellow circle in the inset of Figure 5.3a. The back-scattered light was filtered using a 532 nm notch filter and focused into the slit of a spectrometer. The

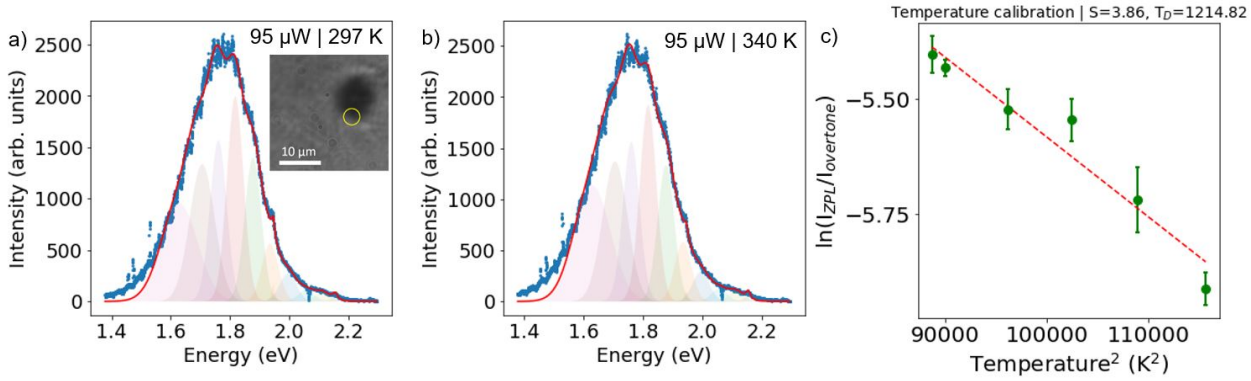

Figure 5.3: a) The room temperature (297 K) emission spectrum measured using 95 μW 532 nm focused diffraction limited spot. The inset shows the single silica sphere coated with NV^- doped NDs placed on a glass coverslip. The location of the 532 nm spot is shown in the inset using a yellow circle. b) The emission spectrum measured at 340 K, while the other parameters remained constant. The spectra were fit using the method discussed in section 2.8.1 The individual components are shown using filled areas and the sum total of all the fit components is shown in red. c) The natural log of DWF is plotted against temperature squared. The dotted line shows a fit to the eq. 2.13. [in preparation]

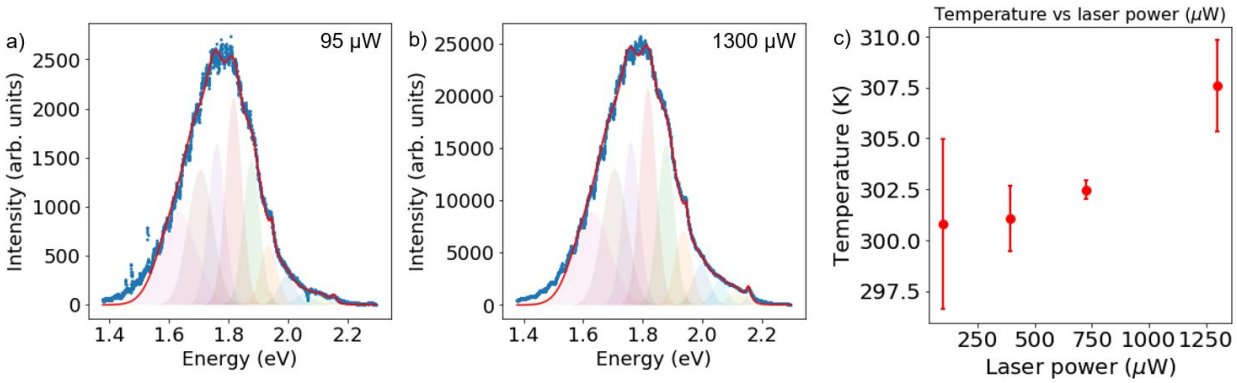

Figure 5.4: a) The emission spectrum measured using 95 μW and b) 1300 μW of 532 nm focused diffraction limited spot. The spectra were fit using the method discussed in section 2.8.1 The individual components are shown using filled areas and the sum total of all the fit components is shown in red. c) The temperatures obtained using the calibration shown in Figure 5.3c at various laser powers. [in preparation]

emission spectra measured at room temperature (297 K) and 340 K using a 95 μW laser power are shown in Figure 5.3a and b, respectively. The spectra consisted of consecutive peaks and valleys due to the enhanced emission at selected wavelengths from the whispering gallery modes. Due to the presence of this interference, the individual fit to the ZPL line was not possible. Therefore the DWF was calculated using the composite function amplitude fitting method discussed in section 2.8.1. The DWF values for each temperature are shown in Figure 5.3c. At each temperature, six individual spectra were measured and fit to obtain the DWF values. The average value is shown using the data points and the error bars represent one standard deviation. A fit to this data using the equation eq. 2.13 is shown using a red dashed line. The Debye temperature (T_D) and the electron-phonon coupling (s) parameters obtained were 1214.8 K and 3.86, respectively.

In the experiment to measure the photothermal heating, six spectra were measured at each laser power. The representative spectra and the respective fits at 532 nm laser powers

95 and 1300 μW is shown in Figure 5.4a and b, respectively. Little difference is qualitatively observable in these spectra, however the DWF calculation can be used to resolve the small changes. The DWF was calculated using the six spectra at each laser power and the average at the corresponding laser power is plotted in Figure 5.4. The errorbars represent one standard deviation. The DWF was converted to the calibrated absolute temperature using the calibration shown in Figure 5.3c. A temperature increase of nearly 8 K was recorded from lowest laser power to the highest laser power. However, since the lowest laser power is relatively noisier due to the smaller signal to noise ratio, the average DWF overestimates the temperature. The expected temperature at such low laser powers is expected to be around the room temperature (297 K) $\pm$1 K. Therefore the overall temperature increase at the highest laser power of 1250 μW is closer to 10 K.

5.2.2 Analytical heat transfer theory for spheres with local sources

The local heating sources (NDs) on the non-absorbing SiO_2 medium can be modeled using the spherical heat transfer theory discussed in this section. If the number of NDs is known, by obtaining the location of individual ND, the following analytical heat transfer theory may be used to estimate the power generated by each ND particle.

For a sphere shaped geometry (Figure 5.5), a solution of the heat-transfer equation is derived below.

The energy equation that applies is expressed in spherical coordinates as:

$$\rho\hat{C}\frac{\partial T}{\partial t} = \frac{\kappa_s}{r^2}\left[\frac{\partial}{\partial r}\left(r^2\frac{\partial T}{\partial r}\right) + \frac{1}{\sin\theta}\frac{\partial}{\partial\theta}\left(\sin\theta\frac{\partial T}{\partial\theta}\right) + \frac{1}{\sin^2\theta}\frac{\partial^2 T}{\partial\phi^2}\right] + S(r,\theta,\phi), \tag{5.1}$$

for a sphere type geometry, where ρ is the mass density, $\hat{C}$ is its specific heat capacity per unit mass and κ_s is its thermal conductivity of the sphere. The sphere is surrounded by a stagnant fluid (κ_f) on all sides and the temperature far away from the boundaries is T_∞. Symmetry is assumed about the y axis. It is convenient to write the energy equation for the

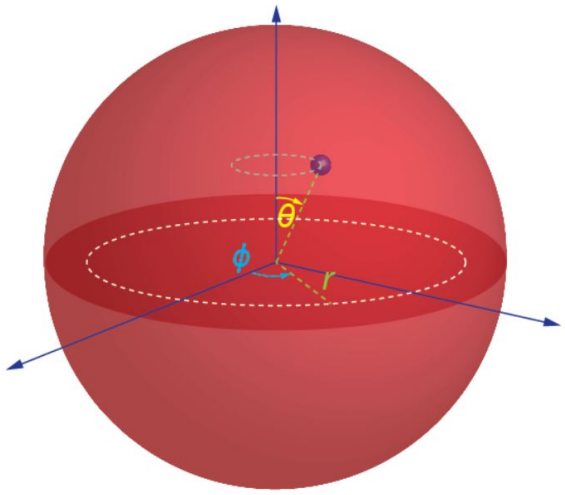

Figure 5.5: Geometry and the spherical coordinate system used to obtain the analytical heat transfer solution of of the geometry with point sources.

geometry in dimensionless form as:

$$\frac{\partial \Theta}{\partial \tau} = \frac{1}{x^2}\left[\frac{\partial}{\partial x}\left(x^2\frac{\partial \Theta}{\partial x}\right) + +\frac{1}{\sin\theta}\frac{\partial}{\partial \theta}\left(\sin\theta\frac{\partial \Theta}{\partial \theta}\right) + \frac{1}{\sin^2\theta}\frac{\partial^2 \Theta}{\partial \phi^2}\right] + \sigma. \tag{5.2}$$

where the dimensionless parameters are defined by

$$\Theta = \frac{T - T_\infty}{T_\infty}, \tau = \frac{\kappa_s t}{\rho \hat{C} a^2}, x = \frac{r}{a}, \sigma = \frac{S a^2}{\kappa_s T_\infty}, \tag{5.3}$$

where S is the source function which is given as the rate of heat generation $(\dot{Q})$ at the coordinates $P(x_1, \theta_1, \phi_1)$ per unit volume. If the volume of the localized source is $V_c = a^3 x_1^2 \Delta x_1 (\Delta\theta_1)^2$, the dimensionless source is given as

$$\sigma = \frac{\dot{Q}}{\kappa_s T_\infty a x_1^2 \sin\theta_1 \Delta x_1 (\Delta\theta_1)^2}, \tag{5.4}$$

where the dimensions of the localized source in each coordinate are $\Delta x_1, \Delta\theta_1$ and $\Delta\phi_1$ Assuming the source spans equally in θ and ϕ, the dimension is given as

$$\Delta\theta_1 = \Delta\phi_1 = \sqrt{\frac{V_c}{x_1^2 \sin\theta_1 \Delta x_1^2}}. \tag{5.5}$$

For the temperatures involved here radiant energy transfer is negligible. The boundary conditions are given by:

$$-\kappa_s \frac{\partial \Theta}{\partial x}(1) = -\frac{ha}{\kappa_s}\frac{(T|_{x=a} - T_\infty)}{T_\infty} = Bi\Theta(1); \frac{\partial \Theta}{\partial \phi}(0,\pi) = 0, \tag{5.6}$$

where the Biot number is $Bi = \frac{-\kappa_f}{\kappa_s}$ and h is the heat transfer coefficient. For a sphere in a stagnant medium, the Nusselt number $Nu = 2ah/\kappa_f$. This gives $ha = \kappa_\infty$.

The solution may be written in terms of orthonormal eigenfunctions to give

$$\Theta(x,\theta,\phi) = \sum_{l=0}^{\infty}\sum_{m=0}^{\infty}\sum_{n=0}^{\infty} A_{lmn}(\tau)U_{lm}(x)V_{ln}(\theta)W_n(\phi), \tag{5.7}$$

where the eigenfunctions $U_{lm}(x)$, $V_l n(\theta)$ and $W_n(\phi)$ are given by

$$U_{lm}(x) = j_l(\lambda_{lm}x) = \sqrt{\frac{\pi}{2\lambda_{lm}x}}J_{l+\frac{1}{2}}(\lambda_{lm}x), \tag{5.8}$$

where the eigenvalues λ_{lm} satisfy

$$(l - 1 + Bi)j_l - 1(\lambda_{l,m}) - \lambda_{l,m}j_l(\lambda_{lm}), \tag{5.9}$$

$$V_{ln}(\theta) = P_n^l(z), \text{ where } z = \cos\theta \text{ and } l, n = 0, 1, 2...; l \geq n, \tag{5.10}$$

where $P_n^l(z)$ are the Associated Legendre polynomials with order n and degree l.

$$W_n(\phi) = \cos(n\phi) \text{ for } n = 0, 1, 2, ... \tag{5.11}$$

$$. \tag{5.12}$$

The coefficients $A_{lmn}(\tau)$ are given by

$$\begin{aligned} A_{lmn}(\tau) = \quad & \frac{2[1 - \exp(-\lambda_{lm}^2\tau)]}{\lambda_{lm}^2}\int_{x_1}^{x_1+\Delta x_1}\int_{\theta_1}^{\Delta\theta_1}\int_{\phi_1 0}^{\phi 1+\Delta\phi_1} \\ & \sigma(x',\theta',\phi')\frac{x'^2 U_{lm}(x')}{||U_{lm}||^2}\frac{V_{ln}(\theta')}{||V_{ln}||^2}\frac{W_n(\phi')}{||W_n||^2}dx'd\theta'd\phi', \end{aligned} \tag{5.13}$$

The norms are given as

$$||U_{lm}||^2 = \int_0^1 x[U_{lm}(x)]^2, \quad ||V_{ln}||^2 = \frac{(l+n)!}{n(l-n)!}, \quad ||W_n||^2 = \pi. \tag{5.14}$$

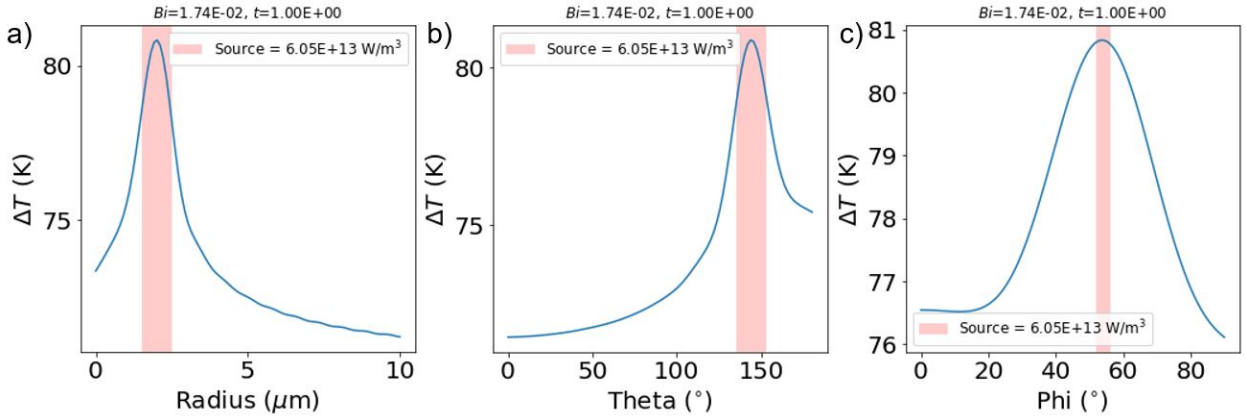

Figure 5.6: a) The steady state state temperature change within a 10 μm glass sphere with a 1 W localized heat source (P) was placed at $P(5\mu m, 144°, 54°)$ along the radial direction, b) along the θ direction and c) along the ϕ direction. The source span is shown in all three axial directions in red. [in preparation]

Calculations for steady state temperatures were performed for a glass sphere of radius 10 μm with thermal conductivity(κ_s), specific heat capacity($\hat{C}$) and mass density (ρ) taken as 1.38 W/(m K), 630 J/(Kg K) and 2200 Kg/m^3, respectively. The glass sphere was levitated in a stagnant air medium of conductivity (κ_f) 0.024 W/(m K). Experimentally, this may be achieved using laser trapping. A 1 W localized heat source (P) was placed at $P(5\mu m, 144°, 54°)$. The source spanned 500 nm, 8.5° and 2.14° in the x, θ and ϕ coordinates. The steady state temperatures along the three coordinate directions passing orthogonally throught the center of the source are shown in Figure 5.6.

The temperature change gradient within the sphere is smaller compared to the overall temperature change. This is because of the low thermal conductivity of the surrounding stagnant medium, resulting in a small Bi number. To visualize the gradient of change in temperature with time, the Figure 5.7a shows the temperature change gradient within the sphere along the radial direction. The temperature reaches steady state temperatures in

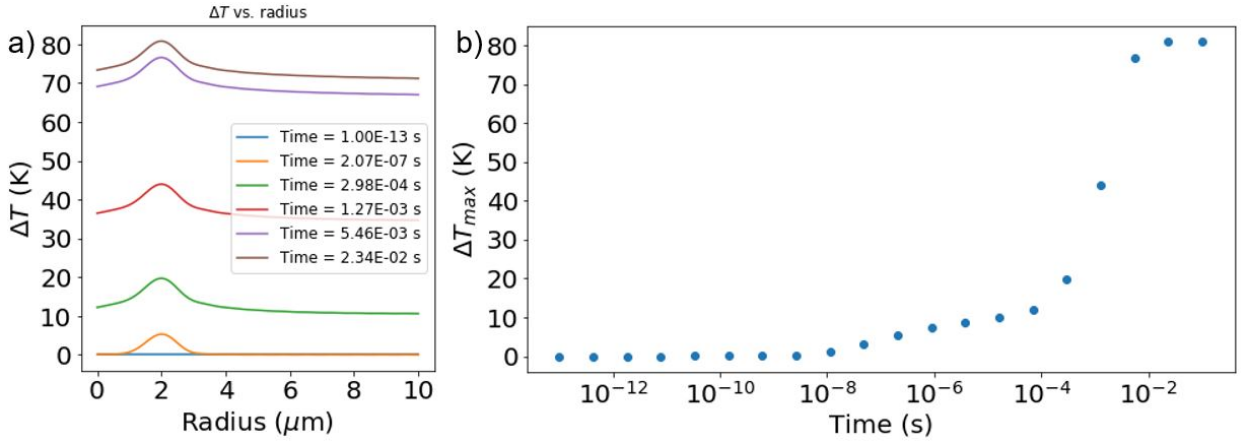

Figure 5.7: a) The time dependent temperature gradient along the radial direction for the 10 μm glass sphere. b) The maximum temperature change within the sphere is plotted against time to visualise the time scale dynamics. [in preparation]

very long time scales of 20 ms. This is primarily due to the low thermal conductivity of the surrounding fluid.

5.2.3 Analytical heat transfer theory for cylinders with local sources

For a cylinder shaped geometry (Figure 5.8), a solution of the heat-transfer equation is derived below.

The energy equation that applies is expressed in cylindrical coordinates as:

$$\rho\hat{C}\frac{\partial T}{\partial t} = \kappa\left[\frac{1}{r}\frac{\partial}{\partial r}\left(r\frac{\partial T}{\partial r}\right) + \frac{1}{r^2}\frac{\partial^2 T}{\partial \theta^2} + \frac{\partial^2 T}{\partial z^2}\right] + \dot{Q}''', \tag{5.15}$$

for the cylinder type geometry, where ρ is the mass density, $\hat{C}$ is its specific heat capacity per unit mass and κ_M is its thermal conductivity. The cylinder is attached to a large conductive heat sink at temperature T_b across one of the circular faces and is surrounded by a fluid of thermal conductivity κ_f around all of the other surfaces. For a half-cylinder geometry with symmetry about $\theta = 0, \pi$ of height H, radius a and $0 < \theta < \pi$, it is convenient to write the

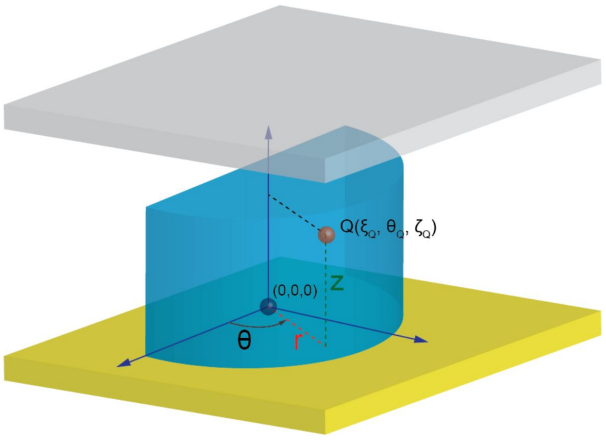

Figure 5.8: Geometry and the cylindrical coordinate system used to obtain the analytical heat transfer solution of of the half-cylinder geometry with a localized source shown using a red sphere. The substrate and the glass coverslip at room temperature is shown using a yellow and a grey slab, respectively.

energy equation for the geometry in dimensionless form given by.

$$\frac{\partial U}{\partial \tau} = b^2 \left[\frac{1}{\xi} \frac{\partial}{\partial \xi} \left(\xi \frac{\partial U}{\partial \xi} \right) + \frac{1}{\xi^2} \frac{\partial^2 U}{\partial \theta^2} \right] + \frac{\partial^2 U}{\partial \zeta^2} + \sigma, \tag{5.16}$$

where the dimensionless parameters are defined by

$$U = \frac{T - T_b}{T_b}, \tau = \frac{\kappa_M t}{\rho \hat{C} H^2}, \xi = \frac{r}{a}, \zeta = \frac{z}{H}, \sigma = \frac{\dot{Q}''' H^2}{\kappa_M T_b}, \tag{5.17}$$

where $\dot{Q}'''$ is the energy of source per unit volume per unit time for a source of Q (Watt) at ξ_Q, θ_Q, ζ_Q, distributed uniformly over a volume of size $\mathrm{d}r, \mathrm{d}\theta$ and $\mathrm{d}z$ in the cylindrical coordinates. It is given as

$$\dot{Q}''' = \frac{Q}{[a\xi_Q d\theta][ad\xi][Hd\zeta]} \tag{5.18}$$

For the temperatures involved here radiant energy transfer is negligible. The boundary

conditions are given by:

$$\frac{\partial U}{\partial \xi}(0,\theta,\zeta,\tau)=0, \frac{\partial U}{\partial \xi}(1,\theta,\zeta,\tau)=-Bi_c U(1,\theta,\zeta,\tau),\ \frac{\partial U}{\partial \theta}(\xi,0,\zeta,\tau)=\frac{\partial U}{\partial \theta}(\xi,\pi,\zeta,\tau)=0, \tag{5.19}$$

and

$$U(\xi,\theta,0,\tau)=0,\ \frac{\partial U}{\partial \zeta}(\xi,\theta,1,\tau)=-Bi_f U(\xi,\theta,1,\tau), \tag{5.20}$$

where Bi_c and Bi_f are Biot numbers corresponding to the surfaces at $\xi = 1$ and $\zeta = 1$, respectively. The Biot number for the radial direction ($Bi_c = ah/\kappa_M$), which is the ratio of heat transfer conducted away from a material to the heat transferred within a material. It is related to the appropriate heat transfer coefficient, $h = Nu\kappa_M/2a$, for heat transfer to the surrounding medium. The heat transfer coefficient for convective and conductive heat transfer is usually written in terms of the dimensionless Nusselt number, Nu, for cylinders in a stagnant fluid yields $Nu = 2ah/\kappa_M = 0.34$.[150] Similarly, in the z-direction, the Biot number is given as $Bi_f = H\kappa_f/\Delta x_s \kappa_M$, where Δx_s is the distance of the circular surface from the coverslip.

The solution may be written in terms of orthonormal eigenfunctions to give

$$U(\xi,\theta,\zeta,\tau)=\sum_{l=0}^{\infty}\sum_{m=0}^{\infty}\sum_{n=0}^{\infty} A_{lmn}(\tau)X_{lm}(\xi)Y_m(\theta)W_n(\zeta), \tag{5.21}$$

where the eigenfunctions $X_{lm}(\xi)$, $Y_m(\theta)$ and $W_n(\zeta)$ are given by

$$X_{lm}(\xi)=J_m(\mu_{lm}\xi), \tag{5.22}$$

$$Y_m(\theta)=\cos(m\theta) \text{ for } m=0,1,2,..., \tag{5.23}$$

$$Z_n(\zeta)=\sin(\omega_m\zeta), \tag{5.24}$$

where μ_{lm} satisfies

$$\mu_{lm}[J_{m-1}(\mu_{lm})]=(m-Bi_c)J_m(\mu_{lm}) \text{ for } l,m=0,1,2,... \tag{5.25}$$

and ω_n satisfies

$$\omega_n \cos(\omega_n) = -Bi_f \sin(\omega_n) \text{ for } n = 0, 1, 2, ... \tag{5.26}$$

The coefficients $A_{lmn}(\tau)$ are given by

$$\begin{aligned} A_{lmn}(\tau) = \quad & \frac{2[1 - \exp(-\lambda_{lmn}^2 \tau)]}{\lambda_{lmn}^2} \int_{\xi_1}^{\xi_2} \int_{\theta_1}^{\theta_2} \int_{\zeta_1}^{\zeta_2} \\ & \sigma(\xi', \theta', \zeta') \frac{\xi' X_{lm}(\xi')}{||X_{lm}||^2} \frac{Y_m(\theta')}{||Y_m||^2} \frac{W_n(\zeta')}{||Z_n||^2} d\xi' d\theta' d\zeta', \end{aligned} \tag{5.27}$$

where the primes indicate dummy variables of integration, $\lambda_{lmn}^2 = b^2 \mu_{lm}^2 + \omega_n^2$, where $b = H/a$, and the norms are given by

$$||X_l||^2 = \int_0^1 \xi' [J_m(\mu_{lm} \xi')]^2 d\xi' \text{ for } l, m = 0, 1, 2, ..., \tag{5.28}$$

$$||Y_m||^2 = \begin{cases} 2\pi & \text{for } m = 0 \\ \pi & \text{for } m = 1, 2, 3, ... \end{cases} \tag{5.29}$$

$$||Z_m||^2 = \int_0^1 [\sin(\omega_n \zeta')]^2 d\zeta' \text{ for } n = 0, 1, 2, ... \tag{5.30}$$

The integration limits are given as

$$\xi_1, \xi_2 = \xi_Q - d\xi/2, \ \xi_Q + d\xi/2 \tag{5.31}$$

$$\theta_1, \theta_2 = \theta_Q - d\theta/2, \ \theta_Q + d\theta/2 \tag{5.32}$$

$$\zeta_1, \zeta_2 = \zeta_Q - d\zeta/2, \ \zeta_Q + d\zeta/2 \tag{5.33}$$

The calculations were performed for diamond cylindrical pillar of radius and height = 10μm which may be fabricated using either focused ion beam milling or traditional clean room vertical etching methods such as deep reactive ion etching (DRIE). The pillar is affixed on one of its circular surfaces to a large conductive diamond substrate is considered for

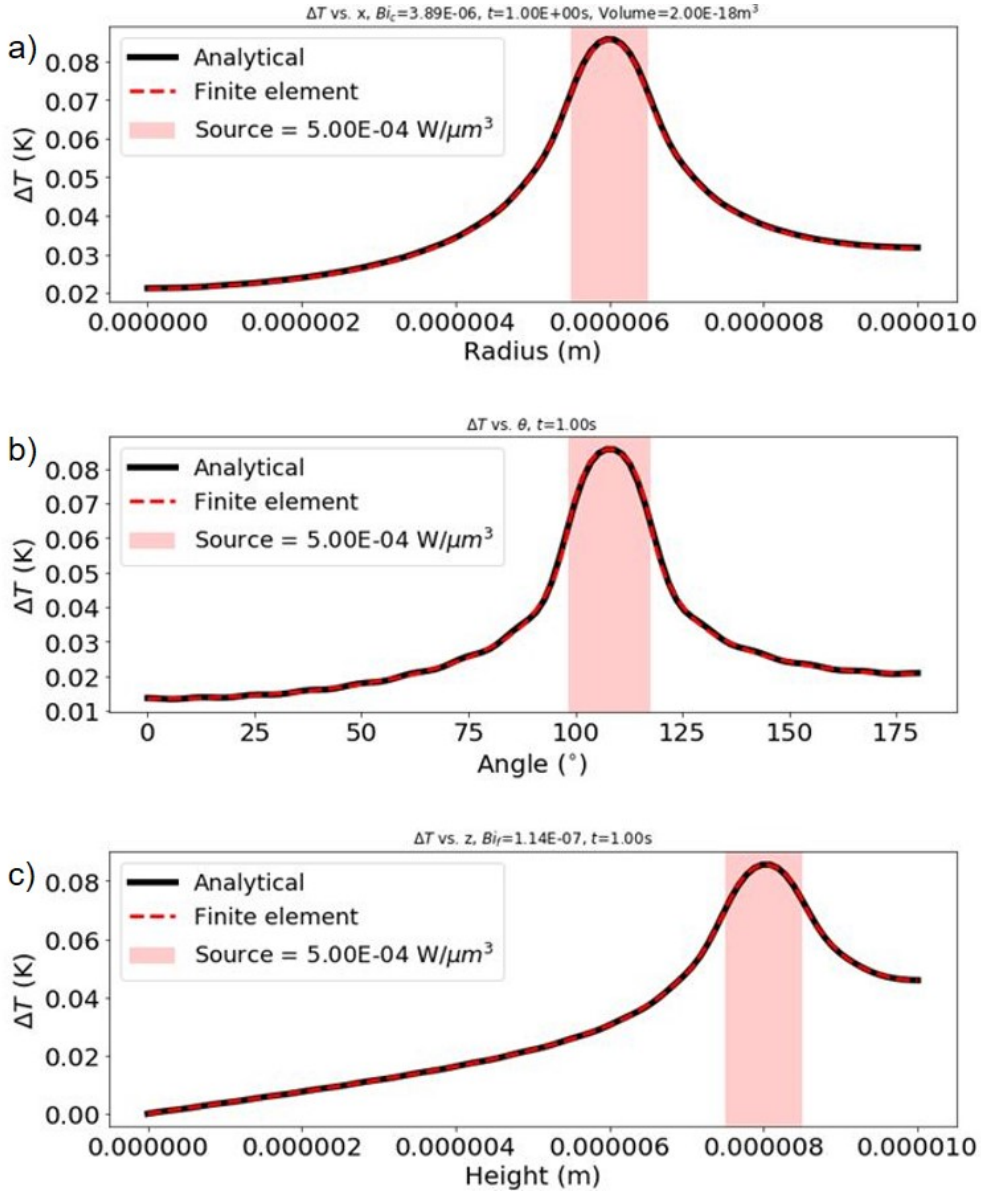

Figure 5.9: The steady state temperature distributions for a symmetric half-cylinder geometry with a single point source calculated along the radial, angular and z-directions using analytical (black) and finite element methods (red dashed line). The source location and spans are shown in red. [in preparation]

the heat transfer calculations. The physical constants, thermal conductivity, specific heat capacity and the mass density of the diamond medium are given as $\kappa_s = 2200$ W/(m k), $\hat{C} =$ 630 J/(kg K) and $\rho = 4860$ Kg/m^3. The pillar is surrounded by a stagnant air medium (κ_f = 0.024 W/(m K)) on all the sides and coverslip 1 mm away from the top circular surface of the cylinder is maintained at room temperature. A 1 mW localized source is placed at a radial position of $x = 6$ μm, $\theta = 108^\circ$ and $z = 6\mu$m which spans 1 μm, 19.1 $^\circ$ and 1 μm in the respective 3 axial directions. The temperature change gradients calculated using the analytical theory discussed above are shown in the Figure 5.9a, b and c along the respective axial directions x, θ and z (Black lines), passing through the center of the source location respectively. The corresponding temperature changes calculated using the same parameters in COMSOL (finite-element analysis) are shown using a red-dashed line. Both the methods agree with each other.

The time dependent temperature change gradients along the radial direction passing through the center of the localized source is shown in Figure 5.10a. The overall temperature gradient within the geometry is significant despite the large difference between the thermal conductivity of the material and the surrounding stagnant fluid because a large amount of heat transfer occurs in the z-direction towards the substrate kept at room temperature. The maximum temperatures within the volume with time is plotted in Figure 5.10b. The temperature change reaches a steady state very rapidly (<1 μs) considering the large size of the diamond cylinder. This is due to the rapid heat transport pathway along the negative z-direction towards the substrate at room temperature.

5.3 H3 centers for laser refrigeration

In diamonds, H3 center is a nitrogen–vacancy–nitrogen chain that is formed when a vacancy is trapped next to the A-aggregate of nitrogen. It is a photostable defect which emits brightly in the range of 500-700 nm with a ZPL at 503 nm with the corresponding wide emission from the phonon side bands. It requires excitation irradiances of more tha 10 MW/cm^2 for saturation. In addition to being highly photostable, it has been shown to perform as

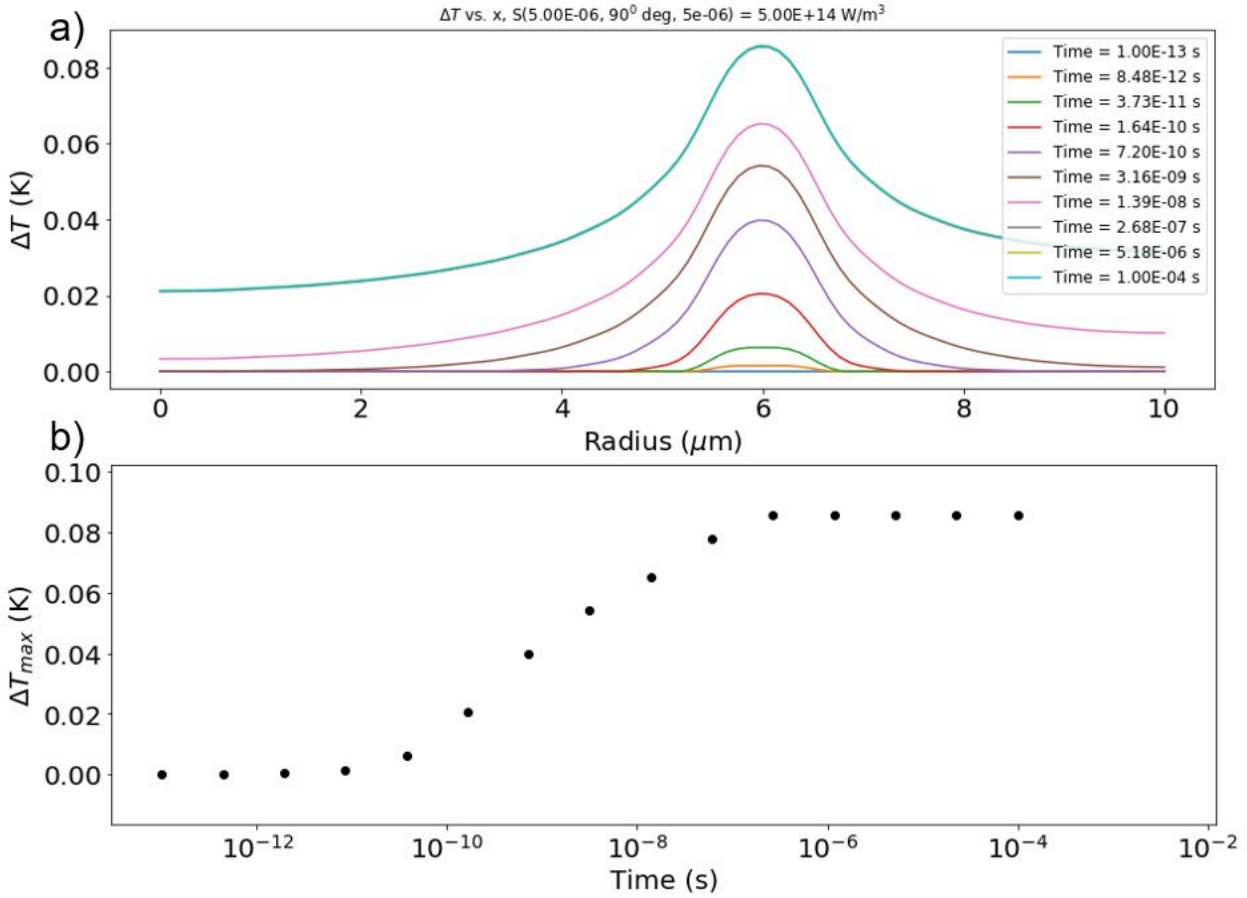

Figure 5.10: The temperature distributions for a symmetric half-cylinder geometry with a single point source calculated along the radial, angular and z-directions using analytical and finite element methods. [in preparation]

a tunable laser with practically unlimited shelf life in the visible range of 500-600 nm[151]. Considering action and its bright emission, H3 center appears to be a great candidate for further exploration for radiation balanced lasers where anti-Stokes fluorescence may be used to cool a solid-state laser gain media internally to negate the heat produced in it.

5.4 H3 diamond heating experiments

An optical setup shown in Figure 5.11a designed to collect the emission from macroscopic diamonds excited locally was used to explore the photothermal properties of the H3 center, two diamond samples (shown in Figure 5.11b and c) were studied. The optical setup for the excitation of the diamond sample uses focused laser spots of a green CW 532 nm or a blue 455 nm. The laser beams were focused using a 50X long working distance objective and the back scattered emission was collected using the same objective. The transmitted part of the emission from a beam splitter (BS) was filtered using a notch filter (NF) to remove the scattered 532 nm photons or 500 nm long pass filter to remove the 455 nm light. The emission was then reflected using a mirror (M) and focused into the spectrometer slit using a focusing lens (FL). A thermoelectrically cooled charge coupled device (TEC-CCD) was used to record the spectra. Additionally, a 20 μm thick insulated copper wire loop was added near the focal spot to induce a variable frequency microwave (MW) source to measure the optically detected magnetic resonance.

The diamond sample shown in Figure 5.11b was hexagonal in shape (H3) and predominantly contained nitrogen defects in the form of H3-centers or NVN-centers. It was yellow around the central area and the areas away from the center had a red/purple hue. The area with the red/purple hue was believed to have a higher proportion of NV^0 and NV^- centers. For the purposes of these experiments, the central area (white circle), which is shown to have a high proportion of H3 center to other defects, was used. The second sample shown in Figure Figure 5.11c was triangular in shape (NV) and had a bright red/purple hue overall. The samples were affixed to the cryostat stage using a double-side copper tape. The focal spot of lasers was maintained 10 μm below the top surface of the diamonds. The focal

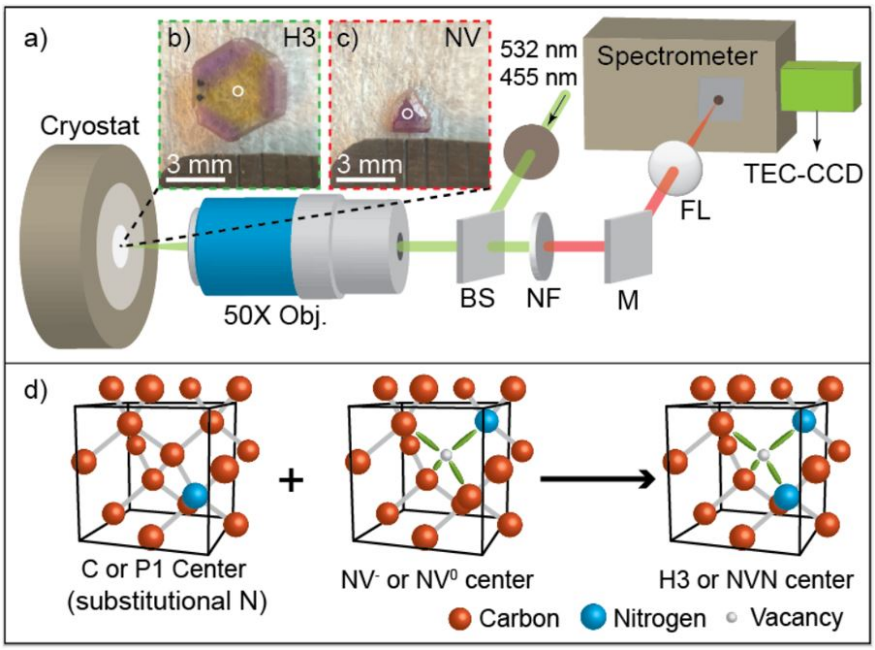

Figure 5.11: a) The optical setup for the excitation of the diamond sample using a focused 532 or 455 nm laser spot. The back scattered part of the emission is collected using the 50X long working distance objective (50X obj.), transmitted through a beam splitter (BS), filtered using a notch filter (NF) or 500 nm long pass filter, reflected using a mirror (M) and focused into the spectrometer slit using a focusing lens (FL). A thermoelectrically cooled charge coupled device (TEC-CCD) was used to record the spectrum. b) The H3 diamond sample with predominant nitrogen doping in the form of NVN or H3 centers, and c) the NV diamond with predominantly NV centers. The white circle represents the area where the 532 nm spot was focused on the respective diamond. d) A schematic showing the mobilization and integration of substitutional nitrogen (C-centers or P1 centers) with NV0 and NV- centers at high pressure and temperature to form NVN or H3 centers. [in preparation]

volume heated and probed using the lasers was limited to <100 μm^3. Also, considering the highly absorptive thick diamond sample compared to the laser spot size, the divergent beam reaching the lower part of the diamond substrate was very low in irradiance and caused negligible heating of the copper tape. The mechanism with which the H3-centers are formed in a diamond are shown in Figure 5.11d. The H3 diamond was treated at high-pressure and high-temperature ($\sim$ 1600 °C) [152] conditions at which the NV^0 and NV^- were mobile enough to seek the P_1 substitutional nitrogen defects and form the NVN or H3 centers.

The stokes part of the emission spectra was collected from the H3 and NV diamonds using a 532 nm excitation are shown in black and red in Figure 5.12, respectively. The emission wavelength of NV^0 and NV^- ZPLs are marked using a yellow and red dashed line centered at 575 and 638 nm, respectively. The counts are normalized using the laser power used and the collection time. A 11 times higher integrated emission intensity was measured from the NV diamond. The significantly high magnitude of emission compared to the H3 sample shows that a significantly higher concentration of NV centers are present within the NV diamond. The inset of Figure 5.12a shows the modulation in the emission intensity from the NV diamond using a microwave (MW) frequency sweep from 2.86 to 2.88 GHz. A stronger (as compared to a weaker) emission is seen when the excitation from the excited state to the ground state while the NV^- center is in the m_s=0 state (versus the weakest emission when the MW is resonant with the with $m_s = \pm 1$ states). The weaker emission associated with $m_s = \pm 1$ results from a stronger non-radiative coupling to the singlet energy level through intersystem crossing. This is described in more detail in the section 2.9. And the splitting in the $m_s = \pm 1$ (weakest emission) states is due to the combination of pseudo magnetic field created by strains within the sample. The anti-Stokes part of the emission spectra collected from the H3 and NV diamonds using a 532 nm excitation is shown in black and red in Figure 5.12b, respectively. Strong anti-Stokes emission from the H3 centers is observed in the H3 diamond, while it is completely absent in the NV diamond. A green dashed line shows the H3 ZPL center wavelength at 503 nm with the red-shifted wide Gaussian phonon side band. The presence of anti Stokes fluoresence is exciting in the context of laser refrigeration and

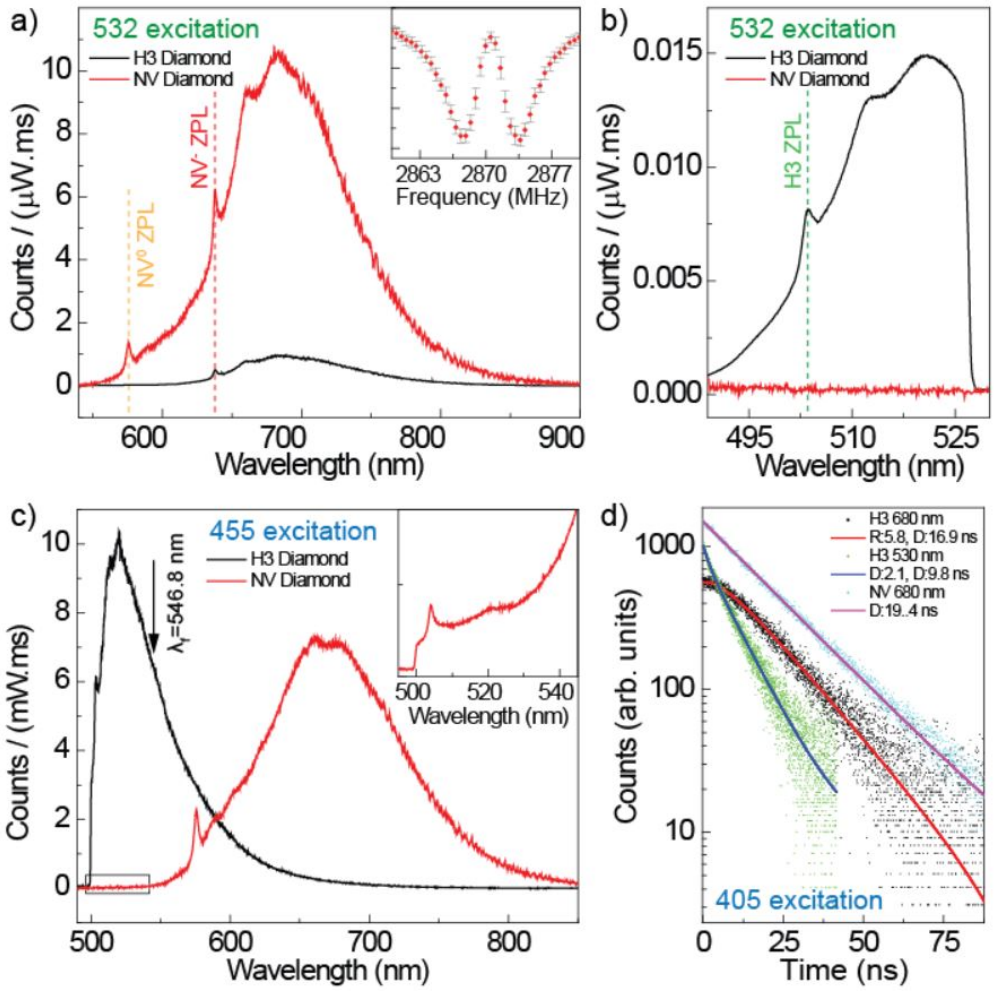

Figure 5.12: a) Normalized room temperature spectra of NV^0 and NV^- emission from both H3 (black) and NV (red) center using a 1 mW 532 nm laser excitation spot. The inset shows the ODMR spectrum measured from the NV diamond. b) The anti-Stokes wavelength band spectra for both the H3 (black) and NV (red) samples using 532 nm excitation. c) Normalized room temperature full-range spectra using a 455 nm laser excitation spot. d) Measured and exponential fitted lifetime data for H3 sample in the 680 and 530 nm bands and NV sample in the 680 nm band. The 'R' and 'D' in the legend represent the rise and decay times from the double-exponential and exponential fits. [in preparation]

motivates conducting experiments in the future to evaluate the efficiency of this process at different excitation wavelengths. The spectra was cut off at 527 nm due to the notch filter used to remove the scattered 532 nm laser. The Stokes part of the emission spectra from the H3 and NV diamond spots measured using a focused 455 nm laser excitation is shown in Figure5.12c black and red, respectively. The emission from the H3 diamond predominantly consist of emission from the H3 ZPL at 503 nm and a broad phonon overtone emission with a center around 530 nm, representing a relatively high concentration of the H3 centers in the sample. The instrument induced intensity variation with wavelength was corrected using the method described in section 2.6.4 to obtain the mean wavelength at 546.8 nm. This is important for laser refrigeration applications as only wavelengths red-shifted to this wavelength can be used to observe net cooling of diamonds through H3 centers doped in them. The emission from the NV diamond predominantly consists of the emission from the NV0 ZPL at 575 nm and a broad phonon overtone centered around 680 nm. The weak NV- ZPL emission at 638 nm is due to strong photoionization of NV^- centers to NV^0 using the 455 nm laser. The emission from the NV center primarily occured from the NV centers where a large emission intensity ($\sim$36.3%) was from the NV^0. The large emission intensity from the NV^0 indicates the efficient ionization of NV^- due to the high energy of the incident laser (455 nm). A very small amount of emission intensity in the NV diamond was from the H3 center due to the very low concentration of H3 centers in this sample. This is indicated using a grey box and the close up is shown in the inset of Figure 5.12c.

Lifetime measurements were conducted on the H3 diamond around the 530 (maximum of H3 center phonon overtone emission) and 680 (maximum of NV-center phonon overtones) was measured using an unfocused 405 nm excitation pulse (Figure 5.12d). A 20 and 10 nm bands pass filter was used around the 680 nm and 530 nm band measurements, respectively. The measurements using an unfocused 405 nm excitation are shown in black and green, respectively. Double exponential fit to the 530 nm band decay spectrum show 9.8 and 2.1 ns decay components, corresponding to the fast and slow decay times of H3 luminescence from the defects in near and far away from A-aggregates, respectively. The time scales are

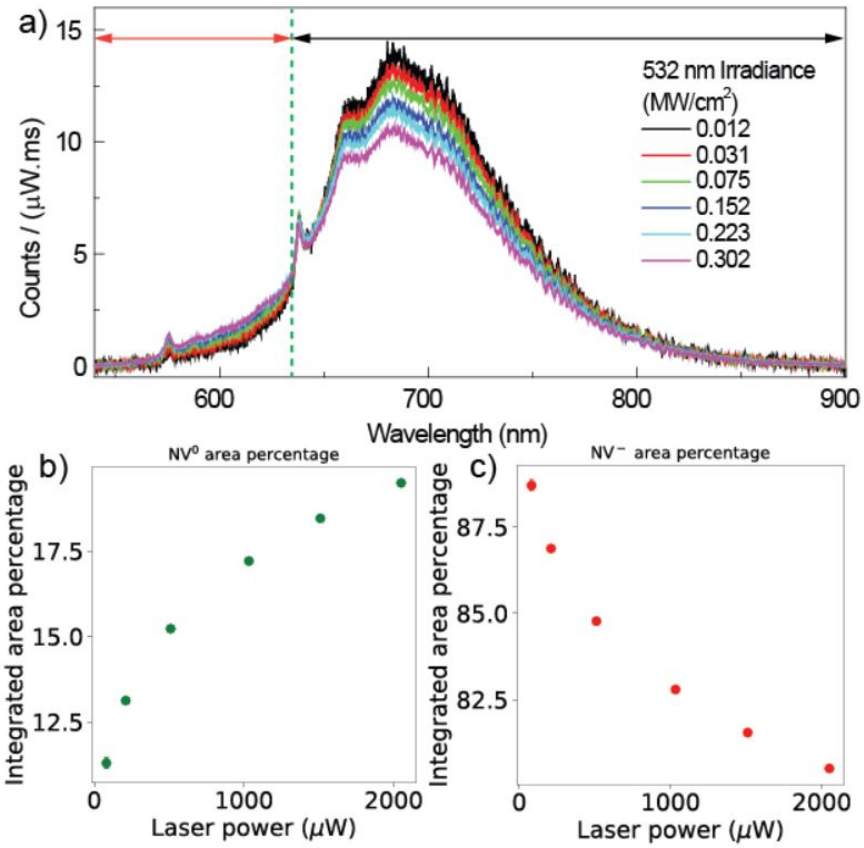

Figure 5.13: a) Room temperature normalized emission spectra from the NV diamond sample at various six different 532 nm irradiances. b) Percentage of integrated intensities of the NV^0 and c) NV^- emission intensity at the six different irradiances from the ZPL and overtones fit. [in preparation]

smaller than the intrinsic H3 lifetimes of ∼16.7 ns[153]. The short decay time component (2.1 ns) can be attributed to heavy quenching of H3 luminescence to other luminescent defects. Since an H3 centre is created from an A-aggregate plus a vacancy, or NV centers and P_1 centers, the spatial correlations are likely between the H3 centres and the A-aggregates, or NV centers[154]. The A-aggregates act as quenching centers, decreasing the lifetime of the H3 ensembles in closer proximity to them[154]. The 680 nm band emission shows a rise and a decay component with timescales of 5.8 and 16.9 ns, corresponding to excitation of the NV centers from the trapped H3 emission (like reabsorption and photon recycling effects in perovsike materials[155]) and the intrinsic NV^- center lifetime, respectively. The lifetime of emission in the 20 nm band around the 680 nm for the NV diamond sample is shown in Figure 5.12d (cyan). The data fits well to a single exponential with a decay time of 19.4 ns. This is much longer than the intrinsic lifetime of the NV^- center (12-13.5 ns [156, 157]), but much closer to the 21 ns intrinsic lifetime of the NV^0 center[158]. The high emission percentage from the NV^0 in the NV diamond sample's spectrum due to blue light excitation as seen in Figure 5.12c may contribute to these long time scales.

The room temperature emission spectra of the NV diamond sample were measured at 6 different laser irradiances are shown in Figure5.13. The measured counts were normalized using the laser power and acquisition times are shown on the y-axis. The vertical green dotted line signifies an arbitrary separation of the emission spectra such that - the left and right sides indicated using red and black lines represent the wavelength ranges in which the predominant amount of emission originates from the NV^0 center and NV^-, respectively. However, since the phonon overtones from the NV^0 are convoluted with the NV^-, a more sophisticated technique is required to measure the percentage of emission from the NV^0 as compared to the total emission. To calculate this, the method of fitting several spectra for the NV^0 and NV^- ZPLs and the overtones described in section 2.8.1 was used. The sum of the amplitudes of L_2 and $G_6 - G_9$ fit to the normalized spectra gave the emission from the NV^0 centers. The sum of amplitudes from the fit of all the other peaks gave the emission from the NV^- centers. The percentage of the respective charge state emission from NV^0 and

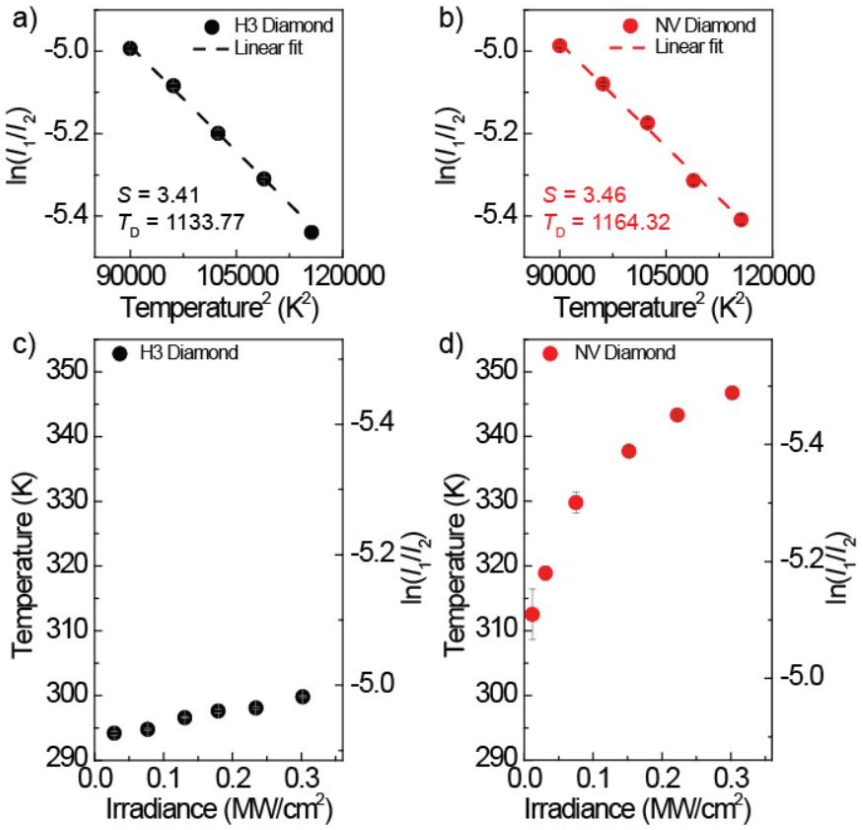

Figure 5.14: a) DWF temperature calibrations for the H3 and b) NV diamond samples. c) The irradiance dependent calibrated temperatures for the H3 and d) NV diamond samples. [in preparation]

NV^- was calculated and is plotted in Figure 5.13b and d, respectively. At higher irradiances the NV^- is dynamically ionized to NV^0 (and back) at a faster rate[159], causing the relative percentage of emission from the NV^0 to rise from 12 to 18 % as the laser power increases from 81 to 2050 μW. The decrease in the dynamic population of the NV^- suggests that the absorption by NV^- would progressively become smaller at higher irradiances as shown by Subedi *et al.*[160].

The temperature dependent measurement of the DWF on the H3 diamond was done

using a 12 KW/cm^2 532 nm laser irradiance. A fit to the DWF equation is shown using a black dashed line (Figure 5.14a), which gives the Debye temperature $T_D = 1133.7$ K and the electron-phonon coupling parameter $S = 3.41$. The same measurement was repeated on the NV diamond. A fit to the DWF equation is shown using a red dashed line (Figure 5.14b) which gives $T_D = 1164.3$ K and $S = 3.46$. These values were used to calibrate the laser irradiance dependent measurements to obtain the change in temperature as shown in Figure 5.14c and d respectively. The overall temperature change near the laser hot spot in the H3 diamond is close to 5 K at the highest irradiance. However at the same laser irradiance the NV diamond heats to temperatures 50 K higher than the room temperature. Note that the NV diamond sample does not heat linearly with the increase in laser irradiance, as one would expect for a material with constant absorption coefficient at a particular wavelength. The decrease in the dynamic population of the NV^- as shown in the previous figure suggests that the change in absorption with increased irradiance may be the reason for this.

The 10-times smaller heating effect in the H3 diamond can be attributed to the significantly lesser amount of NV centers in the sample as discussed above. This is encouraging for further exploration of methods to convert NV centers to H3 centers in a diamond sample. The ability to maintain a relatively high stable population of H3 centers in a sample may result in minimized heating which is advantageous considering its importance as a lasing medium. Additionally, the presence of anti-Stokes emission from the H3 center motivates its further exploration as a laser refrigeration color center for radiation balance lasers.

Chapter 6

CONCLUSIONS

The first chapter introduced the concept of photothermal heating to motivate the need for minimising its undesirable consequences. Following that laser refrigeration was discussed with an emphasis on semiconductor nanoscale devices. The second chapter gives a general overview of the process involved in calculating the steady state temperature and its transient dynamics. It was found that, despite having considered extremely low thermal conductance at the interfaces, the time scales to reach steady state temperatures for nanoscale materials such as the CdSNRs used by Zhang *et al.*[1] are nearly 4-5 orders of magnitude faster than reported. The chapter also introduces the challenges involved with temperature measurement of nanoscale materials and goes on to discuss a variety of non-contact temperature measurement methods, their advantages, disadvantages and other details involved in the accurate interpretation of temperatures using the respective measurement techniques. The discrepancy in the time scales may be explained because some of the limitations of the PPLT thermometry method may not have been accounted for by Zhang *et al.*[1]. When measuring temperatures using PPLT, it is important to account for the dependence of band-edge energies on the carrier excitation densities.

The laser refrigeration of CdSNRs was attempted in chapter 3, where various other complementary thermometry methods, optomechanical thermometry and Raman anti-Stokes Stokes ratio thermometry were used to measure the temperature of CdSNRs in rectangular or wedge shaped geometries. Laser refrigeration was not achieved. Analytical heat transfer theories developed to understand the transient temperature gradients in three different geometries (cantilever, wedge and bridge). To counteract the effects of photothermal heating in CdSNRs, experiments using 10% Yb:$LiYF_4$ have been discussed in chapter 4. By

mounting a 10% Yb:$LiYF_4$ microcrystal at the end of a CdSNR, laser refrigeration of the semiconductor nanoribbon was observed. A temperature drop of 20 K was measured using two complementary thermometry methods, optomechanical and ratiometric thermometry. Both the methods agree well with each other. Lastly, nanodiamond quantum sensors doped with NV^- centers were cooled by 27 K by attaching them to the 10% Yb:$LiYF_4$ microcrystal.

In chapter 5, the possibility of intrinsic laser refrigeration of semiconductors was explored by conducting experiments on NV doped diamonds on a silica microspheres. The silica acts as a whispering gallery mode resonator, causing enhancement of emission intensity in certain wavelength bands. Careful tuning of this cavity may be a great direction for the exploration of ZPL enhancement and possibly realizing laser refrigeration of diamonds using NV centers. The experiments in this work were only limited to photothermal heating. The analytical heat transfer theory for spherical geometries with localized heat sources was developed. In addition a cylindrical theory was developed to assist the future efforts planned for the exploration of the laser refrigeration performance of NV center performance in cylindrical cavities.

In chapter 5, the H3 centers were also introduced and 10 times reduced heating was observed in a macroscopic diamond sample with high concentration of H3 centers compared to a sample with predominantly NV centers. In addition, anti-Stokes emission was observed from H3 centers. In the context of previous reports on H3 centers used for lasing[151], these experiments motivate further exploration of H3 centers for realization of radiation balanced lasers.

6.1 Future directions

In the many experiments with thermometry, I found DWF and ODMR thermometry methods to be the most reliable and convinient methods to use. The reliability arises firstly from the presence of existing foundational literature. Secondly, the fitting of DWF calibration data produces fundamental material parameters such as Debye temperature, electron-phonon coupling parameters. These parameters are not sensitive to many external conditions and

lead to temperature calibrations that are reliable even at varying conditions such as laser irradiances.

Optically detected magnetic resonance is another such method that can measure temperatures reliably. At present the ODMR system uses a proof-of-concept computer algorithm which produces a microwave source that varies in frequency continuously through an antenna. In my experiments, this has caused the broadening of the ODMR features and has been unreliable in measuring temperatures accurately. In addition, the proof-of-concept scheme also requires a high microwave power source, which adds more complications in the measurement. For the next iteration of this project, I recommend modifying the existing algorithm to the one that uses microwave pulses and records the APD signal during the pulse. This will help decrease the broadening and also increase the signal to noise ratio, enabling the use of much lower microwave powers to obtain more accurate temperature measurements.

The H3 defect in diamond was introduced as a candidate for the exploration of laser refrigeration in wide band gap materials. I foresee many challenges before laser refrigeration is achieved using this center. Firstly, the defect emits a large proportion of photons through phonon processes. This means that a large quantity of phonons are dumped into the system when photons red-shifted from the ZPL are emitted. As discussed previously, Purcell enhancement and other resonant cavities may be a few pathways to enhance the emission from the ZPL band as compared to the phonon side bands. Secondly, the present methods used for the synthesis of H3 defects naturally introduce a large percentage of other defects such as A-aggregates and NV centers. This is detrimental because the laser that is to be used for laser refrigeration will need to pump at wavelengths greater than 547 nm and will inevitably get absorbed by NV^0 ir NV^- centers. This is due to the large absorption of NV in this wavelength band compared to the absorption cross section of H3 which is several orders of magnitude smaller. Hence, the synthesis methods for exclusively producing H3 defects will need to be explored. Finally, in macroscopic samples, the high refractive index of diamond will cause emission trapping, hence reducing the extraction efficiency drastically. Therefore the use of smart photon extraction techniques will be required. This may also be addressed

by the use of nanodiamonds doped with H3 defects for exploring laser refrigeration. Before these larger goals are pursued, it is essential that more preliminary measurements be done on the H3 samples using a tunable laser source to evaluate the efficiency of the anti-Stokes process using the LITMOS test[161].

LIST OF PUBLICATIONS

- **A. Pant**, B. E. Smith, M. J. Crane, X. Zhou, M. B. Lim, S. A. Frazier, E. J. Davis, and P. J. Pauzauskie. "Optomechanical thermometry of nanoribbon cantilevers." *The Journal of Physical Chemistry C* **122.13** (2018): 7525-7532.

- X. Zhou, X. Xia, B. E. Smith, M. B. Lim, A. B. Bard, **A. Pant**, and P. J. Pauzauskie. "Interface-dependent radiative lifetimes of Yb^{3+}, Er^{3+} co-doped single $NaYF_4$ upconversion nanowires." *ACS applied materials & interfaces* **11.25** (2019): 22817-22823.

- **A. Pant***, Y. V. Morozov*, S. Zhang*, Boldizsár Jankó, S. D. Melgaard, D. A. Bender, P. J. Pauzauskie, and M. Kuno. *et al.* "Can lasers really refrigerate CdS nanobelts?." *Nature* **570.7762** (2019): E60-E61.

- **A. Pant**, E. J. Davis, and P. J. Pauzauskie."Photothermal heating of semiconductor nanoribbons." *The Journal of Physical Chemistry C* **123.47** (2019): 28941-28947.

- X. Xia, **A. Pant**, E. J. Davis, and P. J. Pauzauskie. "Design of a radiation-balanced fiber laser via optically active composite cladding materials." *Journal of the Optical Society of America B* **36.12** (2019): 3307-3314.

- X. Xia, **A. Pant**, X. Zhou, E. A. Dobretsova, A. B. Bard, M. B. Lim, J. Y. D. Roh, D. R. Gamelin, and P. J. Pauzauskie. "Hydrothermal synthesis and solid-state laser refrigeration of ytterbium-doped potassium lutetium fluoride (KLF) microcrystals." *ChemRxiv* (2020).

- **A. Pant**, X. Xia, E. J. Davis, and P. J. Pauzauskie. "Solid-state laser refrigeration

of a composite semiconductor Yb:$YLiF_4$ optomechanical resonator." *Nature Communications* **11.1** (2020): 1-7.

- A. S. Ganas, E. A. Dobretsova, **A. Pant**, B. Journaux, X. Xia, R. G. Felsted, and P. J. Pauzauskie. "Solid-state laser refrigeration at GPa pressures." *ChemRxiv* (2020).

- **A. Pant**, R. G. Felsted, A. B. Bard, X. Xia, S. Dadras, K. Shayan, D. R. Luntz-Martin, D. Mannikko, I. M. Pavlovetc, S. Stoll, M Kuno, A. N. Vamivakas, and P. J. Pauzauskie. "Solid-state laser refrigeration of nanodiamond quantum sensors. *arXiv preprint* arXiv:2007.15247 (2020).

- X. Xia, **A. Pant**, A. S. Ganas, F. Jelezko, and P. J. Pauzauskie. "Quantum point defects for solid state laser refrigeration." *Advanced Materials* (2020): 1905406.

- **A. Pant**, X. Xia, E. J. Davis, and P. J. Pauzauskie. "Anti-Stokes laser refrigeration of a nanoscale semiconductor gain medium." In *Photonic Heat Engines: Science and Applications*, vol. 10936, p. 1093606 (International Society for Optics and Photonics, 2019).

- X. Xia, **A. Pant**, E. J. Davis, and P. J. Pauzauskie. "Laser refrigeration of optical fibers via optically-active composite cladding materials." In *Photonic Heat Engines: Science and Applications*, vol. 10936, p. 109360I (International Society for Optics and Photonics, 2019).

- X. Xia, G. Felsted, **A. Pant**, E. Dobretsova, and P. J. Pauzauskie. "Laser refrigeration of ytterbium-doped alkali-yttrium-fluoride nanostructures (Yb:MYF, M = K, Na, Li)." In *Biophotonics Congress: Optics in the Life Sciences Congress 2019*, pp. AW4E-2. (Optical Society of America, 2019).

---

* *Indicates equal contribution*

BIBLIOGRAPHY

[1] Zhang, J., Li, D., Chen, R. & Xiong, Q. Laser cooling of a semiconductor by 40 Kelvin. *Nature* **493**, 504–508 (2013).

[2] Pant, A. *et al.* Optomechanical thermometry of nanoribbon cantilevers. *J. Phys. Chem. C* **122**, 7525–7532 (2018).

[3] Dougherty, T. J. *et al.* Photodynamic therapy. *J. Natl. Cancer Inst.* **90**, 889–905 (1998).

[4] Xiao, J.-D. & Jiang, H.-L. Metal–organic frameworks for photocatalysis and photothermal catalysis. *Acc. Chem. Res.* **52**, 356–366 (2018).

[5] Politano, A. *et al.* Photothermal membrane distillation for seawater desalination. *Adv. Mater.* **29**, 1603504 (2017).

[6] Ashkin, A. Optical trapping and manipulation of neutral particles using lasers. *Proc. Natl. Acad. Sci. U.S.A* **94**, 4853–4860 (1997).

[7] Rahman, A. *et al.* Burning and graphitization of optically levitated nanodiamonds in vacuum. *Sci. Rep.* **6**, 21633 (2016).

[8] Sheik-Bahae, M. & Epstein, R. *Optical Refrigeration: science and applications of laser cooling of solids* (Wiley-VCH, Weinheim, Germany, 2009).

[9] Pringsheim, P. Two observations about the difference between luminescence and thermal radiation. *Z. Phys.* **57**, 739–746 (1929).

[10] Epstein, R. I., Buchwald, M. I., Edwards, B. C., Gosnell, T. R. & Mungan, C. E. Observation of laser-induced fluorescent cooling of a solid. *Nature* **377**, 500 (1995).

[11] Fernandez, J., Mendioroz, A., Garcia, A., Balda, R. & Adam, J. Anti-stokes laser-induced internal cooling of yb 3+-doped glasses. *Phys. Rev. B* **62**, 3213 (2000).

[12] Thiede, J., Distel, J., Greenfield, S. & Epstein, R. Cooling to 208 K by optical refrigeration. *Appl. Phys. Lett.* **86**, 154107 (2005).

[13] Melgaard, S. D., Albrecht, A. R., Hehlen, M. P. & Sheik-Bahae, M. Solid-state optical refrigeration to sub-100 Kelvin regime. *Scientific reports* **6**, 1–6 (2016).

[14] Epstein, R. I., Brown, J., Edwards, B. C. & Gibbs, A. Measurements of optical refrigeration in ytterbium-doped crystals. *J. Appl. Phys.* **90**, 4815–4819 (2001).

[15] Mendioroz, A. *et al.* Anti-stokes laser cooling in yb 3+-doped kpb 2 cl 5 crystal. *Opt. Lett.* **27**, 1525–1527 (2002).

[16] Bigotta, S. *et al.* Laser cooling of Yb^{3+}-doped BaY_2F_8 single crystal. *Opt. Mater.* **28**, 1321–1324 (2006).

[17] Zhong, B. *et al.* Laser cooling of Yb^{3+}-doped $LuLiF_4$ crystal. *Opt. Lett.* **39**, 2747–2750 (2014).

[18] Volpi, A., Cittadino, G., Di Lieto, A. & Tonelli, M. Anti-Stokes cooling of Yb-doped KYF_4 single crystals. *Journal of Luminescence* **203**, 670–675 (2018).

[19] Roder, P. B., Smith, B. E., Zhou, X., Crane, M. J. & Pauzauskie, P. J. Laser refrigeration of hydrothermal nanocrystals in physiological media. *Proc. Natl. Acad. Sci. U. S. A.* **112**, 15024–15029 (2015).

[20] Einstein, A. On the motion required by the molecular kinetic theory of heat of small particles suspended in a stationary liquid. *Ann. Phys.* **17**, 549–560 (1905).

[21] Hehlen, M. P. *et al.* First demonstration of an all-solid-state optical cryocooler. *Light: Sci. Appl.* **7**, 15 (2018).

[22] Kessler, T. *et al.* A sub-40-mHz-linewidth laser based on a silicon single-crystal optical cavity. *Nat. Photonics* **6**, 687 (2012).

[23] Zhou, X., Smith, B. E., Roder, P. B. & Pauzauskie, P. J. Laser refrigeration of ytterbium-doped sodium–yttrium–fluoride nanowires. *Adv. Mater.* **28**, 8658–8662 (2016).

[24] Vicente, R. *et al.* Impacts of laser cooling for low earth orbit observation satellites: An analysis in terms of size, weight and power. *Cryogenics* **105**, 103000 (2020).

[25] Bowman, S. R. Lasers without internal heat generation. *IEEE J. Quantum Electron.* **35**, 115–122 (1999).

[26] Nemova, G. & Kashyap, R. Laser cooling of solids: latest achievements and prospects. In *Optical and Electronic Cooling of Solids III*, vol. 10550, 1055005 (International Society for Optics and Photonics, 2018).

[27] Landau, L. *et al.* On the thermodynamics of photoluminescence. *J. Phys.(Moscow)* **10** (1946).

[28] Sugiyama, A., Katsurayama, M., Anzai, Y. & Tsuboi, T. Spectroscopic properties of Yb doped YLF grown by a vertical bridgman method. *J. Alloys Compd.* **408**, 780–783 (2006).

[29] Sheik-Bahae, M. & Epstein, R. I. Optical refrigeration. *Nat. Photonics* **1**, 693–699 (2007).

[30] Sheik-Bahae, M. & Epstein, R. I. Laser cooling of solids. *Laser Photonics Rev.* **3**, 67–84 (2009).

[31] Seletskiy, D. V. *et al.* Local laser cooling of Yb: YLF to 110 K. *Opt. Express* **19**, 18229–18236 (2011).

[32] Gragossian, A. *et al.* Investigation of temperature dependence of quantum efficiency and parasitic absorption in rare-earth doped crystals (conference presentation). In *Optical and Electronic Cooling of Solids III*, vol. 10550, 1055006 (International Society for Optics and Photonics, 2018).

[33] Volpi, A. *et al.* Optical refrigeration: the role of parasitic absorption at cryogenic temperatures. *Opt. Express* **27**, 29710–29718 (2019).

[34] Khurgin, J. B. Role of bandtail states in laser cooling of semiconductors. *Phys. Rev. B* **77**, 235206 (2008).

[35] Kastler, A. Quelques suggestions concernant la production optique et la détection optique d'une inégalité de population des niveaux de quantifigation spatiale des atomes. application à l'expérience de stern et gerlach et à la résonance magnétique. *J. phys. radium* **11**, 255–265 (1950).

[36] Fernandez, J., Garcia-Adeva, A. J. & Balda, R. Anti-Stokes laser cooling in bulk erbium-doped materials. *Phys. Rev. Lett.* **97**, 033001 (2006).

[37] O'Connell, A. D. *et al.* Quantum ground state and single-phonon control of a mechanical resonator. *Nature* **464**, 697–703 (2010).

[38] Teufel, J. *et al.* Sideband cooling of micromechanical motion to the quantum ground state. *Nature* **475**, 359–363 (2011).

[39] Gröblacher, S. *et al.* Demonstration of an ultracold micro-optomechanical oscillator in a cryogenic cavity. *Nat. Phys.* **5**, 485–488 (2009).

[40] Park, Y.-S. & Wang, H. Resolved-sideband and cryogenic cooling of an optomechanical resonator. *Nat. Phys.* **5**, 489–493 (2009).

[41] Chan, J. *et al.* Laser cooling of a nanomechanical oscillator into its quantum ground state. *Nature* **478**, 89–92 (2011).

[42] Lemos, A. M. *Huang-Rhys factors for absorption and emission of light by F-centers.* Ph.D. thesis, Illinois institute of technology, Chicago, IL (1964).

[43] Li, D., Zhang, J. & Xiong, Q. Laser cooling of CdS nanobelts: thickness matters. *Opt. Express* **21**, 19302–19310 (2013).

[44] Agarwal, R., Barrelet, C. J. & Lieber, C. M. Lasing in single cadmium sulfide nanowire optical cavities. *Nano Lett.* **5**, 917–920 (2005).

[45] Liu, B. *et al.* Exciton-related photoluminescence and lasing in CdS nanobelts. *J. Phys. Chem. C* **115**, 12826–12830 (2011).

[46] Nasalevich, M. A., Kozlova, E. A., Lyubina, T. P. & Vorontsov, A. V. Photocatalytic oxidation of ethanol and isopropanol vapors on cadmium sulfide. *J. Catal.* **287**, 138–148 (2012).

[47] Peng, T., Li, K., Zeng, P., Zhang, Q. & Zhang, X. Enhanced photocatalytic hydrogen production over graphene oxide–cadmium sulfide nanocomposite under visible light irradiation. *J. Phys. Chem. C* **116**, 22720–22726 (2012).

[48] Thomas, D. & Hopfield, J. Exciton spectrum of cadmium sulfide. *Phys. Rev.* **116**, 573–582 (1959).

[49] Fröhlich, H. Interaction of electrons with lattice vibrations. *Proc. R. Soc. London, Ser. A* **66**, 291–298 (1952).

[50] Morozov, Y. V. *et al.* Can lasers really refrigerate CdS nanobelts? *Nature* **570**, E60–E61 (2019).

[51] Gauck, H., Gfroerer, T., Renn, M., Cornell, E. A. & Bertness, K. A. External radiative quantum efficiency of 96% from a GaAs/GaInP heterostructure. *Appl. Phys. A* **64**, 143–147 (1997).

[52] Sheik-Bahae, M. & Epstein, R. I. Can laser light cool semiconductors? *Phys. Rev. Lett.* **92**, 247403 (2004).

[53] Hanifi, D. A. *et al.* Redefining near-unity luminescence in quantum dots with photothermal threshold quantum yield. *Science* **363**, 1199–1202 (2019).

[54] Fontenot, R. S., Mathur, V. K., Barkyoumb, J. H., Mungan, C. E. & Tran, T. N. Measuring the anti-stokes luminescence of cdse/zns quantum dots for laser cooling applications. In *Tri-Technology Device Refrigeration (TTDR)*, vol. 9821, 982103 (International Society for Optics and Photonics, 2016).

[55] Fontenot, R., Barkyoumb, J. & Mathur, V. Optical cooling of CdSe/ZnS quantum dots embedded in PMMA. *ECS Trans.* **80**, 1483 (2017).

[56] Zhang, S., Zhukovskyi, M., Jankó, B. & Kuno, M. Progress in laser cooling semiconductor nanocrystals and nanostructures. *NPG Asia Mater.* **11**, 1–19 (2019).

[57] Kern, M. *et al.* Optical cryocooling of diamond. *Phys. Rev. B* **95**, 235306 (2017).

[58] Nia, I. H. *et al.* Efficient luminescence extraction strategies and anti-reflective coatings to enhance optical refrigeration of semiconductors. *J. Lumin.* **170**, 841–854 (2016).

[59] Seletskiy, D. V. *et al.* Precise determination of minimum achievable temperature for solid-state optical refrigeration. *J. Lumin.* **133**, 5–9 (2013).

[60] McLaurin, E. J., Bradshaw, L. R. & Gamelin, D. R. Dual-emitting nanoscale temperature sensors. *Chem. Mater.* **25**, 1283–1292 (2013).

[61] Dong, B. *et al.* Size dependence of the upconverted luminescence of $NaYF_4$: Er, Yb microspheres for use in ratiometric thermometry. *Phys. Chem. Chem. Phys.* **16**, 20009–20012 (2014).

[62] Seletskiy, D. V., Hasselbeck, M. P., Sheik-Bahae, M. & Epstein, R. I. *Fast differential luminescence thermometry.* In *Proc. SPIE 7228, Laser Refrigeration of Solids II, 72280K, San Jose, California, United States, Feb 10, 2009*, vol. 7228 (2009).

[63] Imangholi, B. *et al.* Differential luminescence thermometry in semiconductor laser cooling. In *Physics and Simulation of Optoelectronic Devices XIV*, vol. 6115, 61151C (International Society for Optics and Photonics, 2006).

[64] Grattan, K. & Zhang, Z. Fiber optic fluorescence thermometry. In *Topics in Fluorescence Spectroscopy*, 335–376 (Springer, 2002).

[65] Patterson, W., Seletskiy, D., Sheik-Bahae, M., Epstein, R. & Hehlen, M. Measurement of solid-state optical refrigeration by two-band differential luminescence thermometry. *J. Opt. Soc. Am. B* **27**, 611–618 (2010).

[66] Ha, S.-T., Shen, C., Zhang, J. & Xiong, Q. Laser cooling of organic-inorganic lead halide perovskites. *Nat. Photonics* **10**, 115–121 (2016).

[67] Manzke, G. *et al.* Density dependence of the exciton energy in semiconductors. *Phys. Rev. Lett.* **80**, 4943 (1998).

[68] Smith, B. E. *Thermochemical dynamics of laser-irradiated semiconductor nanostructures.* Ph.D. thesis, University of Washington Libraries (2016).

[69] Hartland, G. V., Hu, M. & Sader, J. E. Softening of the symmetric breathing mode in gold particles by laser-induced heating. *J. Phys. Chem. B* **107**, 7472–7478 (2003).

[70] Major, T. A., Lo, S. S., Yu, K. & Hartland, G. V. Time-resolved studies of the acoustic vibrational modes of metal and semiconductor nano-objects. *J. Phys. Chem. Lett.* **5**, 866–874 (2014).

[71] Ashkin, A., Dziedzic, J. M., Bjorkholm, J. & Chu, S. Observation of a single-beam gradient force optical trap for dielectric particles. *Opt. Lett.* **11**, 288–290 (1986).

[72] Sandberg, R., Svendsen, W., Mølhave, K. & Boisen, A. Temperature and pressure dependence of resonance in multi-layer microcantilevers. *J. Micromech. Microeng.* **15**, 1454–1458 (2005).

[73] Bauchau, O. & Craig, J. Euler-Bernoulli beam theory. In *Structural analysis*, 173–221 (Springer: Dordrecht, Netherlands, 2009).

[74] Balachandran, B. & Magrab, E. B. *Vibrations* (Cengage Learning: Toronto, Canada, 2008).

[75] Rahman, A. A. & Barker, P. Laser refrigeration, alignment and rotation of levitated Yb^{3+}: YLF nanocrystals. *Nat. Photonics* **11**, 634 (2017).

[76] Lei, G., Anderson, J., Buchwald, M., Edwards, B. & Epstein, R. Determination of spectral linewidths by Voigt profiles in Yb^{3+}-doped fluorozirconate glasses. *Phys. Rev. B* **57**, 7673 (1998).

[77] Tanner, M. G., Dyer, S. D., Baek, B., Hadfield, R. H. & Woo Nam, S. High-resolution single-mode fiber-optic distributed Raman sensor for absolute temperature measurement using superconducting nanowire single-photon detectors. *Appl. Phys. Lett.* **99**, 201110 (2011).

[78] Plakhotnik, T., Doherty, M. W., Cole, J. H., Chapman, R. & Manson, N. B. All-optical thermometry and thermal properties of the optically detected spin resonances of the NV^--center in nanodiamond. *Nano Lett.* **14**, 4989–4996 (2014).

[79] Pant, A. *et al.* Solid-state laser refrigeration of nanodiamond quantum sensors. *arXiv preprint arXiv:2007.15247* (2020).

[80] Brand, J., Weinzierl, G. & Friedrich, J. Single-mode electron-phonon coupling and optical lineshape analysis on a naphthalene x trap system. *Chem. Phys. Lett.* **84**, 197–200 (1981).

[81] Balasubramanian, G. *et al.* Nanoscale imaging magnetometry with diamond spins under ambient conditions. *Nature* **455**, 648–651 (2008).

[82] Toyli, D. *et al.* Measurement and control of single nitrogen-vacancy center spins above 600 K. *Phys. Rev. X* **2**, 031001 (2012).

[83] Doherty, M. W. *et al.* Electronic properties and metrology applications of the diamond NV^- center under pressure. *Phys. Rev. Lett.* **112**, 047601 (2014).

[84] Jin, L. *et al.* Twinning mediated growth of ZnSe tri and bi-crystal nanobelts with single crystalline wurtzite nanobelts as building blocks. *CrystEngComm* **12**, 150–158 (2010).

[85] Morozov, Y. V. *et al.* Defect-mediated CdS nanobelt photoluminescence up-conversion. *J. Phys. Chem. C* **121**, 16607–16616 (2017).

[86] Tell, B., Damen, T. & Porto, S. Raman effect in cadmium sulfide. *Phys. Rev.* **144**, 771–774 (1966).

[87] Hu, C., Zeng, X., Cui, J., Chen, H. & Lu, J. Size effects of Raman and photoluminescence spectra of CdS nanobelts. *J. Phys. Chem. C* **117**, 20998–21005 (2013).

[88] Phuruangrat, A., Thongtem, T. & Thongtem, S. Characterization and photonic absorption of hierarchical tree-like CdS nanostructure synthesized by solvothermal method. *Mater. Lett.* **80**, 114–116 (2012).

[89] Chuu, D., Dai, C., Hsieh, W. & Tsai, C. Raman investigations of the surface modes of the crystallites in CdS thin films grown by pulsed laser and thermal evaporation. *J. Appl. Phys.* **69**, 8402–8404 (1991).

[90] Abdulkhadar, M. & Thomas, B. Study of Raman spectra of nanoparticles of CdS and ZnS. *Nanostruct. Mater.* **5**, 289–298 (1995).

[91] Johnson, B. Theory of morphology-dependent resonances: shape resonances and width formulas. *J. Opt. Soc. Am.* **10**, 343–352 (1993).

[92] Roder, P. B., Pauzauskie, P. J. & Davis, E. J. Nanowire heating by optical electromagnetic irradiation. *Langmuir* **28**, 16177–16185 (2012).

[93] *Comsol, version 4.2; COMSOL Inc.: Burlington, MA, 2011.*

[94] Gerlich, D. The elastic constants of cadmium sulfide between 4.2–300° K. *J. Phys. Chem. Solids* **28**, 2575–2579 (1967).

[95] Treharne, R. *et al.* Optical design and fabrication of fully sputtered CdTe/CdS solar cells. *J. Phys. Conf. Ser* **286**, 012038 (2011).

[96] Pant, A., Davis, E. J. & Pauzauskie, P. J. Photothermal heating of semiconductor nanoribbons. *J. Phys. Chem. C* **123**, 28941–28947 (2019).

[97] Zhang, Q. *et al.* Exciton-phonon coupling in individual ZnTe nanorods studied by resonant Raman spectroscopy. *Phys. Rev. B* **85**, 085418 (2012).

[98] Liu, H.-L. *et al.* Deep-ultraviolet Raman scattering spectroscopy of monolayer WS_2. *Sci. Rep.* **8**, 11398 (2018).

[99] Moore Jr, G. E. & Klein, M. V. Thermal conductivity of doped and pure cadmium sulfide. *Phys. Rev.* **179**, 722 (1969).

[100] Guajardo-Cuéllar, A., Go, D. B. & Sen, M. Evaluation of heat current formulations for equilibrium molecular dynamics calculations of thermal conductivity. *J. Chem. Phys.* **132**, 104111 (2010).

[101] Che, J., Çağın, T., Deng, W. & Goddard III, W. A. Thermal conductivity of diamond and related materials from molecular dynamics simulations. *J. Chem. Phys.* **113**, 6888–6900 (2000).

[102] Jeong, C., Datta, S. & Lundstrom, M. Thermal conductivity of bulk and thin-film silicon: a Landauer approach. *J. Appl. Phys.* **111**, 093708 (2012).

[103] Liu, X. *et al.* Thermal conductivity measurement of individual CdS nanowires using microphotoluminescence spectroscopy. *J. Appl. Phys.* **108**, 054310 (2010).

[104] Liang, L. & Li, B. Size-dependent thermal conductivity of nanoscale semiconducting systems. *Phys. Rev. B* **73**, 153303 (2006).

[105] Lyeo, H.-K. & Cahill, D. G. Thermal conductance of interfaces between highly dissimilar materials. *Phys. Rev. B* **73**, 144301 (2006).

[106] Meyer, G. A simple low-temperature ultrahigh-vacuum scanning tunneling microscope capable of atomic manipulation. *Rev. Sci. Instrum.* **67**, 2960–2965 (1996).

[107] Kirk, M., Albrecht, T. & Quate, C. Low-temperature atomic force microscopy. *Rev. Sci. Instrum.* **59**, 833–835 (1988).

[108] Hosseini, M., Guccione, G., Slatyer, H. J., Buchler, B. C. & Lam, P. K. Multimode laser cooling and ultra-high sensitivity force sensing with nanowires. *Nat. Commun.* **5**, 4663 (2014).

[109] Chang, D. E. *et al.* Cavity opto-mechanics using an optically levitated nanosphere. *Proc. Natl. Acad. Sci. U. S. A.* **107**, 1005–1010 (2010).

[110] Delić, U. *et al.* Cooling of a levitated nanoparticle to the motional quantum ground state. *Science* **367**, 892–895 (2020).

[111] Li, Y. *et al.* Room-temperature continuous-wave lasing from monolayer molybdenum ditelluride integrated with a silicon nanobeam cavity. *Nat. Nanotechnol.* **12**, 987–992 (2017).

[112] García-Meca, C. *et al.* On-chip wireless silicon photonics: from reconfigurable interconnects to lab-on-chip devices. *Light: Sci. Appl.* **6**, e17053 (2017).

[113] Atatüre, M., Englund, D., Vamivakas, N., Lee, S.-Y. & Wrachtrup, J. Material platforms for spin-based photonic quantum technologies. *Nat. Rev. Mater.* **3**, 38–51 (2018).

[114] Jensen, K., Kim, K. & Zettl, A. An atomic-resolution nanomechanical mass sensor. *Nat. Nanotechnol.* **3**, 533–537 (2008).

[115] Braginskii, V. B. & Manukin, A. B. *Measurement of weak forces in physics experiments* (University of Chicago Press, 1977).

[116] Abramovici, A. *et al.* LIGO: The laser interferometer gravitational-wave observatory. *Science* **256**, 325–333 (1992).

[117] Schwab, K. C. & Roukes, M. L. Putting mechanics into quantum mechanics. *Phys. Today* **58**, 36–42 (2005).

[118] Kolkowitz, S. *et al.* Coherent sensing of a mechanical resonator with a single-spin qubit. *Science* **335**, 1603–1606 (2012).

[119] Bowman, S. R., O'Connor, S. R. & Biswal, S. Ytterbium laser with reduced thermal loading. *IEEE J. Quantum Electron.* **41**, 1510–1517 (2005).

[120] Lee, J., Goericke, F. & King, W. P. Temperature-dependent thermomechanical noise spectra of doped silicon microcantilevers. *Sens. Actuators, A* **145**, 37–43 (2008).

[121] Pini, V. *et al.* Shedding light on axial stress effect on resonance frequencies of nanocantilevers. *ACS Nano* **5**, 4269–4275 (2011).

[122] Bensalah, A. *et al.* Growth of Yb^{3+}-doped $YLiF_4$ laser crystal by the Czochralski method. attempt of Yb^{3+} energy level assignment and estimation of the laser potentiality. *Opt. Mater.* **26**, 375–383 (2004).

[123] Reddy, B. & Venkateswarlu, P. Infrared to visible energy upconversion in Er^{3+}-doped oxide glass. *Appl. Phys. Lett.* **64**, 1327–1329 (1994).

[124] Yeh, D., Sibley, W., Schneider, I., Afzal, R. & Aggarwal, I. Intensity-dependent upconversion efficiencies of Er^{3+} ions in heavy-metal fluoride glass. *J. Appl. Phys.* **69**, 1648–1653 (1991).

[125] Acosta, V. M. *et al.* Temperature dependence of the nitrogen-vacancy magnetic resonance in diamond. *Phys. Rev. Lett.* **104**, 070801 (2010).

[126] Rondin, L. *et al.* Magnetometry with nitrogen-vacancy defects in diamond. *Rep. Prog. Phys.* **77**, 056503 (2014).

[127] Pelliccione, M. *et al.* Scanned probe imaging of nanoscale magnetism at cryogenic temperatures with a single-spin quantum sensor. *Nat. Nanotechnol.* **11**, 700–705 (2016).

[128] Schmitt, S. *et al.* Submillihertz magnetic spectroscopy performed with a nanoscale quantum sensor. *Science* **356**, 832–837 (2017).

[129] Kurtsiefer, C., Mayer, S., Zarda, P. & Weinfurter, H. Stable solid-state source of single photons. *Phys. Rev. Lett.* **85**, 290 (2000).

[130] Beveratos, A. *et al.* Room temperature stable single-photon source. *Eur. Phys. J. D* **18**, 191–196 (2002).

[131] Childress, L. & Hanson, R. Diamond NV centers for quantum computing and quantum networks. *MRS Bull.* **38**, 134–138 (2013).

[132] Nemoto, K. *et al.* Photonic quantum networks formed from NV^- centers. *Sci. Rep.* **6**, 26284 (2016).

[133] Seletskiy, D. V., Epstein, R. & Sheik-Bahae, M. Laser cooling in solids: advances and prospects. *Rep. Prog. Phys.* **79**, 096401 (2016).

[134] Schirhagl, R., Chang, K., Loretz, M. & Degen, C. L. Nitrogen-vacancy centers in diamond: nanoscale sensors for physics and biology. *Annu. Rev. Phys. Chem.* **65**, 83–105 (2014).

[135] Riedel, C. J. Direct detection of classically undetectable dark matter through quantum decoherence. *Phys. Rev. D* **88**, 116005 (2013).

[136] Albrecht, A., Retzker, A. & Plenio, M. B. Testing quantum gravity by nanodiamond interferometry with nitrogen-vacancy centers. *Phys. Rev. A* **90**, 033834 (2014).

[137] Arvanitaki, A. & Geraci, A. A. Detecting high-frequency gravitational waves with optically levitated sensors. *Phys. Rev. Lett.* **110**, 071105 (2013).

[138] Crane, M. J., Zhou, X., Davis, E. J. & Pauzauskie, P. J. Photothermal heating and cooling of nanostructures. *Chem. - Asian J.* **13**, 2575–2586 (2018).

[139] Stanwix, P. L. *et al.* Coherence of nitrogen-vacancy electronic spin ensembles in diamond. *Phys. Rev. B* **82**, 201201 (2010).

[140] Waldermann, F. *et al.* Creating diamond color centers for quantum optical applications. *Diamond Relat. Mater.* **16**, 1887–1895 (2007).

[141] Li, Z., Aleshire, K., Kuno, M. & Hartland, G. V. Super-resolution far-field infrared imaging by photothermal heterodyne imaging. *J. Phys. Chem. B* **121**, 8838–8846 (2017).

[142] Pettit, R. M., Neukirch, L. P., Zhang, Y. & Vamivakas, A. N. Coherent control of a single nitrogen-vacancy center spin in optically levitated nanodiamond. *J. Opt. Soc. Am. B* **34**, C31–C35 (2017).

[143] Chen, Y. *et al.* Deterministic positioning of colloidal quantum dots on silicon nitride nanobeam cavities. *Nano Lett.* **18**, 6404–6410 (2018).

[144] Fryett, T. K. *et al.* Encapsulated silicon nitride nanobeam cavity for hybrid nanophotonics. *ACS Photonics* **5**, 2176–2181 (2018).

[145] Rupper, G., Kwong, N.-H. & Binder, R. Large excitonic enhancement of optical refrigeration in semiconductors. *Phys. Rev. Lett.* **97**, 117401 (2006).

[146] Xu, Y. *et al.* Strong anti-Stokes luminescence from H^+-irradiated diamond. *Appl. Phys. Lett.* **83**, 1968–1970 (2003).

[147] Gao, Y.-F. *et al.* Phonon-assisted photoluminescence up-conversion of silicon-vacancy centers in diamond. *J. Phys. Chem. Lett.* **9**, 6656–6661 (2018).

[148] Tran, T. T. *et al.* Anti-Stokes excitation of solid-state quantum emitters for nanoscale thermometry. *Sci. Adv.* **5**, 9180 (2019).

[149] Wolf, S. A., Rosenberg, I., Rapaport, R. & Bar-Gill, N. Purcell-enhanced optical spin readout of nitrogen-vacancy centers in diamond. *Phys. Rev. B* **92**, 235410 (2015).

[150] Davies, P. & Fisher, M. Heat transfer from electrically heated cylinders. *Proc. R. Soc. A* **280**, 486–527 (1964).

[151] Rand, S. & DeShazer, L. Laser action of H3 color center in diamond. In *Tunable Solid State Lasers for Remote Sensing: Proceedings of the NASA Conference Stanford University, Stanford, USA, October 1–3, 1984*, vol. 51, 146 (Springer, 2013).

[152] Pinto, H. *et al.* On the diffusion of NV defects in diamond. *Phys. Status Solidi A* **209**, 1765–1768 (2012).

[153] Thomaz, M. & Davies, G. The decay time of N3 luminescence in natural diamond. *Proc. R. Soc. Lond. A* **362**, 405–419 (1978).

[154] Liaugaudas, G., Collins, A. T., Suhling, K., Davies, G. & Heintzmann, R. Luminescence-lifetime mapping in diamond. *J. Phys. Condens. Matter.* **21**, 364210 (2009).

[155] Diab, H. *et al.* Impact of reabsorption on the emission spectra and recombination dynamics of hybrid perovskite single crystals. *J. Phys. Chem. Lett.* **8**, 2977–2983 (2017).

[156] Collins, A., Thomaz, M. & Jorge, M. I. B. Luminescence decay time of the 1.945 eV centre in type Ib diamond. *J. Phys. C: Solid State Phys.* **16**, 2177 (1983).

[157] Batalov, A. *et al.* Temporal coherence of photons emitted by single nitrogen-vacancy defect centers in diamond using optical rabi-oscillations. *Phys. Rev. Lett.* **100**, 077401 (2008).

[158] Beha, K., Batalov, A., Manson, N. B., Bratschitsch, R. & Leitenstorfer, A. Optimum photoluminescence excitation and recharging cycle of single nitrogen-vacancy centers in ultrapure diamond. *Phys. Rev. Lett* **109**, 097404 (2012).

[159] Aslam, N., Waldherr, G., Neumann, P., Jelezko, F. & Wrachtrup, J. Photo-induced ionization dynamics of the nitrogen vacancy defect in diamond investigated by single-shot charge state detection. *New J. Phys.* **15**, 013064 (2013).

[160] Subedi, S. D. *et al.* Laser spectroscopic characterization of negatively charged nitrogen-vacancy (NV^-) centers in diamond. *Opt. Mater. Express* **9**, 2076–2087 (2019).

[161] Melgaard, S. D. *Cryogenic optical refrigeration: Laser cooling of solids below 123 K* (The University of New Mexico, 2013).

[162] Svelto, O. & Hanna, D. C. *Principles of lasers*, vol. 4 (Springer: New York, 1998).

Appendix A

HEAT TRANSFER

A.1 Heat transfer theory

The energy equation for this electromagnetically heated ribbon is given by

$$\rho\hat{C}\frac{\partial T}{\partial t} = \kappa\left(\frac{\partial^2 T}{\partial x^2} + \frac{\partial^2 T}{\partial y^2} + \frac{\partial^2 T}{\partial z^2}\right) + Q''', \tag{A.1}$$

in which ρ is the nanoribbon density, $\hat{C}$ is its specific heat, κ is its thermal conductivity, and Q''' is the rate of heat generated per unit volume, which is related to the electric field vector, $\mathbf{E}$, of the laser beam by

$$Q''' = \frac{2\pi n' n''}{\lambda_0 Z_0}(\mathbf{E}\cdot\mathbf{E}^*). \tag{A.2}$$

Here $n = n' - in''$ is the complex refractive index of the medium, λ_0 is the wavelength *in vacuo*, Z_0 is the free space impedance ($Z_0 = 376.73$ ohms), and $\mathbf{E}^*$ is the complex conjugate of the electric field vector. For CdS at a wavelength of 532 nm, $n = 2.5513 - i0.0057657$ [95]. The small imaginary component of the refractive index indicates weak absorption of the electromagnetic radiation.

We assume that the Gaussian beam impinges on the nanoribbon on its centerline with the beam located at axial position $y = L_0$ and its beam waist, w_0, located at the surface of the nanoribbon ($z = 0$). For a weakly convergent beam polarized in the x-direction and propagating in the z-direction through a thin slab the electric vector of the beam can be approximated by[162]:

$$\mathbf{E}(r,z) = \hat{x}E_0 \exp\left(-\frac{r^2}{w_0^2}\right)\exp(-ikz), \tag{A.3}$$

in which $\hat{x}$ is the unit vector in the x-direction, E_0 is the electric field amplitude at $r = 0$, r is the radial distance from the center of the beam, and w_0 is the beam waist radius. The

wavenumber, k, is, in general, complex and is defined by

$$k = k' - ik'' = \frac{2\pi}{\lambda_0}(n' - in''), \tag{A.4}$$

The incident irradiance, I_0, equals the time-averaged magnitude of the Poynting vector, $\langle S \rangle$, where the Poynting vector is defined by

$$\mathbf{S} = \mathbf{E} \times \mathbf{H}^*, \tag{A.5}$$

and $\mathbf{H}^*$ is the complex conjugate of the magnetic vector, $\mathbf{H}$, given by

$$\mathbf{H}(r, z) = \hat{y}\frac{1}{Z_0}E_x(r, z), \tag{A.6}$$

in which $\hat{y}$ is the unit vector in the y-direction, and Z_0 is the impedance in vacuum. The incident irradiance is related to the total power of the beam, P_0, by

$$P_0 = \frac{1}{2}\pi I_0 w_0^2. \tag{A.7}$$

Using these results, the irradiance transmitted to the nanoribbon is given by

$$I(r, z) = I_0 \frac{(1 - R_\lambda)}{(1 - R_\lambda \exp(-2k''H))} \exp\left(- \frac{2r^2}{w_0^2} \right) \exp(-2k''z), \tag{A.8}$$

in which R_λ is the wavelength-dependent reflectivity of the beam and the $1/(1 - R_\lambda \exp(-2k''H))$ term takes into account multiple internal reflections within the CdSNR. Substituting in the energy equation and applying orthogonality of eigenfunctions, we obtain the following differential equation

$$\frac{dA_{lmn}(\tau')}{d\tau} + \gamma_{lmn}^2 A_{lmn}(\tau') = \int_0^1 \int_0^1 \int_0^1 \sigma(\xi'\eta'\zeta') X_l(\xi') Y_m(\eta') Z_n(\zeta') d\xi' d\eta' d\zeta'. \tag{A.9}$$

The solution for the coefficients $A_{lmn}(\tau)$ can be obtained by applying an integrating factor, and the steady state solution is obtained by taking the limit as $\tau \to \infty$ to give

$$A_{lmn} = \frac{1}{\gamma_{lmn}^2} \int_0^1 \int_0^1 \int_0^1 \sigma(\xi'\eta'\zeta') X_l(\xi') Y_m(\eta') Z_n(\zeta') d\xi' d\eta' d\zeta'. \tag{A.10}$$

A.2 Electrical conductivity for an electromagnetic heat source

In an electrical circuit the power (P) is equal to the current (I) multiplied by voltage (V). Then, the rate of heat generated per unit volume (L) is given as:

$$L = j \cdot E = (\sigma E) \cdot E, \tag{A.11}$$

where σ, j and E are the electrical conductivity, current density and electric field, respectively.

In ideal dielectrics there is no direct current, only displacement currents $j(\omega) = \epsilon(\omega) \cdot dE/dt$ may occur for alternating voltages or electrical fields. Here $\epsilon(\omega)$ is frequency dependent dielectric function. We thus have

$$j(\omega) = \epsilon(\omega) \cdot \frac{d[E_0 e^{i\omega t}]}{dt} = \epsilon(\omega) \cdot i \cdot \omega \cdot E_0 e^{i\omega t} = \epsilon(\omega) \cdot i \cdot \omega \cdot E(\omega). \tag{A.12}$$

For a complex dielectric function, $\epsilon(\omega) = \epsilon'(\omega) + i\epsilon''(\omega)$, the current density can be written as

$$j(\omega) = \omega \cdot \epsilon'' \cdot E(\omega) + i \cdot \omega \cdot \epsilon' \cdot E(\omega). \tag{A.13}$$

Equating the real parts of Eq. A.11 and A.13, the rate of heat generation per unit volume (L) can be written as

$$L = (\epsilon'' \omega E) \cdot E = (\epsilon'' \frac{2\pi}{\lambda_0} E) \cdot E, \tag{A.14}$$

where λ_0 is the wavelength of light. Since the complex dielectric function is the square of the complex refractive index ($n' + in''$), by equating the imaginary parts we can rewrite Eq. A.14 as

$$L = (2n'n'')\left(\frac{2\pi}{\lambda_0}\right) E \cdot E. \tag{A.15}$$

Therefore, the conductivity (σ) can be written in terms of the refractive index as

$$\sigma = \left(\frac{4\pi n'n''}{\lambda_0}\right) \tag{A.16}$$

A.3 The double quadrature

The double integral defined by

$$I_{lm} = \frac{2L^2k''}{\kappa T_0} I_0 \int_0^1 \int_0^1 \exp\left(\frac{-2r'^2}{w_0^2}\right) X_l(\xi')Y_m(\eta')d\xi' d\eta', \tag{A.17}$$

is zero for sufficiently large value of r. For example, the exponential term decreases to 1% of its value at the origin for $r = 1.5174w_0$ unless this value exceeds $W/2$. Consequently, the maximum value of r may be taken to be $W/2$. It is convenient to carry out the integration in cylindrical coordinates. Thus,

$$I_{lm} = \frac{4Lk''}{W\kappa T_0} I_0 \int_0^{\pi} \int_0^{W/2} \exp\left(\frac{-2r'^2}{w_0^2}\right) X_l(\xi')Y_m(\eta')rdr'd\theta', \tag{A.18}$$

in which

$$\xi' = \frac{1}{2} + \frac{r'}{W}\sin\theta', \eta' = \frac{L_0 - r\cos\theta'}{L}. \tag{A.19}$$

Letting $u' = 2(r'/w_0)^2$ and $r' = w_0(u'/2)^{1/2}$ in Eqs. (A.18 and A.19) the double integral transforms to

$$I_{lm} = \frac{w_0^2 Lk''}{W\kappa T_0} I_0 \int_0^{\pi} \int_0^{W^2/2w_0^2} \exp(-u') X_l(\xi')Y_m(\eta')du'd\theta', \tag{A.20}$$

where

$$\xi' = \frac{1}{2} + \frac{w_0}{W}\sqrt{\frac{u'}{2}}\sin\theta', \eta' = \frac{L_0}{L} - \frac{w_0}{L}\sqrt{\frac{u'}{2}}\cos\theta'. \tag{A.21}$$

The double integral was evaluated using python.

A.4 Analytical to Numerical with Python - Cylinder

```
import numpy as np
import pandas as pd
from scipy.special import jn as jv
from math import factorial
import matplotlib.pyplot as plt
from numpy import pi, sin, cos, sqrt
from mpl_toolkits.mplot3d import axes3d
```

```
from matplotlib import cm
%matplotlib inline
plt.rcParams['figure.figsize'] = [15, 5]

L = 10e-6
Rmax = 10e-6

meshR = 50
meshTheta = 50
meshZ = 50

r = np.linspace(0,Rmax,meshR)
xi = r/Rmax
theta = np.linspace(0,np.pi,meshTheta)
z = np.linspace(0,L,meshZ)
zeta = z/L

t = 1                    # Time in seconds
Tinf = 298

kappa = 2100
rho = 4860
C = 630

global Bi
kf = 0.024
Bi = kf/kappa
Bic = 0.34*(kf/kappa)
delx = 1000e-6
Bif = (L/delx)*(kf/kappa)
#Bi = 10000

tau = (kappa*t)/(rho*C*L**2)
```

```
41
42 def Xfunc(mu,m,xi):
43     return jv(m,mu*xi)
44
45 def Xeigfunc(xm,m):
46     return xm*(jv(m-1,xm)) - (m-Bic)*jv(m,xm)
47
48 def Yfunc(m,theta):
49     return cos(m*theta)
50
51 def Ynormfunc(m,intyx):
52     if m==0:
53         intyy = Yfunc(m,intyx)**2
54         integ = 2*np.trapz(intyy,intyx)
55         return 2*pi
56     else:
57         intyy = Yfunc(m,intyx)**2
58         integ = np.trapz(intyy,intyx)
59         return pi
60
61
62 def Zfunc(omega,zeta):
63     return sin(omega*zeta)
64
65 def Zeigfunc(xm):
66     return xm*np.cos(xm)+Bif*np.sin(xm)
67
68 def Znormfunc(n,intzx):
69     intzy = Zfunc(omega[n],intzx)**2
70     integ = np.trapz(intzy,intzx)
71     return integ
72
```

```
# Finds the roots of a function y(x). Takes in x and y arrays of the
    eigenfunction.
def rootfinder(xm,ym):
    eigL = 1000
    eigM = 1000
    lam = np.zeros(eigM)
    count = 0
    for j in range(0,len(ym)-1):
        if np.sign(ym[j]) != np.sign(ym[j+1]):
            xm1, xm2, ym1, ym2 = xm[j], xm[j+1], ym[j], ym[j+1]
            m = (ym2-ym1)/(xm2-xm1)
            lam[count] = (-ym1+(m*xm1))/m
            count = count+1
    lam = np.trim_zeros(lam)
    lam = [s for s in lam if str(s) != 'nan']

    #plt.plot(xm, ym)
    #plt.xlim(0,0.001)
    #plt.title("X-eigenvalue function")
    #plt.scatter(lam, np.zeros(np.size(lam)), color='red')
    #plt.show()

    return lam

numl = 20
numm = 20
numn = 20

xm = np.linspace(0,numn*10,100000)
omega = rootfinder(xm,Zeigfunc(xm))[0:numn]
print(omega)

xm = np.linspace(0,numl*10,100000)
```

```
105 mu = np.zeros((numl,numm))
106 for mm in range(0,numm):
107     mu[:,mm] = rootfinder(xm,Xeigfunc(xm,mm))[0:numl]
108     print("Mu_l for m={}".format(mm), mu[:,mm])
109 #print("\nMu size: ", np.shape(mu))
110 
111 plt.rcParams['figure.figsize'] = [7, 5]
112 
113 XFUNC = np.zeros((numl,numm,len(xi)))
114 for l in range(0,numl):
115     for m in range(0,numm):
116         XFUNC[l,m,:] = Xfunc(mu[l,m],m,xi)
117 
118 m=0
119 for l in range(0,numl):
120     plt.plot(xi,XFUNC[l,m,:], label="l={}".format(l))
121 #plt.legend()
122 plt.title("X-eigenfunction for l={}".format(l))
123 plt.show()
124 
125 def normXfunc(mu,omega,xi):
126     XintY = xi*Xfunc(mu,omega,xi)**2
127     normXi = np.trapz(XintY,xi)
128     return normXi
129 
130 normX = np.zeros((numl,numm))
131 for l in range(0,numl):
132     for m in range(0,numm):
133         normX[l] = normXfunc(mu[l,m],m,xi)
134 #print(normX)
135 
136 m=0
137 for l in range(0,5):
```

```
138     plt.plot(xi,XFUNC[l,m,:]/normX[l,m], label="l={}".format(l))
139 #plt.legend()
140 plt.title("Normalized X-eigenfunction for l={}".format(l))
141 plt.show()
142 
143 plt.rcParams['figure.figsize'] = [15, 5]
144 
145 YFUNC = np.zeros((numm,len(theta)))
146 for m in range(0,numm):
147     YFUNC[m,:] = Yfunc(m,theta)
148 
149 for m in range(0,numm):
150     plt.plot(theta,YFUNC[m,:]/Ynormfunc(m,theta),label="m={}".format(m))
151 #plt.legend()
152 plt.title("Y-eigenfunction")
153 plt.show()
154 
155 plt.rcParams['figure.figsize'] = [15, 5]
156 
157 ZFUNC = np.zeros((numn,len(zeta)))
158 for n in range(0,numn):
159     ZFUNC[n,:] = Zfunc(omega[n],zeta)
160 
161 for n in range(0,numn):
162     plt.plot(zeta,ZFUNC[n,:]/Znormfunc(n,zeta),label="n={}".format(n))
163 #plt.legend()
164 plt.title("Z-eigenfunction")
165 plt.show()
166 
167 xpos = 0.6
168 zpos = 0.8
169 thetapos = 0.6
170 
```

```
dr = 0.1
dz = 0.1
dtheta = 0.2/xpos

print('dr',dr*Rmax,'dtheta', dtheta*180/np.pi,'dz', dz*L)
print('xpos',xpos*Rmax,'theta pos', thetapos*pi*180/np.pi,'zpos', zpos*L)

Q = 1e-3/(dr*Rmax*dz*L*xpos*Rmax*dtheta)
#Q = 1e18
vol = (dr*Rmax*dz*L*xpos*Rmax*dtheta)
print('Volume (um3)', vol*1e18)
print("Source in W/m3", Q)
Qx = [xpos-dr/2, xpos+dr/2]
Qy = [(thetapos*np.pi)-dtheta/2, (thetapos*np.pi)+dtheta/2]
Qz = [zpos-dz/2, zpos+dz/2]

intxx = np.linspace(Qx[0],Qx[1],meshR)
intyx = np.linspace(Qy[0],Qy[1],meshTheta)
intzx = np.linspace(Qz[0],Qz[1],meshZ)

sigma = Q*L**2/(kappa*Tinf)
a = L/Rmax

print('Calculating ALMN')
Almn = np.zeros((numl,numm,numn))
for ll in range(0,numl):
    for mm in range(0,numm):
        for nn in range(0,numn):
            lamvals = (a*mu[ll,mm])**2+(omega[nn])**2
            #integ = 2*np.trapz(intxx*Xfunc(mu[ll],intxx)**2,intxx)*
            np.trapz(Yfunc(mm,intyx),intyx)*
            np.trapz(Zfunc(omega[nn],intzx),intzx)/
            (normXfunc(mu[ll],intxx)*
```

```
204             Ynormfunc(mm)*Znormfunc(nn))
205
206             integ = 2*np.trapz(intxx*Xfunc(mu[ll,mm],mm,intxx),intxx)*
207             np.trapz(Yfunc(mm,intyx),intyx)*
208             np.trapz(Zfunc(omega[nn],intzx),intzx)/
209             (normXfunc(mu[ll,mm],mm,xi)*
210             Ynormfunc(mm,theta)*Znormfunc(nn,zeta))
211             Almn[ll,mm,nn]=(1/lamvals)*sigma*integ
212
213 Ux = np.zeros((numl,numm,numn,meshR))
214 print('Calculating UX')
215 for ll in range(0,numl):
216     for mm in range(0,numm):
217         for nn in range(0,numn):
218             for ii in range(0,meshR):
219                 Ux[ll,mm,nn,:] = Almn[ll,mm,nn]*XFUNC[ll,mm,:]*
220                 YFUNC[mm,int(thetapos*meshTheta)]*
221                 ZFUNC[nn,int(zpos*meshZ)]
222 print('Calculating Uy')
223 Uy = np.zeros((numl,numm,numn,meshTheta))
224 for ll in range(0,numl):
225     for mm in range(0,numm):
226         for nn in range(0,numn):
227             for ii in range(0,meshTheta):
228                 Uy[ll,mm,nn,:] =
229                 Almn[ll,mm,nn]*XFUNC[ll,mm,int(xpos*meshR)]*
230                 YFUNC[mm,:]*
231                 ZFUNC[nn,int(zpos*meshZ)]
232 print('Calculating Uz')
233 Uz = np.zeros((numl,numm,numn,meshZ))
234 for ll in range(0,numl):
235     for mm in range(0,numm):
236         for nn in range(0,numn):
```

```
            for ii in range(0,meshZ):
                Uz[ll,mm,nn,:] = Almn[ll,mm,nn]*XFUNC[ll,mm,int(xpos*meshR
    )]*
                YFUNC[mm,int(thetapos*meshTheta)]*
                ZFUNC[nn,:]

#dataX = pd.read_csv("cyl_x.csv", skiprows=7).values
#dataZ = pd.read_csv("cyl_z.csv", skiprows=7).values
#dataT = pd.read_csv("cyl_theta.csv", skiprows=7).values
#xFEA = dataX[:,0]
#UxFEA = dataX[:,1]
#TFEA = dataT[:,0]
#UTFEA = dataT[:,1]
#zFEA = dataZ[:,0]
#UzFEA = dataZ[:,1]
#plt.plot(xFEA,UxFEA)

plt.rcParams['figure.figsize'] = [12, 4]
Ux2 = np.sum(np.sum(np.sum(Ux, axis=2),axis=1),axis =0)*Tinf
Uy2 = np.sum(np.sum(np.sum(Uy, axis=2),axis=1),axis =0)*Tinf
Uz2 = np.sum(np.sum(np.sum(Uz, axis=2),axis=1),axis =0)*Tinf
plt.plot(xi*Rmax, Ux2, 'k-', linewidth=5, label='Analytical')
#plt.plot(xFEA,UxFEA, 'r--', linewidth=3, label='Finite element')
plt.title('$\Delta T$ vs. x, $Bi_c$={:.2E}, $t$={:.2E}s,
Volume={:.2E}m$^3$'.format(Bic,t,vol))
plt.xlabel('Radius (m)', fontsize=20)
plt.ylabel('$\Delta T$ (K)', fontsize=20)
plt.xticks(fontsize=20)
plt.yticks(fontsize=20)
plt.axvspan(Qx[0]*Rmax, Qx[1]*Rmax, facecolor='r', alpha=0.2,
label='Source = {:.2E} W/$\mu m^3$'.format(Q/1e18))
plt.legend(fontsize=18)
#plt.ylim(0,1.6)
```

```
plt.show()

plt.plot(theta*180/np.pi, Uy2, 'k-', linewidth=5, label='Analytical')
#plt.plot(TFEA,UTFEA,'r--', linewidth=3, label='Finite element')
plt.title('$\Delta T$ vs. $\\theta$, $t$={:.2f}s'.format(t))
plt.xlabel('Angle ($^{\circ}$)', fontsize=20)
plt.ylabel('$\Delta T$ (K)', fontsize=20)
plt.xticks(fontsize=20)
plt.yticks(fontsize=20)
plt.axvspan(Qy[0]*180/np.pi, Qy[1]*180/np.pi, facecolor='r', alpha=0.2,
label='Source = {:.2E} W/$\mu m^3$'.format(Q/1e18))
plt.legend(fontsize=18)
#plt.ylim(0,1.6)
plt.show()

plt.plot(zeta*L, Uz2, 'k-', linewidth=5, label='Analytical')
#plt.plot(zFEA,UzFEA,'r--', linewidth=3, label='Finite element')
plt.title('$\Delta T$ vs. z, $Bi_f$={:.2E}, $t$={:.2f}s'.format(Bif,t))
plt.xlabel('Height (m)', fontsize=20)
plt.ylabel('$\Delta T$ (K)', fontsize=20)
plt.xticks(fontsize=20)
plt.yticks(fontsize=20)
plt.axvspan(Qz[0]*L, Qz[1]*L, facecolor='r', alpha=0.2, label='Source =
{:.2E} W/$\mu m^3$'.format(Q/1e18))
plt.legend(fontsize=18)
#plt.ylim(0,1.6)
plt.show()
```

A.4.1 Time dependent calculations

```
import numpy as np
from scipy.special import jv, yv, lpmn, lpmv, spherical_jn
from math import factorial
import matplotlib.pyplot as plt
```

```
from numpy import pi, sin, cos, sqrt
from mpl_toolkits.mplot3d import axes3d
from matplotlib import cm
%matplotlib inline
plt.rcParams['figure.figsize'] = [15, 5]

ts = np.logspace(-13,-4,15)
Utot = np.zeros((meshR,len(ts)))
for ti in range(0,len(ts)):

    t = ts[ti]                    # Time in seconds
    print('Calculating for t = ',t,' seconds')
    tau = (kappa*t)/(rho*C*L**2)

    print('Calculating ALMN')
    Almn = np.zeros((numl,numm,numn))
    for ll in range(0,numl):
        for mm in range(0,numm):
            for nn in range(0,numn):
                lamvals = (a*mu[ll,mm])**2+(omega[nn])**2
                #integ = 2*np.trapz(intxx*Xfunc(mu[ll],intxx)**2,intxx)*
                np.trapz(Yfunc(mm,intyx),intyx)*
                np.trapz(Zfunc(omega[nn],intzx),intzx)/
                (normXfunc(mu[ll],intxx)*Ynormfunc(mm)*Znormfunc(nn))
                integ =
                2*np.trapz(intxx*Xfunc(mu[ll,mm],mm,intxx),intxx)*np.trap
                z(Yfunc(mm,intyx),intyx)*np.trapz(Zfunc(omega[nn],intzx),
                intzx)/(normXfunc(mu[ll,mm],mm,xi)*Ynormfunc(mm,theta)*Zn
                ormfunc(nn,zeta))
                Almn[ll,mm,nn]=((1-np.exp(-lamvals*tau))/lamvals)*sigma*
                integ


```

```
38      Ux = np.zeros((numl,numm,numn,meshR))
39      print('Calculating UX')
40      for ll in range(0,numl):
41          for mm in range(0,numm):
42              for nn in range(0,numn):
43                  for ii in range(0,meshR):
44                      Ux[ll,mm,nn,:] = Almn[ll,mm,nn]*XFUNC[ll,mm,:]*
45                      YFUNC[mm,int(thetapos*meshTheta)]*
46                      ZFUNC[nn,int(zpos*meshZ)]
47
48
49      Utot[:,ti] = np.sum(np.sum(np.sum(Ux, axis=2),axis=1),axis =0)*Tinf
50      plt.plot(xi*Rmax, Utot[:,ti], label='Time = {} s'.format(t))
51      plt.title('$\Delta T$ vs. x, S({}, 90$^0$ deg, {}) = {} W/m$^3$'.
    format(0.5*Rmax,0.5*L,Q))
52      plt.xlabel('Radius (m)', fontsize=20)
53      plt.ylabel('$\Delta T$ (K)', fontsize=20)
54      plt.xticks(fontsize=20)
55      plt.yticks(fontsize=20)
56      #plt.ylim(0,0.070)
57      plt.legend(fontsize=12)
58  plt.show()
```

Appendix B

DATA ANALYSIS WITH PYTHON

B.1 GUI ipywidgets

Python has a package called "ipywidgets" which can be used to make interactive graphical user interface for the user of your code. In addition to helping the user interface with the code, the GUI also helps with, for instance, a live visualization of your initial parameters that you would use for fitting as you change the values in an input box. This is helpful for fitting curves with better initial guesses, or for simplifying the file selection process for data analysis.

B.2 File Select Button

Running the following will output a button which can be used to select multiple files for processing.

```
import traitlets
import os
import pandas as pd
import matplotlib.pyplot as plt
import numpy as np
from tkinter import Tk, filedialog
from ipywidgets import *
from IPython.display import clear_output, display, Javascript
from IPython.core.display import display, HTML

# Function for creating select files dialogue
def select_files(b):
    root = Tk()
```

```
    root.withdraw()                                          # Hide the main
    window
    root.call('wm', 'attributes', '.', '-topmost', True)    # Raise the
   root to the top of all windows.
    b.files = filedialog.askopenfilename(multiple=True)     # List of
   selected fileswill be set to b.value
    f = b.files
    b.description = "Files Selected"
    b.icon = "check-square-o"
    b.style.button_color = "lightgreen"
    #clear_output()
    # Adding the dot variable helps you access
    # the variable value outside the function.
    select_files.selectfs = SelectMultiple(options=f, value=[f[0]],
    disabled=False, layout=Layout(width='100%', height='300px'))
    print("Selected files:")
    display(select_files.selectfs)

fileselect = Button(description="File Select")
fileselect.icon = "square-o"
fileselect.style.button_color = "orange"
fileselect.on_click(select_files)

display(fileselect)
```

Once the files are selected the path string list can be inserted into a variable f using the following code.

```
f = select_files.selectfs.value
```

A loop can be therefore be added to process the files sequentially by looping through the following. In this case, the ith ASCII file with two columns is read and plotted one after another. Additional analysis to be done on each data file may be added inside the loop.

```
for i in range(0,len(f)):
```

```
    fx = select_files.selectfs.value[i]
    x = pd.read_csv(fx, sep=None, engine='python').values[:,0]
    y = pd.read_csv(fx, sep=None, engine='python').values[:,0]
    plt.plot(x,y)
    plt.show()
```

B.3 Defining NV emission fitting model

```
L1 = LorentzianModel(prefix='L1')
L2 = LorentzianModel(prefix='L2')
G1 = GaussianModel(prefix='G1')
G2 = GaussianModel(prefix='G2')
G3 = GaussianModel(prefix='G3')
G4 = GaussianModel(prefix='G4')
G5 = GaussianModel(prefix='G5')
G6 = GaussianModel(prefix='G6')
G7 = GaussianModel(prefix='G7')
G8 = GaussianModel(prefix='G8')
G9 = GaussianModel(prefix='G9')

model = L1+G1+G2+G3+G4+G5+L2+G6+G7+G8+G9
params = Parameters()
Pnames = model.param_names

def plotter(*args, **kwargs):

    params.add(Pnames[0], value=L1amp.value, vary=True)
    params.add(Pnames[1], value=L1cen.value, vary=False)
    params.add(Pnames[2], value=L1sig.value, vary=False)

    params.add(Pnames[3], value=G1amp.value, vary=True)
    params.add(Pnames[4], value=G1cen.value, vary=False)
    params.add(Pnames[5], value=G1sig.value, vary=False)
```

```
26
27      params.add(Pnames[6], value=G2amp.value, vary=True)
28      params.add(Pnames[7], value=G2cen.value, vary=False)
29      params.add(Pnames[8], value=G2sig.value, vary=False)
30
31      params.add(Pnames[9], value=G3amp.value, vary=True)
32      params.add(Pnames[10], value=G3cen.value, vary=False)
33      params.add(Pnames[11], value=G3sig.value, vary=False)
34
35      params.add(Pnames[12], value=G4amp.value, vary=True)
36      params.add(Pnames[13], value=G4cen.value, vary=False)
37      params.add(Pnames[14], value=G4sig.value, vary=False)
38
39      params.add(Pnames[15], value=G5amp.value, vary=True)
40      params.add(Pnames[16], value=G5cen.value, vary=False)
41      params.add(Pnames[17], value=G5sig.value, vary=False)
42
43      params.add(Pnames[18], value=L2amp.value, vary=True)
44      params.add(Pnames[19], value=L2cen.value, vary=False)
45      params.add(Pnames[20], value=L2sig.value, vary=False)
46
47      params.add(Pnames[21], value=G6amp.value, vary=True)
48      params.add(Pnames[22], value=G6cen.value, vary=False)
49      params.add(Pnames[23], value=G6sig.value, vary=False)
50
51      params.add(Pnames[24], value=G7amp.value, vary=True)
52      params.add(Pnames[25], value=G7cen.value, vary=False)
53      params.add(Pnames[26], value=G7sig.value, vary=False)
54
55      params.add(Pnames[27], value=G8amp.value, vary=True)
56      params.add(Pnames[28], value=G8cen.value, vary=False)
57      params.add(Pnames[29], value=G8sig.value, vary=False)
58
```

```
59      params.add(Pnames[30], value=G9amp.value, vary=True)
60      params.add(Pnames[31], value=G9cen.value, vary=False)
61      params.add(Pnames[32], value=G9sig.value, vary=False)
62
63      init = model.eval(params, x=xev)
64      plt.scatter(xev, y, s=3)
65      out = model.fit(y, params, x=xev)
66
67      components = out.eval_components(x=xev)
68      for model_name, model_value in components.items():
69          plt.fill(xev, model_value, alpha=0.1)
70
71      plt.title('2050$\mu$W - 532 nm', fontsize=16)
72      plt.xlabel('Energy (eV)', fontsize=18)
73      plt.ylabel('Intensity (arb. units)', fontsize=18)
74      plt.xticks(fontsize=18)
75      plt.yticks(fontsize=18)
76
77      plt.plot(xev, init, 'k--', label="Initial guess", alpha=1)
78      plt.plot(xev, out.best_fit, 'r-')
79      plt.show()
80
81      print(out.fit_report(min_correl=0.5))
82
83  f=selectFiles.files
84  st = 0
85  en = -1
86
87  x = pd.read_csv(f[0], sep=None, engine='python').values[st:en,0]
88  y = pd.read_csv(f[0], sep=None, engine='python').values[st:en,1]
89  xev = 1240/x
90
91  L1cen = BoundedFloatText(value=1.94515987152471, min=np.min(xev),
```

```
92 max=np.max(xev), step=abs(xev[1]-xev[0]), description='L1cen')
93 L1sig = BoundedFloatText(value=0.006, min=0.002, max=0.02, step=0.0005,
94 description='L1sig')
95 L1amp = BoundedFloatText(value=129, min=0, max=np.max(y), step=1,
96 description='L1amp')
97
98 G1sig = BoundedFloatText(value=0.028, min=0.02, max=0.1, step=0.001,
99 description='G1sig')
100 G1amp = BoundedFloatText(value=2261, min=0, max=np.max(y), step=1,
101 description='G1amp')
102 G1cen = BoundedFloatText(value=1.87719923672072, min=np.min(xev),
103 max=np.max(xev), step=abs(xev[1]-xev[0]), description='G1cen')
104
105 G2sig = BoundedFloatText(value=0.028, min=0.02, max=0.1, step=0.001,
106 description='G2sig')
107 G2amp = BoundedFloatText(value=2509, min=0, max=np.max(y), step=1,
108 description='G2amp')
109 G2cen = BoundedFloatText(value=1.81723397071721, min=np.min(xev),
110 max=np.max(xev), step=abs(xev[1]-xev[0]), description='G2cen')
111
112 G3sig = BoundedFloatText(value=0.028, min=0.02, max=0.1, step=0.001,
113 description='G3sig')
114 G3amp = BoundedFloatText(value=1764, min=0, max=np.max(y), step=1,
115 description='G3amp')
116 G3cen = BoundedFloatText(value=1.76037801480277, min=np.min(xev),
117 max=np.max(xev), step=abs(xev[1]-xev[0]), description='G3cen')
118
119 G4sig = BoundedFloatText(value=0.042, min=0.02, max=0.3, step=0.001,
120 description='G4sig')
121 G4amp = BoundedFloatText(value=2015, min=0, max=np.max(y), step=1,
    description='G4amp')
122 G4cen = BoundedFloatText(value=1.70574299466623, min=np.min(xev),
123 max=np.max(xev), step=abs(xev[1]-xev[0]), description='G4cen')
```

```
124
125 G5sig = BoundedFloatText(value=0.061, min=0.02, max=0.4, step=0.001,
126 description='G5sig')
127 G5amp = BoundedFloatText(value=1352, min=0, max=np.max(y), step=1,
128 description='G5amp')
129 G5cen = BoundedFloatText(value=1.62889861675062, min=np.min(xev),
130 max=np.max(xev), step=abs(xev[1]-xev[0]), description='G5cen')
131
132 L2cen = BoundedFloatText(value=2.15437202180363, min=np.min(xev),
133 max=np.max(xev), step=abs(xev[1]-xev[0]), description='L2cen')
134 L2sig = BoundedFloatText(value=0.0105, min=0.002, max=0.02, step=0.0005,
135 description='L2sig')
136 L2amp = BoundedFloatText(value=163.6, min=0, max=np.max(y), step=1,
137 description='L2amp')
138
139 G6sig = BoundedFloatText(value=0.024, min=0.02, max=0.4, step=0.001,
140 description='G6sig')
141 G6amp = BoundedFloatText(value=242, min=0, max=np.max(y), step=1,
142 description='G6amp')
143 G6cen = BoundedFloatText(value=2.11128586771222, min=np.min(xev),
144 max=np.max(xev), step=abs(xev[1]-xev[0]), description='G6cen')
145
146 G7sig = BoundedFloatText(value=0.026, min=0.02, max=0.4, step=0.001,
147 description='G7sig')
148 G7amp = BoundedFloatText(value=355, min=0, max=np.max(y), step=1,
149 description='G7amp')
150 G7cen = BoundedFloatText(value=2.05665084757569, min=np.min(xev),
151 max=np.max(xev), step=abs(xev[1]-xev[0]), description='G7cen')
152
153 G8sig = BoundedFloatText(value=0.028, min=0.02, max=0.4, step=0.001,
154 description='G8sig')
155 G8amp = BoundedFloatText(value=607, min=0, max=np.max(y), step=1,
156 description='G8amp')
```

```
G8cen = BoundedFloatText(value=1.99535302010543, min=np.min(xev), max=np.max(xev), step=abs(xev[1]-xev[0]), description='G8cen')

G9sig = BoundedFloatText(value=0.028, min=0.02, max=0.4, step=0.001, description='G9sig')
G9amp = BoundedFloatText(value=1057, min=0, max=np.max(y), step=1, description='G9amp')
G9cen = BoundedFloatText(value=1.93494356694633, min=np.min(xev), max=np.max(xev), step=abs(xev[1]-xev[0]), description='G9cen')

H1 = HBox([L1amp, L1sig, L1cen])
H2 = HBox([G1amp, G1sig, G1cen])
H3 = HBox([G2amp, G2sig, G2cen])
H4 = HBox([G3amp, G3sig, G3cen])
H5 = HBox([G4amp, G4sig, G4cen])
H6 = HBox([G5amp, G5sig, G5cen])
H7 = HBox([L2amp, L2sig, L2cen])
H8 = HBox([G6amp, G6sig, G6cen])
H9 = HBox([G7amp, G7sig, G7cen])
H10 = HBox([G8amp, G8sig, G8cen])
H11 = HBox([G9amp, G9sig, G9cen])


V1 = VBox([H1,H2,H3,H4,H5,H6,H7,H8,H9,H10,H11])
w=interactive_output(plotter, {'L1amp':L1amp, 'L1sig':L1sig, 'L1cen':L1cen, 'G1amp':G1amp, 'G1sig':G1sig, 'G1cen':G1cen, 'G2amp':G2amp, 'G2sig':G2sig, 'G2cen':G2cen, 'G3amp':G3amp, 'G3sig':G3sig, 'G3cen':G3cen, 'G4amp':G4amp, 'G4sig':G4sig, 'G4cen':G4cen, 'G5amp':G5amp, 'G5sig':G5sig, 'G5cen':G5cen, 'L2amp':L2amp, 'L2sig':L2sig, 'L1cen':L2cen, 'G6amp':G6amp, 'G6sig':G6sig, 'G6cen':G6cen, 'G7amp':G7amp, 'G7sig':G7sig, 'G7cen':G7cen, 'G8amp':G8amp, 'G8sig':G8sig, 'G8cen':G8cen, 'G9amp':G9amp, 'G9sig':G9sig, 'G9cen':G9cen})
```

```
189
190 display(V1,w)
191 OkButton = Button(description="OK")
192 OkButton.on_click(run_all)
193 display(OkButton)
194
195 ##########################################################################
196 # This function retrieves the powers from the file name by searching for
197 # st_532 and st_1020 in the filenames
198 # f is the list of files, this need not be entered as long as the
199 # variable f contains all the filenames.
200 # st_532 takes in the string that is to be searched in each file name.
201 # len_532 is the length of parameter value after the st_532.
202 def parout(st_532,len_532,f=f):
203     pow532 = []
204     for iy in range(0,len(f)):
205         start_532 = f[iy].find(st_532)+len(st_532)
206         pow532.append(f[iy][start_532:start_532+len_532])
207     return pow532
208
209 ##########################################################################
210 # This function retrieves the powers from the file name by searching for
211 # st_532 and st_1020 in the filenames
212 # f is the list of files, this need not be entered as long as the
213 # variable f contains all the filenames.
214 # st_532 takes in the string that is to be searched in each file name.
215 # len_532 is the length of parameter value after the st_532.
216 def parout(st_532,len_532,f=f):
217     pow532 = []
218     for iy in range(0,len(f)):
219         start_532 = f[iy].find(st_532)+len(st_532)
220         pow532.append(f[iy][start_532:start_532+len_532])
221     return pow532
```

B.4 Fitting NV spectra sequentially

```
%matplotlib inline
DWFs = np.zeros(len(f))
NV0areas = np.zeros(len(f))
NVmareas = np.zeros(len(f))
j=0
#gains = parout('ms_',3)
#times = parout('nm_',3)

# Enter the string before the laser power entry in the file name
#st_1020 = '532ex_'
# Enter the length of the laser power string
#len_1020 = 5
#pow1020 = parout(st_1020,len_1020)
#pow1020 = np.array([float(ix) for ix in pow1020])

#print(gains, times, pow1020)

for j in range(0,len(f)):
    #norm = float(pow1020[j])*float(gains[j])*float(times[j])
    x = pd.read_csv(f[j], sep=None, engine='python').values[st:en,0]
    #y = pd.read_csv(f[j], sep=None, engine='python').values[st:en,1]/norm
    y = pd.read_csv(f[j], sep=None, engine='python').values[st:en,1]
    xev = 1240/x

    print("File:",f[j])
    head, tail = os.path.split(f[j])

    out = model.fit(y, params, x=xev)
    plt.rcParams['figure.figsize'] = [5, 5]
    plt.scatter(xev, y, s=3)
    #plt.plot(xev, init, 'k--', label="Initial guess", alpha=0.5)
```

```
    plt.plot(xev, out.best_fit, 'r-')

    components = out.eval_components(x=xev)
    for model_name, model_value in components.items():
        plt.fill(xev, model_value, alpha=0.1)

    plt.title(tail, fontsize=12)
    plt.xlabel('Energy (eV)', fontsize=18)
    plt.ylabel('Intensity (arb. units)', fontsize=18)
    plt.xticks(fontsize=18)
    plt.yticks(fontsize=18)
    plt.show()


    areanames = [Pnames[i] for i in range(0, len(Pnames), 3)]
    Pareas = np.zeros(len(areanames))
    for i in range(0,len(areanames)):
        Pareas[i] = out.best_values[areanames[i]]
        print(areanames[i],out.best_values[areanames[i]])

    NVmareas[j] = Pareas[0]+Pareas[1]+Pareas[2]+Pareas[3]+Pareas[4]+
    Pareas[5]
    NV0areas[j] = Pareas[6]+Pareas[7]+Pareas[8]+Pareas[9]+Pareas[10]
    ZPL = Pareas[0]
    overtones = np.sum(Pareas)-ZPL
    DWFln = np.log(ZPL/overtones)
    DWFs[j] = DWFln
    print("ln(DWF): ", DWFln)
```

B.5 Radiation Pressure Calculations

The radiation pressure depends on the energy fluxes of the absorbed, reflected, and radiantly emitted energy. For the relatively low temperatures involved here and because the emissivity of CdSNR is very low for a wavelength of 532 nm the radiantly emitted energy is negligible

compared with the absorbed and reflected contributions.

For a wave that is completely absorbed the radiation pressure is given by

$$P_{abs} = \frac{fT_\lambda \langle S \rangle}{c}, \tag{B.1}$$

in which f is the fraction absorbed, T_λ is the wavelength-dependent transmission coefficient, and c is the velocity of light. For a thin fiber of thickness H, the fraction of light absorbed is

$$f = 1 - \exp\left(-2k''H\right). \tag{B.2}$$

For a CdS fiber with a thickness of 110 nm and for a wavelength of 532 nm, $f = 0.0148$. The radiation pressure resulting from reflection is given by

$$P_{ref} = \frac{2R_\lambda \langle S \rangle}{c}, \tag{B.3}$$

where R_λ is the reflection coefficient which depends on the polarization of the laser beam and its wavelength, and $T_\lambda = 1 - R_\lambda$. For CdS, using a wavelength of 532 nm, $R_\lambda = 0.20315$. Consequently, the total radiation pressure becomes

$$P_{rad} = (fT_\lambda + 2R_\lambda)\frac{\langle S \rangle}{c} = [f(1 - R_\lambda) + 2R_\lambda]\frac{\langle S \rangle}{c}. \tag{B.4}$$

The approximation $\langle S \rangle$ is given by

$$\langle S \rangle = I_0 \exp\left(\frac{-2r^2}{w_0^2}\right). \tag{B.5}$$

Consequently, the force on the fiber becomes

$$\begin{aligned} F &= \frac{[f(1 - R_\lambda) + 2R_\lambda]I_0}{c} \int_0^{2\pi} \int_0^{W/2} \exp\left(\frac{-2r^2}{w_0^2}\right) r dr d\theta \\ &= \frac{[f(1 - R_\lambda) + 2R_\lambda]\pi w_0^2 I_0}{2c} \left[1 - \exp\left(\frac{-W^2}{2w_0^2}\right)\right]. \end{aligned} \tag{B.6}$$

Thus, for the given geometry and optical parameters mentioned in the manuscript, a force of $3.21\text{x}10^{-14}$ and $1.65\text{x}10^{-12}$ N is obtained for a laser power of 35 and 1800 μW respectively.

The deflection (δ_{max}) for a uniform rectangular cantilever of length L and moment of inertia $I = (WH^3)/12$, with a load F acting at the end of the cantilever is given by,

$$\delta_{max} = \frac{FL^3}{3EI}. \tag{B.7}$$

A maximum deflection at the end of the cantilever of dimensions $L = 35$ μm, $W = 2.3$ μm and $H = 0.11$ μm and $E = 45$ GPa of $\delta_{max} = 3.9\text{x}10^{-11}$ m and $2\text{x}10^{-9}$ m were calculated for loads of $3.21\text{x}10^{-14}$ and $1.65\text{x}10^{-12}$ N, respectively.

Appendix C

PYTHON MEEP

Python meep is run in Jupyter notebook using the meep environment in Linux. Please refer to the Python MEEP documentation to get started.

C.1 Focused Gaussian beam and 2D geometries

```
# http://maxwellrules.com/index.php/2018/02/28/gaussian-beams/
# Propagates in both directions, and has the beam waist displaced from the
    source position

import meep as mp
import math
import cmath
import numpy as np
import matplotlib.pyplot as plt
import numpy as np

resolution = 15 # pixels per um
cell_x = 30
cell_y = 20
timest = 200
cell_size = mp.Vector3(cell_x,cell_y,0)

pml_layers = [mp.PML(thickness=1.0)]

lambda0 = 0.670
fcen = 1/lambda0 # center frequency of CW source (wavelength is 1 um)

```

```
tilt_angle = math.radians(0) # angle of tilted beam
k = mp.Vector3(y=2*np.pi*fcen).rotate(mp.Vector3(z=1),tilt_angle)

w0 = 1.15
dist_to_waist = 9  #z
n1 = 1.456
n2 = 1e-6
n = n1+1j*n2
eps0 = 8.854e-12
eps = n**2
epsinf = np.real(eps)
dcond = fcen*2*np.pi*np.imag(eps)/epsinf
zr = math.pi*1*fcen*w0**2
Z0 = 376.73

L = 10
W = 5
angle = math.radians(0)
rad = 9.42/2

#YLF
vertices = [mp.Vector3(-L/2,0).rotate(mp.Vector3(z=1),angle),
            mp.Vector3(0,W/2).rotate(mp.Vector3(z=1),angle),
            mp.Vector3(L/2,0).rotate(mp.Vector3(z=1),angle),
            mp.Vector3(0,-W/2).rotate(mp.Vector3(z=1),angle),]

#rectangle
#vertices = [mp.Vector3(-L/2,W/2).rotate(mp.Vector3(z=1),angle), mp.
   Vector3(L/2,W/2).rotate(mp.Vector3(z=1),angle), mp.Vector3(L/2,-W/2).
   rotate(mp.Vector3(z=1),angle), mp.Vector3(-L/2,-W/2).rotate(mp.Vector3(
   z=1),angle),]

def gaussian_beam(zr, k, z):
```

```
52      def _gaussian_beam(x):
53          zprime = z/zr
54          return (1/np.sqrt(1+zprime**2))*np.exp(-k.norm()*x.norm()**2/(2*zr
    *(1+zprime**2)))*np.exp(-1j*zprime*k.norm()*x.norm()**2/(2*zr*(1+zprime
    **2)))*np.exp(1j*np.arctan2(z,zr))*np.exp(-1j*k.dot(x))
55      return _gaussian_beam
56
57 src_pt = mp.Vector3(y=9)
58 sources = [mp.Source(src=mp.ContinuousSource(fcen, fwidth=0.2*fcen),
59                      component=mp.Ez,
60                      center=src_pt,
61                      size=mp.Vector3(20),
62                      amp_func=gaussian_beam(zr,k,dist_to_waist))]
63
64 geometry = [mp.Prism(vertices, height=0, center=mp.Vector3(L/4,0),
    material=mp.Medium(epsilon=epsinf, D_conductivity=dcond))]
65
66 non_pml_vol = mp.Volume(center=mp.Vector3(), size=mp.Vector3(cell_x-2,
    cell_y-2,0))
67
68 sim = mp.Simulation(cell_size=cell_size,
69                     sources=sources,
70                     geometry=geometry,
71                     k_point=k,
72                     boundary_layers=pml_layers,
73                     resolution=resolution)
74
75 #sim.run(mp.in_volume(particle_vol, mp.to_appended("ez_particle",
76 mp.at_every(0.6, mp.output_efield_z))),until=200)
77 sim.run(mp.to_appended("ez", mp.at_every(0.6, mp.output_efield_z)),
78 until=timest)
79
80 eps_data = sim.get_array(vol=non_pml_vol, center=mp.Vector3(),
```

```
size=cell_size, component=mp.Dielectric)
ez_data = sim.get_array(vol=non_pml_vol, component=mp.Ez)
(Ex,Ey,Ez)     = [sim.get_array(vol=non_pml_vol, component=c, cmplx=True)
for c in [mp.Ex, mp.Ey, mp.Ez]]
(x,y,z,w) = sim.get_array_metadata(vol=non_pml_vol)
energy_density = np.real(eps_data*(np.conj(Ex)*Ex + np.conj(Ey)*Ey +
np.conj(Ez)*Ez))
energy = np.sum(w*energy_density)
```

C.2 Reading MEEP output and plotting

```
import h5py
import numpy as np
import matplotlib.pyplot as plt
import numpy as np
from mpl_toolkits.axes_grid1 import make_axes_locatable
from matplotlib.colors import LogNorm
from matplotlib.ticker import MultipleLocator

filename = 'ez.h5'
f = h5py.File(filename, 'r')

# List all groups
print("Keys: %s" % f.keys())
imag_group_key = list(f.keys())[0]
real_group_key = list(f.keys())[1]

datashape = np.shape(f[real_group_key])
print(datashape)

ez_real = f[real_group_key]
ez_imag = f[imag_group_key]

time = 300
```

```
ezreal_time150 = ez_real[:,:,time]
ezimag_time150 = ez_imag[:,:,time]
fig, (ax1, ax2, ax3) = plt.subplots(1,3, figsize=[15,4.4])

fig.suptitle('Electric fields in a YLF (s=5 $\mu$m), $\lambda$=1000 nm',
fontsize=20)

ax1.set_title('ez_real')
# Display image, `aspect='auto'` makes it fill the whole `axes` (ax3)

im1 = ax1.imshow(np.flipud(eps_data.transpose()), aspect='auto',
cmap='binary', extent=[-(cell_x-2)/2,(cell_x-2)/2,
-(cell_y-2)/2,(cell_y-2)/2])
im1 = ax1.imshow(np.flipud(np.transpose(ezreal_time150)), aspect='auto',
cmap='seismic', extent=[-(cell_x-2)/2,(cell_x-2)/2,
-(cell_y-2)/2,(cell_y-2)/2], alpha=0.8)
ax1.set_xlabel("x coordinate ($\mu$m)")
ax1.set_ylabel("y coordinate ($\mu$m)")

# Create divider for existing axes instance
divider1 = make_axes_locatable(ax1)
# Append axes to the right of ax3, with 20% width of ax3
cax1 = divider1.append_axes("right", size="10%", pad=0.05)
# Create colorbar in the appended axes
# Tick locations can be set with the kwarg `ticks`
# and the format of the ticklabels with kwarg `format`
cbar1 = plt.colorbar(im1, cax=cax1, format="%.2f")

ax2.set_title('ez_imag')
ax2.set_xlabel("x coordinate ($\mu$m)")
ax2.set_ylabel("y coordinate ($\mu$m)")
im2 = ax2.imshow(np.flipud(eps_data.transpose()), aspect='auto',
cmap='binary', extent=[-(cell_x-2)/2,(cell_x-2)/2,
```

```
-(cell_y-2)/2,(cell_y-2)/2])
im2 = ax2.imshow(np.flipud(np.transpose(ezimag_time150)), aspect='auto',
cmap='seismic', extent=[-(cell_x-2)/2,(cell_x-2)/2,
-(cell_y-2)/2,(cell_y-2)/2], alpha=0.8)

divider2 = make_axes_locatable(ax2)
cax2 = divider2.append_axes("right", size="10%", pad=0.05)
cbar2 = plt.colorbar(im2, cax=cax2, format="%.2f")

ax3.set_title('Energy')
ax3.set_xlabel("x coordinate ($\mu$m)")
ax3.set_ylabel("y coordinate ($\mu$m)")
im3 = ax3.imshow(np.flipud(eps_data.transpose()), aspect='auto',
cmap='binary', extent=[-(cell_x-2)/2,(cell_x-2)/2,
-(cell_y-2)/2,(cell_y-2)/2])
im3 = ax3.imshow(np.flipud(np.transpose(energy_density)), aspect='auto',
cmap='jet', extent=[-(cell_x-2)/2,(cell_x-2)/2,
-(cell_y-2)/2,(cell_y-2)/2], alpha=0.8 , vmin=0, vmax=0.36)
#im3 = ax3.imshow(np.flipud(np.transpose(np.real((ezreal_time150+1j*
ezimag_time150)*(ezreal_time150-1j*ezimag_time150)))),
aspect='auto', cmap='jet', extent=[-10,10, -9,9], alpha=0.8)
divider3 = make_axes_locatable(ax3)
cax3 = divider3.append_axes("right", size="10%", pad=0.05)
cbar3 = plt.colorbar(im3, cax=cax3)


plt.tight_layout()
# Make space for title
plt.subplots_adjust(top=0.85)
plt.show()

f.close()
```

C.3 3D Focused Gaussian propagation with hexagonal prism

```
import meep as mp
import math
import cmath
import numpy as np
import matplotlib.pyplot as plt

thickness = [890, 920, 950]
for i in range (0,len(thickness)):
    resolution = 30 # pixels per um
    cell_x = 5
    cell_y = 5
    cell_z = 5
    timest = 75

    cell_size = mp.Vector3(cell_x,cell_y,cell_z)

    pml_layers = [mp.PML(thickness=1.0,direction=mp.Z)]

    lambda0 = 1.020
    rect_h = 2
    rect_w = 2
    rect_l = 2
    fcen = 1/lambda0 # center frequency of CW source (wavelength is 1 um)
    k = mp.Vector3(z=2*np.pi*fcen)

    w0 = 1.15
    dist_to_waist = (cell_z/2)-1  #z

    n1 = 1.4705
    n2 = 3.34e-6
    n = n1+1j*n2
```

```
    eps0 = 8.854e-12
    eps = n**2
    epsinf = np.real(eps)
    dcond = fcen*2*np.pi*np.imag(eps)/epsinf
    zr = math.pi*1*fcen*w0**2
    Z0 = 376.73

    def gaussian_beam(zr, k, z):
        def _gaussian_beam(x):
            zprime = z/zr
            return (1/np.sqrt(1+zprime**2))*np.exp(-k.norm()*x.norm()**2
            /(2*zr*(1+zprime**2)))*np.exp(-1j*zprime*k.norm()*x.norm()**
            2/(2*zr*(1+zprime**2)))*np.exp(1j*np.arctan2(z,zr))*
            np.exp(-1j*k.dot(x))
        return _gaussian_beam

    src_pt = mp.Vector3(z=(cell_z/2)-1)
    sources = [mp.Source(src=mp.ContinuousSource(fcen, fwidth=0.2*fcen),
                         component=mp.Ey,
                         center=src_pt,
                         size=mp.Vector3(cell_x, cell_y, 0),
                         amp_func=gaussian_beam(zr,k,dist_to_waist))]

    hexht = thickness[i]/1000
    r = 0.5
    vertices = [mp.Vector3(-r,0),
                mp.Vector3(-r/2,r*math.sqrt(3)/2),
                mp.Vector3(r/2,r*math.sqrt(3)/2),
                mp.Vector3(r,0),
                mp.Vector3(r/2,-r*math.sqrt(3)/2),
                mp.Vector3(-r/2,-r*math.sqrt(3)/2),]

    geometry = [mp.Prism(vertices, height=hexht, center=mp.Vector3(),
```

```
    material=mp.Medium(epsilon=epsinf, D_conductivity=dcond))]
65
66      particle_vol = mp.Volume(center=mp.Vector3(), size=mp.Vector3(rect_w,
        rect_h,rect_l))
67      non_pml_vol = mp.Volume(center=mp.Vector3(), size=mp.Vector3(cell_x,
        cell_y,cell_z-2))
68
69      sim = mp.Simulation(cell_size=cell_size,
70                          sources=sources,
71                          k_point=k,
72                          boundary_layers=pml_layers,
73                          geometry=geometry,
74                          resolution=resolution)
75
76      fnameprefix = "H-{0:0=4d}nm".format(int(hexht*1000))
77      sim.run(mp.at_beginning(mp.with_prefix(fnameprefix,mp.output_epsilon)
78      ),mp.at_end(mp.with_prefix(fnameprefix,mp.output_efield_y)),
79      until=timest)
```

C.4 Plotting electric fields

```
1  import matplotlib.pyplot as plt
2  from mpl_toolkits.axes_grid1 import make_axes_locatable
3  from matplotlib.colors import LogNorm
4  from matplotlib.ticker import MultipleLocator
5  import h5py
6  import numpy as np
7  import matplotlib.pyplot as plt
8
9  #cell_x = 5
10 #cell_y = 5
11 #cell_z = 5
12 #timest = 75
13 plt.rcParams['figure.figsize'] = [10, 10]
```

```
#i = 1
#thickness = [530, 590, 650, 710, 770, 830, 890, 950]
totegys = np.zeros(len(thickness))

for i in range (0,len(thickness)):

    fname = "H-{0:0=4d}nm-ey-{1:0=6d}.00.h5".format(thickness[i],timest)
    feps = "H-{0:0=4d}nm-eps-000000.00.h5".format(thickness[i])
    print("Reading: ", fname)
    #fname = 'ey_W_2000nm_H_{0:0=4d}nm.h5'.format(thickness[i])
    #feps = 'eps_W_2000nm_H_{0:0=4d}nm.h5'.format(thickness[i])
    fey = h5py.File(fname, 'r')
    fepsn = h5py.File(feps, 'r')

    # List all groups
    #print("Keys: %s" % fepsn.keys())
    epsgk = list(fepsn.keys())[0]
    imag_group_key = list(fey.keys())[0]
    real_group_key = list(fey.keys())[1]

    datashape = np.shape(fepsn[epsgk])
    xshp, yshp, zshp = (datashape)
    eps_data = np.array(fepsn[epsgk])
    #print('Datashape:',datashape)

    ez_real = np.array(fey[real_group_key])
    ez_imag = np.array(fey[imag_group_key])
    egy = np.real((ez_real+1j*ez_imag)*(ez_real-1j*ez_imag))

    egyhex = np.where(eps_data!=1, egy, 0)

    xcoord = np.linspace(-cell_x/2,cell_x/2,len(egyhex[:,int(yshp/2),
    int(zshp/2)]))
```

```
47      ycoord = np.linspace(-cell_y/2,cell_y/2,len(egyhex[int(xshp/2),:,
48      int(zshp/2)]))
49      zcoord = np.linspace(-cell_z/2,cell_z/2,len(egyhex[int(xshp/2),
50      int(yshp/2),:]))
51      totalegy = np.trapz(np.trapz(np.trapz(egyhex,zcoord),ycoord),xcoord)
52      totegys[i] = totalegy
53
54
55      plt.title('E.E*/E$_0$ along the center line in z direction')
56      # Display image, `aspect='auto'` makes it fill the whole `axes` (ax3)
57
58      #im1 = ax1.imshow(np.flipud(np.transpose(np.real(eps_data[:,100,:])))
59      , interpolation='spline36', aspect='auto', cmap='binary',
60      extent=[-10,10, -9,9])
61
62      plt.plot(zcoord,np.flipud(np.transpose(egyhex[int(xshp/2),
63      int(yshp/2),:])), label=thickness[i])
64      plt.legend(title='Thickness (nm)')
65      plt.xlabel("z coordinate ($\mu$m)")
66      plt.ylabel("E.E*/E$_0$")
67      # Create divider for existing axes instance
68
69  plt.show()
```